DEVELOPMENT OF A HYBRID PNEUMATIC-ELECTRIC ACTUATOR

DEVELOPMENT OF A HYBRID PNEUMATIC-ELECTRIC ACTUATOR

By Xing Chen, B.A.

A Thesis

Submitted to School of Graduate Studies

In Partial Fulfillment of Requirements

For the Degree

Master of Applied Science

McMaster University

MASTER OF APPLIED SCIENCE (2011)

McMaster University

(Mechanical Engineering)

Hamilton, Ontario

TITLE: Development of a Hybrid Pneumatic-Electric Actuator

AUTHOR: Xing Chen, B.A. (Huaqiao University, Fujian, China)

SUPERVISOR: Dr. Gary M. Bone, Professor

NUMBER OF PAGES: I – XXII

1 - 131

ABSTRACT

Pneumatic actuators are low cost, clean and safe. They also have a high power to weight ratio. However, due to the compressibility of the air and the nonlinearities of their dynamics, they are very difficult to precisely model and control. Electrically powered actuators are easier to model and control, and are the most commonly used actuator in applications requiring fast and precise position control, such as robot arms. However, they require a high ratio transmission to produce sufficient torque or force, the cost of their components is greater, and they have a lower power to weight ratio compared to pneumatic actuators. This thesis presents the development of a novel hybrid pneumatic-electric actuator which combines the advantages of both actuator types.

The design and prototyping of the hybrid actuator is presented first. A pneumatic cylinder and a DC motor are connected in parallel using gears. The components are sized to provide the torque required to rotate a single-link robot arm vertically upwards. On/off solenoid valves are used rather than servo valves to keep the hardware cost low.

Next, a mathematical model of the nonlinear actuator dynamics is derived using a combination of physical laws and empirical curve fitting. The dynamics of the mechanical, electrical and pneumatic elements are included. Then a novel discrete-valued model-predictive control plus integral compensator algorithm is created for controlling the position of the pneumatic cylinder using the on/off valves. The control algorithm for

the hybrid actuator is completed by using a conventional PD algorithm to control the electric motor.

The performances of the hybrid actuator and the pneumatic cylinder acting alone are investigated and compared using computer simulations and hardware experiments. Multiple experiments are done for vertical cycloidal, vertical sine wave and horizontal sine wave trajectories, and different payloads. The steady state performances of the hybrid actuator and pneumatic cylinder are found to be similar. Conversely, the DC motor added a faster acting and finer quantized force to the pneumatic cylinder force, which greatly improved the dynamic position control performance of the hybrid actuator. In experiments, the mean root-mean-square error and the maximum absolute error improved by 84% and 77%, respectively.

TABLE OF CONTENTS

ACKNOWLEDGEMENTS

It takes a long time to finish graduate study as a part time student. Without the support of my supervisor, Dr. Gary M. Bone and my family, this thesis would never have been finished. I like to express my sincerely appreciation to Dr. Bone for his guidance and support. I also like to thank technicians Mr. M. MacKenzie and Mr. J. P. Talon for their support of test equipment. Finally I like to thank everyone who help and support me during my graduate study.

LIST OF FIGURES

LIST OF TABLES

ABBREVIATIONS

DC	Direct current
DMPC	Discrete-valued model-predictive control
DMPC+I	Discrete-valued model-prediction control plus integral compensator
ID	Inverse dynamic
PD	Proportional plus derivative
PI	Proportional plus integral
PRBS	Pseudo random binary signal
PTP	Point to point
PWM	Pulse-width-modulation
MAE	Maximum absolute error
MPC	Model based prediction control
RMSE	Root mean square error
SSA	Steady state amplitude
SSE	Steady state error

NOMENCLATURE

A_a	Piston area in chamber *A*
A_b	Piston area in chamber *B*
C_{vf}	Coefficient of viscous friction
c_{fill}	Filling coefficient for the valve
c_{dis}	Discharging coefficient for the valve
d_{pitch}	Pitch diameter of driven gear
d_{pinion}	Pitch diameter of pinion
d_{bore}	Cylinder bore size
$\hat{e}(k)$	Predicted tracking error
e	Error
F_c	Cylinder force
F_{max}	Maximum force required
F_{motor}	Motor force
$F_{friction}$	Total friction force
F_{cf}	Coulomb friction force
F_{sf}	Static friction force

$F_{cylinder}$	Force generated by the cylinder
F_{arm}	Equivalent gravity force for the arm
$F_{payload}$	Equivalent gravity force for the payload
F_{block}	Gravity force acting on the linear slide block
$F_{gravity}$	Total gravity force
I_{arm}	Moment of inertia of arm
$I_{payload}$	Moment of inertia of payload
i_m	Motor current
K_{ip}	Integral gain
K_{pe}	Proportional gain for the motor
K_{de}	Derivative gain for the motor
K_{amp}	Motor amplifier gain
K_t	Torque constant of the motor
k	Ratio of specific heats of air
L_{arm}	Effective length of the arm
$m_{payload}$	Payload mass
m_{block}	Linear slide block mass
m_{eq}	System equivalent mass
$\dot{m}$	Mass flow rate into the chamber
$\dot{m}_{choked}$	Choked mass flow rate

N_p	Prediction horizon
$n_{d,fill}$	Valve energizing delay in sampling periods
$n_{d,dis}$	Valve de-energizing delay in sampling periods
P_c	Gauge supply pressure
P_a	Absolute pressure inside chamber *A*
P_b	Absolute pressure inside chamber *B*
P_{up}	Upstream pressure
P_{down}	Downstream pressure
P_0	Atmospheric pressure
$\hat{P}_a$	Predicted pressures for chambers A
$\hat{P}_b$	Predicted pressures for chambers B
R	Universal gas constant
T_e	Elapsed time from initial angle to end angle
T	The air temperature
T_s	The sampling period
u_{motor}	Motor control signal
V	Volume of the chamber
y	Linear displacement
$\dot{y}$	Linear speed
$\ddot{y}$	Linear acceleration

y_{dp}	Desired position for the pneumatic DMPC controller
$y_d(k)$	Desired position for the k^{th} sampling instant
$\hat{y}(k)$	Predicted position
$\hat{\dot{y}}$	Predicted velocity
y_f	Butterworth low-pass filtered measured position
y_d	Desired trajectory position
y_{offset}	Offset used to compensate y_d
θ_i	Initial arm angle
θ	Arm angle
$\dot{\theta}$	Arm angular velocity
$\ddot{\theta}$	Arm angular acceleration
θ_{total}	Total angular movement
$\tau_{acc,\max}$	Maximum torque needed to accelerate the arm
$\tau_{gravity}$	Torque needed to overcome gravity
τ_{total}	Total torque
τ_{motor}	Motor torque
$\tau_{motor,max}$	Maximum required motor torque

CHAPTER 1

INTRODUCTION

1.1 Motivation for this research

Pneumatic power is a low cost, clean and safe power source. It also has a high power to weight ratio. That is why it is currently widely used in industry in a variety of applications from simple pneumatic handheld tools to automated assembly processes. However due to the compressibility of the air and nonlinearities of the pneumatic actuators and valves, it is very difficult to precisely model the system. This greatly restricts its use in applications requiring higher precision control. For example, a robotic automation application may use pneumatic power for point to point motion with mechanical stops. This is an example of hard automation that cannot be reconfigured as quickly and inexpensively as systems that are programmable. Today's fast paced industries require programmable control systems to provide greater flexibility, save cost and reduce the waste associated with re-tooling hard automation. Electrically powered actuators are easier to model and control, and are the most commonly used power source in automation and robotics. However, the cost of their components is greater and they have a lower power to weight ratio compared to pneumatic actuators. Because it naturally runs at a high speed with low output torque, an electrical motor must normally be coupled with a gearbox to generate the required torque. This type of arrangement increases the

overall weight and lowers the backdrivability of the system. If the magnitude or direction of motion of an actuator can be easily changed by applying a force or torque to its output shaft then that actuator is known as backdrivable. Low backdrivability contributes to a high impact force if the machine comes into contact with a person (Rooks, 2006). Pneumatic actuators possess a much higher backdrivability due to the compressibility of air, which is an advantage for applications where machines must operate near people, e.g. service robots (Corteville, 2005).

An actuator combining a pneumatic cylinder with an electric motor, forming a single "hybrid pneumatic-electric actuator", could be designed to exploit the advantages of each type of power component. If the cylinder and motor are connected in parallel, the cylinder can overcome the low power to weight ratio of the motor, eliminating the need for a large and costly gearbox. The electrical component can improve the speed and precision of the position control. The hybrid actuator would also possess high backdrivability.

1.2 Objective and organization of the thesis

The objectives of this thesis are to:

1. Design a proof-of-concept prototype of a hybrid pneumatic-electric actuator for a simple robotic arm.
2. Build and test the prototype.
3. Develop a mathematical model of the actuator dynamics.
4. Design and test a model-based position control algorithm.

The organization of the thesis is as follows. In Chapter 2 the literature related to the modeling and control of pneumatic and hybrid pneumatic-electric actuators are reviewed. The design of the prototype actuator is presented in Chapter 3. In Chapter 4, the nonlinear system model is derived. The control algorithm is designed in Chapter 5. Simulations and experiments are presented and discussed in Chapters 6 and 7, respectively. Conclusions and recommendations for future work are presented in Chapter 8.

CHAPTER 2

LITERATURE REVIEW

2.1 Introduction

In this thesis, a prototype hybrid pneumatic-electric actuator will be designed and tested. In addition to the hardware design, this will involve system modeling, and position control algorithm development. The relevant literature is reviewed in this chapter.

2.2 Design of Hybrid Pneumatic-Electric Actuators

The literature on hybrid pneumatic-electric actuators is very limited. The actuators may be connected in series or parallel. The series connection does not increase the output torque, but can produce more accurate positioning. The parallel connection increases the output torque and can provide more accurate positioning, but it is difficult to control.

The concept of a pneumatic-electrical hybrid actuator first appeared in a 1987 U.S. patent (Petrosky, 1987), sponsored by Westinghouse Electric Corp. It was intended to solve the problems of electric motor overheating and low power to weight ratio for high payload applications. This device consisted of an electrical motor and a pneumatic motor connected in parallel. No evidence was found of a commercial device (or even a prototype) being produced. The patent discusses a control algorithm in qualitative terms only.

Mills (1990) proposed an actuator for a robotic joint that consisted of two pneumatic muscle actuators in series with a DC motor. The goal was to achieve independent position control and stiffness control. Simulation results were used to demonstrate the closed-loop control performance. No hardware experiments were included.

The hybrid actuator design proposed by Takemura *et al.* (2000) is the most relevant design from the literature. They connected a rotary pneumatic motor (also known as an air motor) in parallel with a DC motor using gears. The gear ratio between the DC motor and the pneumatic motor was 2:1, *i.e.* the DC motor contributed 1/3 of the output torque while the pneumatic motor contributed 2/3. The output shaft drove the load via a second pair of gears with a 15:1 ratio. The paper does not provide any reasons for these design choices, or details of the mechanical components used. Their control algorithm will be reviewed in section 2.4.

Chiang *et al.*(2005) developed a hybrid actuator consisting of a double rod cylinder and a piezoelectric actuator connected in series. The piezoelectric actuator was attached to the end of the cylinder to make small adjustments (<80 μm) to the endpoint position. If the position error was larger than the range of the piezoelectric actuator, only the pneumatic actuator was engaged. This approach achieved an accuracy of 0.1 μm when both components were active.

2.3 System Modeling

2.3.1 Overview

The hardware for a hybrid pneumatic-electric actuator includes the pneumatic components (air supply, pressure regulator, directional control valve(s), and cylinder), electric components (power supply, amplifier, and DC motor), mechanical components (bearings, gears, payload, etc.), sensors, signal conditioners and controller. Compared with the pneumatic components, the dynamics of the electric components are fast, linear and easily modeled. Therefore the dynamics of the pneumatic components will dominate the system dynamic behaviour. The friction of the cylinder and the flow dynamics through the valve are particularly important, and the relevant literature will now be reviewed.

2.3.2 Friction of the Pneumatic Cylinder

A typical pneumatic system consists of an air supply, pressure regulator, directional control valve, cylinder, sensors and controller. A particular challenge when modelling a pneumatic system is the friction present in the cylinder. When not adequately considered in a position control scheme, friction can cause large steady state position and tracking errors. While friction is very important to include, it is a complex phenomenon that is very difficult to model. Many approaches have been attempted and the most pertinent will be reviewed in this section.

Van Varseveld and Bone (1997) included a simple friction compensator in their control system. Their compensator was based on a Coulomb friction model. This was shown to significantly improve the steady state error. Ning and Bone (2005) monitored the pressure change in cylinder chamber and the piston position, and then estimated the static friction, Coulomb friction and coefficient of viscous friction using a systematic procedure.

Since friction changes as components wear it is necessary to update the model parameters periodically. An alternative is to use an adaptive approach that updates them online. Schindele and Aschemann (2009) developed an adaptive friction compensator based on the LuGre friction model. They applied it to a rodless pneumatic cylinder.

Another approach is to reduce the friction as much as possible to minimize its effect on the system dynamics. Corteville *et al*. (2005) developed a pneumatic cylinder using an air bearing rather than a conventional seal. This method effectively reduced the friction force. Airpot Corporation (2009) has developed a unique pneumatic cylinder using a graphite piston and cylinder lining made from glass. Their design results in very low static friction. This cylinder will be used in the prototype and will be discussed further in Chapter 3.

2.3.3 Pneumatic Valve Modeling

Two main types of valves have been used to control pneumatic cylinders. On/off valves, also known as solenoid valves, and servo valves. Although servo valves are

preferable since they are adjustable over a continuous range, research has been done using on/off valves due to their significantly lower cost.

The majority of servo valve models are based on the model proposed by Shearer (1956). He proposed a nonlinear flow rate model for a four port closed-centre valve derived from the equation for compressible flow through an orifice. Similar models were used by Shen *et al.* (2006) and Nguyen *et al.* (2007), for example. An alternative is to fit a parametric equation to the mass flow rate behaviour. Rao and Bone (2008) fit a bipolynomial in terms of the valve voltage and upstream pressure to the mass flow rate surface. Similar approaches were employed in McDonell and Bobrow (1993), Corteville *et al.* (2005) and Schindele and Aschemann (2009). Ning and Bone (2005) used a mixed approach, extending Shearer's model with several parametric functions. They also presented a method for obtaining the model parameters from simple experiments. Their approach does not require any special hardware.

Modeling on/off valves also involves nonlinear dynamics with the additional complication of the discontinuous switching. In pneumatic control systems, the valve is switched using pulse-width modulation (PWM) to roughly approximate the behaviour of a servo valve. In 1992, Ye *et al.* presented two dynamic models of a PWM-operated pneumatic valve. Their first model was able to predict the discontinuous nature of the mass flow, but was overly complex. For this reason, they introduced a simpler model that predicted the average mass flow. Wang *et al.* (1998) presented another method for modelling an on/off solenoid valve. They first modelled the dead times and switching

times for opening and closing the valve. Next, they fit the parameters of Shearer's model to their experimental data using nonlinear least squares. Shen *et al.* (2006) approximated the dynamics of an on/off valve operating under PWM by averaging the mass flow rates from Shearer's model at the middle of each discrete on/off state.

2.4 Pneumatic Actuator Position Control

Since in this thesis servo valves will not be used in the position control system, only papers using on/off valves will be reviewed. In 1990, Lai *et al.* implemented a system consisting of two pressure regulators and one 3 port – 2 position (3/2) solenoid valve. One chamber of the single-rod cylinder was connected to the first pressure regulator. The pressure in the second chamber was controlled via PWM of the solenoid valve. Their controller employed an inner proportional plus integral (PI) pressure control loop and an outer proportional plus derivative (PD) plus feedforward position control loop. Paul *et al.* (1994) switched two 3/2 valves (each attached to a chamber of a double-rod cylinder) based on a sliding mode control algorithm rather than PWM. Their algorithm was based on a very simplified system model. Their control system achieved a steady-state error (SSE) of 1 mm. Van Varseveld and Bone (1997) developed a controller combining PID, friction compensation, bounded integral action and position feedforward. Their hardware setup consisted of a single-rod cylinder, two 3/2 on/off valves and a linear potentiometer to sense the position of the cylinder piston. A maximum SSE of 0.2 mm and maximum tracking error of 2 mm were achieved. Their experiments also proved the system was robust to 500% changes in the payload mass. Barth *et al.* (2003) proposed

a control method based on PWM and a linearized time-averaged model of the system dynamics. Their hardware included two 3/2 valves and a single-rod cylinder. They employed a frequency domain methodology to design a robust compensator. They achieved an SSE less than 0.5 mm, but large tracking error were also present (greater than 15 mm). Shen *et al.* (2006) extended this research by designing a sliding mode controller based on a time-averaged nonlinear model. They achieved tracking errors less than 3 mm. No SSE results were included. A different sliding mode algorithm was presented by Nguyen *et al.* (2007). Their hardware included four 2-port, 2-position (2/2) solenoid valves. These were configured to give the following three modes of operation: (1) Chamber *A* fills while chamber *B* exhausts, (2) Chamber *B* fills while chamber *A* exhausts, and (3) Neither chamber fills. The controller switched the modes based on the value of a second-order sliding surface. SSE less than 1 mm and tracking errors less than 5 mm were achieved in their experiments.

2.5 Hybrid Pneumatic-Electric Actuator Position Control

In this thesis the prototype hybrid pneumatic-electric actuator will connect a pneumatic cylinder and DC motor in parallel using gears. The only paper that presents a control algorithm for this type of actuator is the work of Takemura *et al.*(2000). This was an extension on their work on air motor control (Pandian *et al.*, 1999). Their hardware design was described in section 2.2. They used two servo valves to control the air flow, an optical encoder to measure the angle of the output shaft, and two pressure sensors. The pressure sensors were used to obtain the pressure difference between the chambers of

the air motor. Since numerically differentiating position twice to obtain acceleration amplifies high frequency noise, they used this differential pressure measurement in their controller as an alternative. They presented two control algorithms: one for point to point (PTP) motion (termed "PTP control") and one for tracking a sinusoidal trajectory (termed "trajectory control"). They designed a sliding mode controller based on a linearized model of the hybrid actuator for the trajectory control mode. For PTP control they defined two phases, "before switching" and "after switching", defined by a threshold value of the position error. During the "before switching" phase the air motor was controller using the sliding mode algorithm and PD control was used with the DC motor. During the "after switching" phase, the servo valves are commanded to exhaust the chambers of the air motor, and the DC motor operates alone (under PD control as before). This strategy may result in increased precision, but has the disadvantage of eliminating the torque contribution of the air motor during part of motion. They included experimental results for step inputs (for PTP motion) and a 0.5 Hz sinusoidal input (for trajectory control). Compared with air motor operating alone (under sliding mode control), the hybrid actuator reduced the settling time from 1.2 s to 0.5 s for the step input, and the maximum tracking error from 10% to less than 5% for the sinusoidal input. Experiments were only performed for horizontal motion.

2.6 Summary

In this chapter, previous related published research on hardware design, system modeling, and position control algorithms was reviewed. Very few designs have appeared in the literature. The most relevant one was published by Takemura *et al.* (2000). They connected an air motor in parallel with a DC motor using gears. Compared to connecting the motors in a serial fashion, connecting them in parallel increases the output torque and can provide more accurate positioning, but it is difficult to control. They used two servo valves to control the air flow. They built and tested a prototype, but did not provide any justification of their design choices.

After the hardware design is complete, it is necessary to model the system dynamics for the purpose of controller development. The pneumatic components will dominate the overall dynamic behaviour. Although various models of cylinder friction have been proposed, accurately modelling friction remains inherently difficult. The flow dynamics through the valve are another critical element of the model. Typically, a physics-based model is combined with empirical parameter estimation.

Due to their complex dynamic behaviour, control of the pneumatic components is much more challenging that DC motor control. Algorithms ranging from classical approaches, e.g. PID control, to nonlinear controllers, e.g. sliding mode control, have been investigated with varying degrees of success. Only one paper has been published on the control of a parallel-connected hybrid pneumatic-electric actuator. Takemura *et al.* (2000) used a combination of PD control and sliding-mode control. Their hybrid actuator

reduced the settling time for a step input from 1.2 to 0.5 s when compared to an air motor.

CHAPTER 3

DESIGN OF THE PROTOTYPE HYBRID PNEUMATIC-ELECTRIC ACTUATOR

3.1 System Overview

A prototype hybrid pneumatic-electric actuator will be designed and built for the purpose of investigating position control algorithms. The actuator will be powered by a pneumatic cylinder and a DC electric motor. Both power components act together in parallel as Figure 3-1 shows. The parallel connection was chosen, rather than the serial connection, since it has potential to provide higher torque in addition to higher positioning precision. This is similar to Takemura *et al.* (2000), except that a pneumatic cylinder is used in this thesis rather than a rotary pneumatic motor. The chosen pneumatic cylinder has the advantage of very low friction compared with rotary pneumatic motors. A further difference is that on/off solenoid valves will be used in this thesis rather than servo valves as was used by Takemura *et al.* (2000). Solenoid valves were chosen since they are available for roughly 5% of the cost of servo valves (e.g. $40 vs. $800 per valve), significantly reducing the overall system cost. The actuator will be used to drive a single degree of freedom robot arm. This arm is capable of rotating in either the horizontal or the vertical plane. A rack and driven gear is used to convert the linear motion of the pneumatic cylinder to rotary motion. The electrical motor transfers torque

to the arm through a pair of gears. The driven gear is supported by rotary bearings, while the rack is guided by a linear slide mechanism. Additional hardware details are provided in section 3.4.

3.2 Design Specifications

The actuator is solely intended as a proof-of-concept prototype. The desired maximum payload is 0.5 kg. To fit within the available lab space the arm must be less than 40 cm long. The arm will move with a range of 0-180º. A variety of equations are used with robots to provide smooth motion trajectories. In this thesis, to determine the maximum torque required, a smooth position trajectory defined by a cycloidal curve (Sindrey and Bone, 2009) will be used, as shown in Figure 3-2.

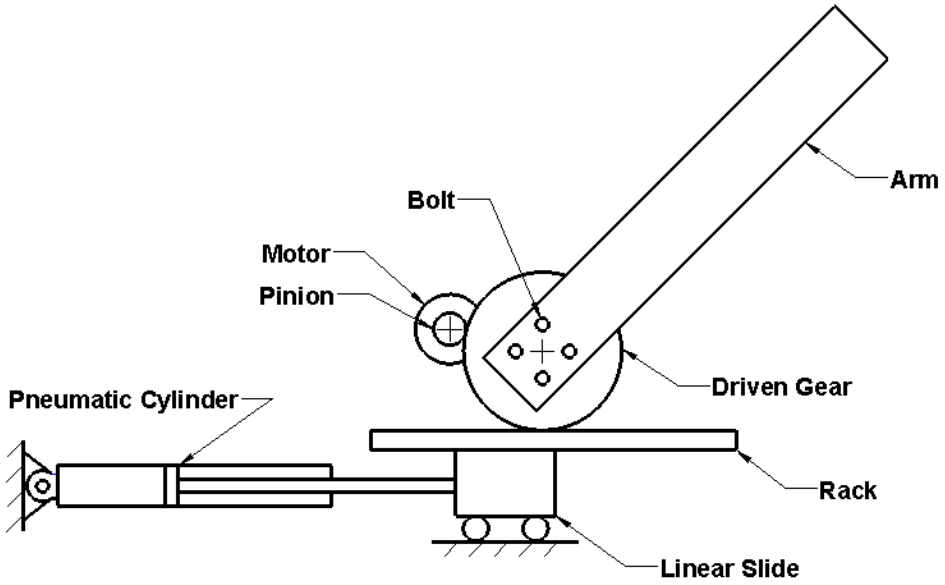

Figure 3-1 Design concept for the pneumatic-electric hybrid actuator.

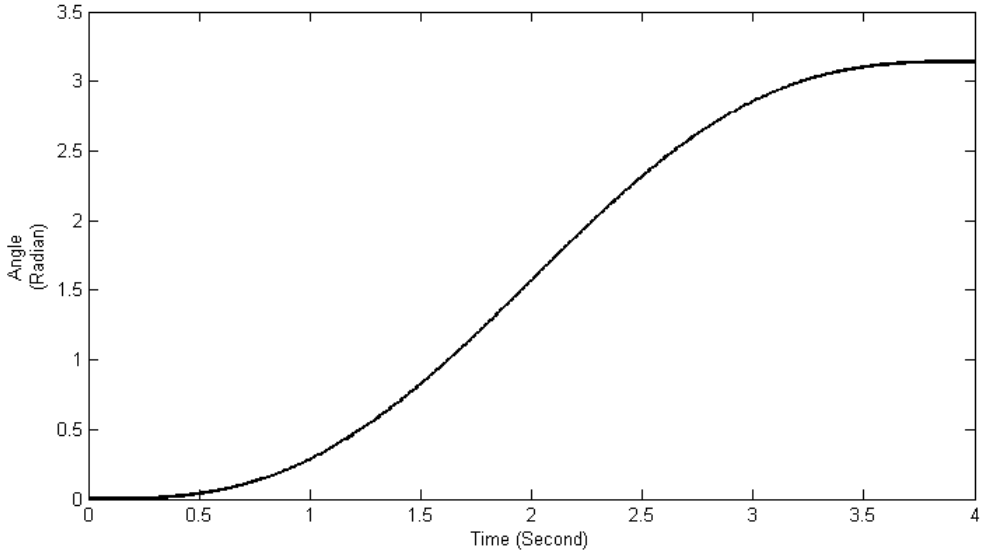

Figure 3-2 Cycloidal trajectory used for actuator.

As mentioned in Chapter 1, the pneumatic actuator should be the primary power source for the hybrid actuator. Following the heuristic proposed by Petrosky (1988), the maximum torque generated by the electrical motor should be about 10% of the maximum torque generated by the pneumatic cylinder.

3.3 Component Selection

3.3.1 Calculation of the Maximum Force Required from Pneumatic Cylinder

To be conservative, in this section it is assumed that the all of the torque is provided by the cylinder alone. The cycloidal curve used to define the arm trajectory has the form:

$$\theta(t) = \theta_i + \theta_{total}\left(\frac{t}{T_e} - \frac{1}{2\pi}\sin\left(2\pi\frac{t}{T_e}\right)\right) \quad \textbf{(3.1)}$$

Where θ (t) is the arm angle at time t, θ_i is initial arm angle, θ_{total} is the total angular movement, and T_e is the elapsed time from initial angle to end angle. The corresponding acceleration is:

$$\ddot{\theta}(t) = \frac{2\pi\theta_{total}}{T_e^{\,2}}\sin\left(2\pi\frac{t}{T_e}\right) \quad \textbf{(3.2)}$$

Because this is only a prototype, fast motion may be unsafe, and the elapsed move time is set to: $T_e = 4$ s . Substituting $t = \frac{1}{4}T_e = \frac{1}{4}(4\text{s})=1$ s into (3.2) gives the maximum acceleration:

$$\ddot{\theta}_{\max} = \ddot{\theta}\left(\tfrac{1}{4}T_e\right) = \frac{2\pi\theta_{total}}{T_e^2} = 1.23\ \text{rad/s}^2 \quad \textbf{(3.3)}$$

The arm will be made from an aluminum beam with approximate dimensions 39 x 5 x 1 cm. Its measured mass is $m_{arm} = 0.5kg$, and its moment of inertia is:

$$I_{arm} = \tfrac{1}{3}m_{arm}L_{arm}^2 = \tfrac{1}{3}(0.5\text{ kg})(0.35\text{ m})^2 = 0.0204\ \text{kgm}^2 \quad \textbf{(3.4)}$$

Where L_{arm} is the effective length of the arm. Note that L_{arm} is less than the length of the beam since the pivot point is inset from the end as shown in Figure 3-1. A maximum mass of 0.5 kg will be added to the end of the arm as a payload. The inertia of this payload mass, $m_{payload}$, is:

$$I_{payload} = m_{payload}L_{arm}^2 = (0.5\text{ kg})(0.35\text{ m})^2 = 0.0613\ \text{kgm}^2 \quad \textbf{(3.5)}$$

The torque required to accelerate the arm is:

$$\tau_{acc}(t) = \left(I_{arm} + I_{payload}\right)\frac{2\pi\theta_{total}}{T_e^{\,2}}\sin\left(2\pi\frac{t}{T_e}\right) \quad \textbf{(3.6)}$$

The maximum torque needed to accelerate the arm is then:

$$\tau_{acc,\max} = \left(0.0204\,\text{kgm}^2 + 0.0613\,\text{kgm}^2\right)\left(1.23\,\text{rad/s}^2\right) = 0.100\,\text{Nm} \quad \textbf{(3.7)}$$

When the arm moves in the horizontal plane the maximum required torque equals τ_{acc}. For motion in the vertical plane the torque needed to overcome gravity must be added. Because it is a uniform beam, the centre of mass of the arm is at its midpoint. The angle θ is defined such that it is zero when the arm is positioned vertically downward, and $\frac{\pi}{2}$ when it is horizontal. Therefore the torque needed to overcome gravity is:

$$\tau_{gravity} = \left(\tfrac{1}{2}m_{arm}L_{arm} + m_{payload}L_{arm}\right)g\sin\left(\theta\right) \quad \textbf{(3.8)}$$

and the total torque required is:

$$\tau_{total} = \tau_{acc} + \tau_{gravity} \quad \textbf{(3.9)}$$

To study the behaviour of the torques, equations (3.1)-(3.8) were programmed in Matlab. As shown by the plot in Figure 3-3, the maximum required torque is: $\tau_{\max} = 2.73$ Nm.

To require the least amount of force from the cylinder the driven gear should have as large a diameter as possible. However, a very large gear would be impractical for robotic applications, plus it would require a very large cylinder stroke. For a standard

stroke of 5 inches (127 mm), and a 180° range of motion, a suitable gear pitch diameter is $d_{pitch} = 75mm$. The total maximum required force is then given by:

$$F_{\max} = \frac{\tau_{\max}}{\frac{1}{2}d_{pitch}} = \frac{2.73\ \text{Nm}}{\frac{1}{2}(0.075\ \text{m})} = 72.8\ \text{N} \qquad \textbf{(3.10)}$$

The driven gear and arm subassembly is shown in Figure 3-4. The complete mechanical assembly, set up for motion in the vertical plane, is shown in Figure 3-5.

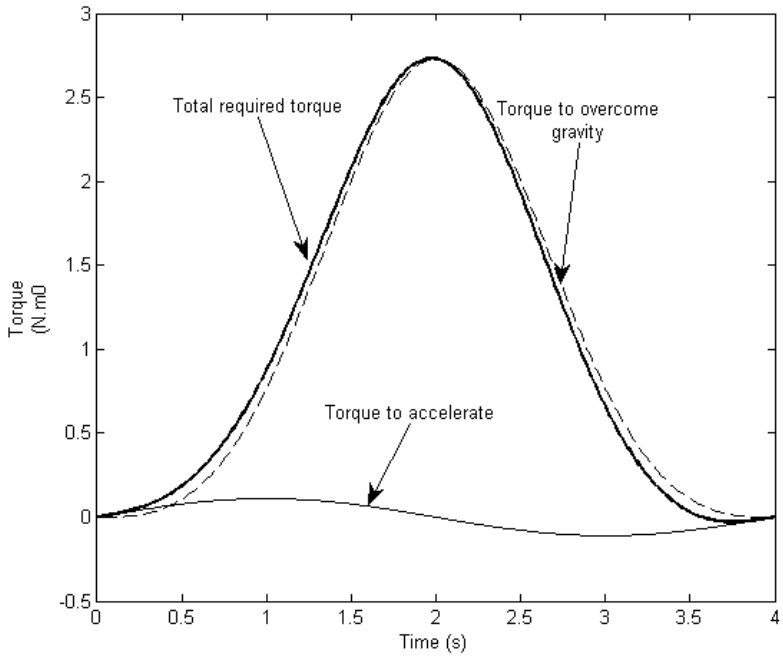

Figure 3-3 Torques from equations (3.1)-(3.8) plotted over the cycloidal trajectory.

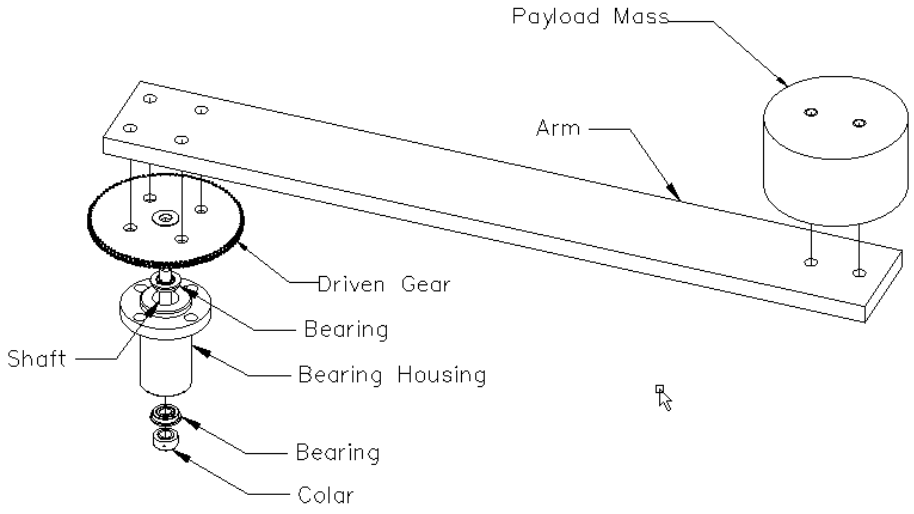

Figure 3-4 Driven gear and arm subassembly.

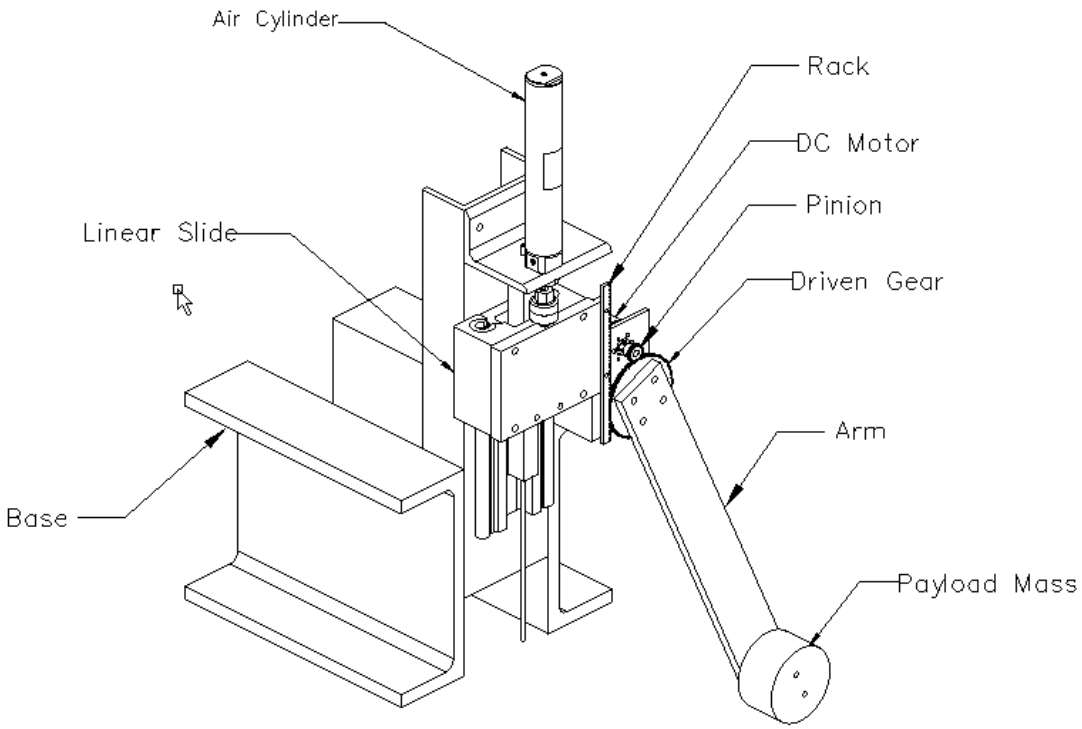

Figure 3-5 Mechanical assembly drawing.

From Figure 3-5, the total required force is supplied by the combination of the cylinder force and the gravity force acting on the block of the linear slide. The mass of this block is $m_{block} = 1.17kg$. So the maximum force required from the cylinder is

$$F_c = F_{\max} - m_{block} g = 72.8 \text{ N} - (1.17 \text{ kg})(9.8 \text{ N/kg}) = 61.33 \text{ N} \quad \textbf{(3.11)}$$

3.3.2 Selection of Cylinder, Motor and Gears

The first step will be to select the bore diameter of the cylinder. The relationship between bore diameter and cylinder force is:

$$F_c = P_c \frac{\pi}{4} d_{bore}^2 \quad \textbf{(3.12)}$$

or:

$$d_{bore} = \sqrt{\frac{4F_c}{\pi P_c}} \quad \textbf{(3.13)}$$

where d_{bore} is the bore diameter and P_c is the gauge pressure inside the cylinder. where P_s is the supply pressure. A supply pressure $P_s = 0.15$ MPa gauge will be used in this thesis. This relatively low pressure (*i.e.* 0.6 MPa gauge is typical with pneumatic systems) was chosen to ensure safe operation of the prototype. Assuming the supply pressure losses are negligible, substituting F_c from (3.10) into (3.12), the minimum required bore diameter is:

$$d_{bore,\min} = \sqrt{\frac{4F_c}{\pi P_c}} = \sqrt{\frac{4(61.33\text{N})}{\pi(0.15 \text{ MPa})}} = 22.8 \text{ mm} \quad \textbf{(3.14)}$$

To limit the size and weight of the actuator the bore diameter should be selected as close as possible to $d_{bore,min}$. For precise position control a cylinder with low friction is highly desirable. For these reasons an Airpel anti-stiction cylinder was selected. Its outer stainless steel housing contains a glass liner. The piston seal is graphite. As a result of these materials it has very low static and dynamic friction. Its specifications are listed in Table 3-1.

Table 3-1 Specifications of the selected pneumatic cylinder

(Airpot Corporation, 2009)

Manufacturer	Airpot
Model	Airpel E24D5.0N
Stroke (mm)	127
Bore (mm)	24.13
Rod Diameter (mm)	6.35

The DC electric motor will now be selected. As previously stated in Section 3.2, the maximum torque from the motor should be about 10% of the maximum torque supplied by the pneumatic cylinder. The required motor torque depends on the pitch diameter of the pinion gear, d_{pinion}. To allow a smaller and lighter motor to be used, d_{pinion} should be as small as possible. Its lower limit is determined by the strength of its teeth. Following the standard tooth stress calculations (described further in Appendix A),

the smallest size able to deliver the required torque was metric module 0.75. Since at least 20 teeth are required for smooth meshing, the chosen pitch diameter was: d_{pinion} =20 x 0.75 mm = 15 mm. The specifications of the chosen gears are listed in Table 3-2. Since the motor must supply approximately 10% of the torque to the driven gear, the maximum required motor torque is:

$$\tau_{motor,max} \approx 0.1\tau_{\max}\frac{d_{pinion}}{d_{pitch}} = 0.1(2.73\text{ N})\left(\frac{15\text{ mm}}{75\text{ mm}}\right) = 0.055\text{ Nm} \quad \textbf{(3.15)}$$

A RE40 motor from Maxon was selected. Table 3-3 lists the specifications of this motor. Its torque output equals its torque constant (0.060 Nm/A) times its input current. Its maximum continuous torque equals 0.11 Nm. In practice the torque is limited by the electrical hardware. An amplifier converts the control signal from the computer into the current that drives the motor. The available motor amplifier had a gain of: $K_{amp} = 0.2\text{A / V}$. The maximum voltage output from the computer control board was 5V, so the maximum torque that the motor could continuously generate was: 0.060 Nm/A x 0.2A/V x 5V = 0.06 Nm.

Table 3-2 Specifications of the selected driven gear and pinion (SDP/SI, 2009)

	Driven Gear	**Pinion**
Manufacturer	SDP/SI	SDP/SI
Part Number	A 1B 2MYKH7100	A 1B 2MYKH7020
Module (mm)	0.75	0.75
Number of teeth	100	20
Pitch Diameter (mm)	75	15
Material	Brass	Brass

Table 3-3 Specifications of the selected DC motor (Maxon Motor, 2009)

Manufacturer	Maxon
Model	RE40
Order Number	148877
Torque Constant, K_t (Nm/A)	0.060
Max. Continuous Current (A)	1.9
Max. Continuous Torque (Nm)	0.11

3.4 Control System Hardware

The hardware is shown schematically in Figure 3-6. One 3-way on/off solenoid valve is connected to each port of the cylinder. This allows the inflow and outflow of air to be controlled. Two pressure sensors measure the air pressure at each port of the cylinder. A linear potentiometer measures the position of the cylinder. A PC-based data acquisition and control system reads the sensor measurements and sends control signals to the pneumatic valve solenoids (via optocouplers) and electrical motor (via the amplifier).

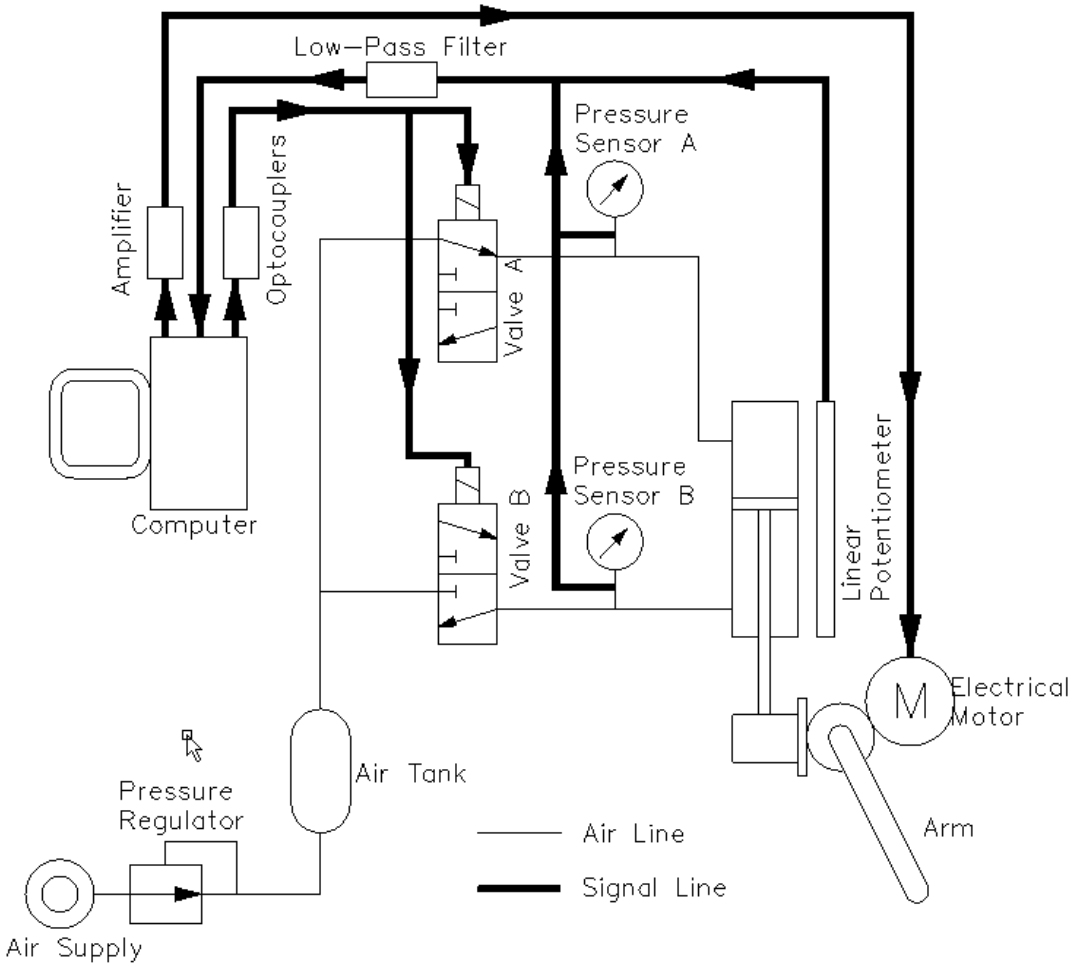

Figure 3-6 Schematic of the control system hardware.

The on/off valves are fast switching solenoid valves made by MAC, model number 34B-AAA-GDFB-1BA. These valves were selected since they performed very well in prior pneumatic position control research (van Varseveld and Bone, 1997). The linear potentiometer is made by Novotecnik, model number T100 with a range of 0-100 mm. The pressure sensors are made by Omega Engineering, model number PX138-

030D5V. They have a differential pressure range of ±30 psi (±0.21 MPa gauge). All of the sensors are interfaced with the computer (Pentium III 500 MHz) through a Quanser MultiQ3 I/O board. The PC is programmed in C and a 1000 Hz sampling frequency is used.

3.5 Signal Conditioning

Significant noise was observed in the raw pressure sensor signals. The noise in the signal is caused by the built-in amplifier of the sensors, the power supply and the quantization effect of the analog to digital conversion process. To reduce the noise amplitude, both pressure sensor signals are hardware low-pass filtered before being sampled by the MultiQ3 board. The raw linear potentiometer signal contained only a small amount of noise. For this reason, rather than adding the complexity of wiring and powering another hardware filter, the potentiometer signal was filtered digitally as part of the computer control program. The bandwidth of a typical pneumatic servo system is around 5 Hz. A low-pass filter with a cut-off frequency of 50 Hz (*i.e.* 10 times greater than the expected bandwidth) was chosen to remove most of the high frequency noise while not adding significant phase lag to the feedback loop. Each hardware filter IC is an 8^{th}-order low-pass Bessel filter. They were made by Maxim Integrated Products, part number MAX292CPA+. For the potentiometer, a 2^{nd}-order digital Butterworth filter was programmed in C. To demonstrate the effectiveness of the filters, plots of the raw and filtered signals are provided in Figure 3-7. The plots show that the pressure noise spikes

were reduced from 10 kPa to less than 1 kPa by the filter. Similarly, the displacement noise amplitude was reduced from approximately 0.1 mm to 0.05 mm.

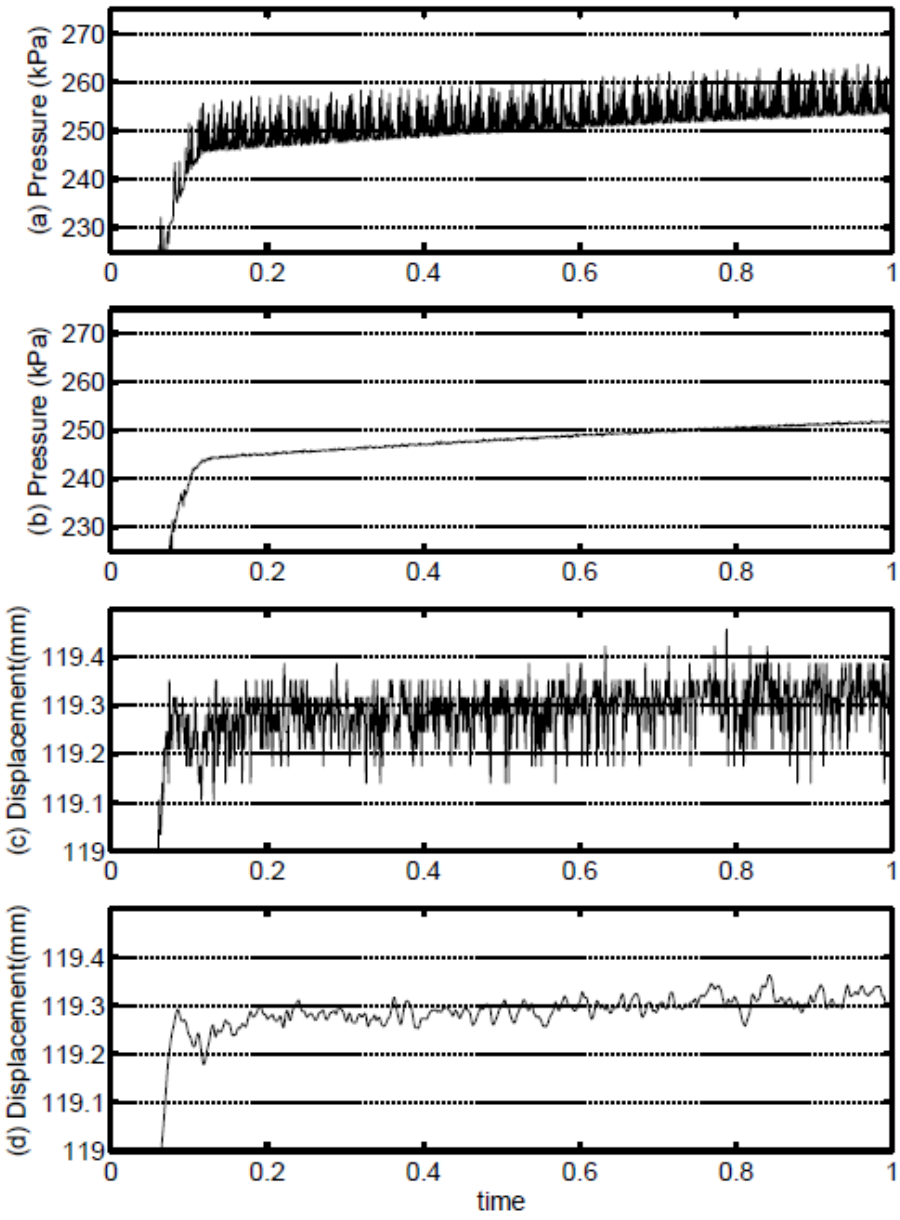

Figure 3-7 Filtered sensor signals: (a) raw pressure, (b) filtered pressure, (c) raw displacement, and (d) filtered displacement.

3.6 Summary

In this chapter, the design of a proof-of-concept prototype hybrid pneumatic-electrical actuator was described. The maximum required torque was derived from the desired position trajectory. The pneumatic cylinder, electric motor and gears were sized to satisfy this requirement. Details of the sensors and other control system hardware were provided. The next chapter will discuss the mathematical modeling of this system.

CHAPTER 4

SYSTEM MODELING

4.1 Introduction

A dynamic model provides the foundation for control design. In this chapter, a mathematical model of the actuator dynamics is derived, including the pneumatic cylinder, pneumatic valves, DC motor and mechanical elements. Since the main power input comes from the pneumatic cylinder and the position is measured by the linear potentiometer, the system model will be developed with respect to the motion of the block on the linear slide.

4.2 System Dynamic Model

In this section the overall system model will be derived. The assembled mechanical components are shown in Figure 4-1. A free body diagram of the mass equivalent to the inertias of the arm, payload and block, termed m_{eq}, is shown in Figure 4-2. The total applied force is:

$$F_{total} = F_{cylinder} + F_{gravity} + F_{motor} - F_{friction} \quad \textbf{(4.1)}$$

where $F_{cylinder}$ is the force applied by the cylinder, $F_{gravity}$ is the total force due to gravity, F_{motor} is the force applied by the DC motor, and $F_{friction}$ is the total friction force. The system dynamics equation is then:

$$\ddot{y} = \frac{F_{total}}{m_{eq}} \tag{4.2}$$

The equations for the terms in (4.1) and (4.2) will be derived in the proceeding sections.

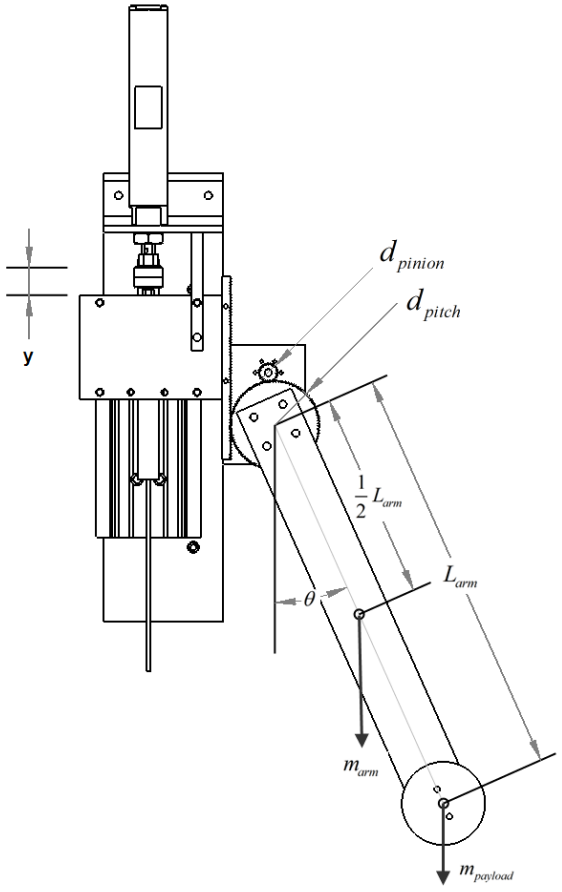

Figure 4-1 System mechanical elements.

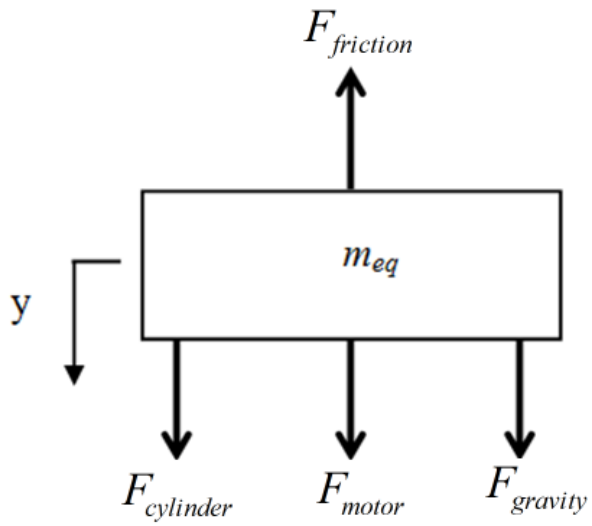

Figure 4-2 Free body diagram of m_{eq}.

4.3 Dynamics of the Cylinder, Arm and Motor

4.3.1 Cylinder Force

The force produced by the cylinder is dependent on the pressure inside each chamber and the associated piston cross-sectional area. This relationship is:

$$F_{cylinder} = P_a A_a - P_b A_b \tag{4.3}$$

where $F_{cylinder}$ is the force generated by the cylinder, P_a is the absolute pressure inside chamber A, P_b is the absolute pressure inside chamber B, A_a is the piston area in chamber A, and A_b is the piston area in chamber B. The equation used to obtain the chamber pressures is presented in section 4.5.1.

4.3.2 Gravity Force

It is assumed that the masses and inertias of small components such as the gears can be neglected without significant loss of accuracy. This leaves the arm, payload mass and block of the linear slide (recall Figure 3-5 Mechanical assembly drawing.). The torque required to balance gravity acting on the arm and payload was given in (3.7). The relationship between the arm angle and block displacement is simply:

$$\theta = \frac{y}{\frac{1}{2} d_{pitch}} \tag{4.4}$$

where θ is the arm angle in radians, y is the position of the block of the linear slide, and d_{pitch} is the pitch diameter of the driven gear. The equivalent forces for each element are then:

$$\begin{aligned} F_{arm} &= -\frac{\frac{1}{2} m_{arm} L_{arm} g \sin(\theta)}{\frac{1}{2} d_{pitch}} \\ &= -\frac{\frac{1}{2} m_{arm} L_{arm} g \sin\left(\frac{2y}{d_{pitch}}\right)}{\frac{1}{2} d_{pitch}} \end{aligned} \tag{4.5}$$

And

$$\begin{aligned} F_{payload} &= -\frac{m_{payload} L_{arm} g \sin(\theta)}{\frac{1}{2} d_{pitch}} \\ &= -\frac{m_{payload} L_{arm} g \sin\left(\frac{2y}{d_{pitch}}\right)}{\frac{1}{2} d_{pitch}} \end{aligned} \tag{4.6}$$

where F_{arm} is the equivalent gravity force for the arm, $F_{payload}$ is the equivalent gravity force for the payload, and L_{arm} is the length of the arm. For the block of the linear slide:

$$F_{block} = m_{block} g \tag{4.7}$$

where F_{block} is the gravity force for the block, and m_{block} is the mass of the block. Finally, the total gravity force is

$$F_{gravity} = F_{arm} + F_{payload} + F_{block} \tag{4.8}$$

4.3.3 DC Motor Torque and Force

The relationship between the torque generated by the DC motor and the motor control signal from the PC can be expressed by the equation:

$$\begin{aligned} \tau_{motor} &= K_t i_m \\ &= K_t K_{amp} u_{motor} \end{aligned} \tag{4.9}$$

where τ_{motor} is the motor torque, K_t is the torque constant of the motor, K_{amp} is the amplifier gain, u_{motor} is the motor control signal, and i_m is the supplied current. Note that (4.9) assumes the relationship between u_{motor} and i_m can be represented by a gain. This is a reasonable assumption since the inductance of the RE40 motor is only 0.3 mH, and a current mode amplifier circuit is used. The force transmitted via the gears to the block is:

$$\begin{aligned} F_{motor} &= \frac{\tau_{motor}}{\frac{1}{2} d_{pinion}} \\ &= \frac{K_t K_{amp} u_{motor}}{\frac{1}{2} d_{pinion}} \end{aligned} \tag{4.10}$$

Recall from Chapter 3, that for our amplifier $K_{amp} = 0.2 \text{ A / V}$, and the torque constant given by the motor manufacturer is $K_t = 0.060 \text{ Nm / A}$ (Maxon Motor, 2009). Note than any friction caused by the motor will be included in the overall friction model described in section 4.4.

4.3.4 Equivalent Mass

The force required to accelerate the block, arm and payload is

$$F_{acc} = m_{block}\ddot{y} + \frac{\left(I_{arm} + I_{payload}\right)\ddot{\theta}}{\frac{1}{2}d_{pitch}} \tag{4.11}$$

and the relationship between the linear and angular accelerations is

$$\ddot{\theta} = \frac{\ddot{y}}{\frac{1}{2}d_{pitch}} \tag{4.12}$$

From(4.11), (4.12) and Newton's second law:

$$\begin{aligned} m_{eq} &= \frac{F_{acc}}{\ddot{y}} \\ &= m_{block} + \frac{\left(I_{arm} + I_{payload}\right)\ddot{\theta}}{\frac{1}{2}d_{pitch}} \frac{1}{\frac{1}{2}d_{pitch}\ddot{\theta}} \\ &= m_{block} + \frac{I_{arm} + I_{payload}}{\frac{1}{4}d_{pitch}^2} \end{aligned} \tag{4.13}$$

where I_{arm} and $I_{payload}$ may be obtained using (3.4) and (3.5), respectively.

4.4 Friction Forces

4.4.1 Overview

Static friction is present in the prototype between the block and rail of the linear slide, piston and cylinder barrel, rod and its seal, and the meshing gears. The rotary bearing supporting the driven gear and the linear potentiometer also contribute to the total friction force. In equation form the friction is:

$$F_{friction} = \begin{cases} F_{cylinder} + F_{gravity} + F_{motor} & \dot{y} = 0,\ F_{cylinder} + F_{gravity} + F_{motor} \le F_{sf} \\ F_{cf}\, sign(\dot{y}) + C_{vf}\, \dot{y} & \dot{y} \neq 0 \end{cases} \quad \textbf{(4.14)}$$

where $F_{friction}$ is the total friction force, F_{cf} is the Coulomb friction force, F_{sf} is the static friction force, C_{vf} is the coefficient of viscous friction, and $\dot{y}$ is the velocity of the block.

4.4.2 Static Friction Force

The static friction force, F_{sf}, is the maximum force that can be applied to the stationary block before it starts to move. The challenge when measuring static friction is determining exactly the instant when the movement starts. To detect this instant an aluminum "contact bar" was rigidly attached to the block as shown in Figure 4-4. The bracket shown was connected to the electrical ground. The bar was electrically isolated from the slide so that its electrical state could be used to detect whether it was in contact with the bracket. The bar was wired to one of the digital input pins of the Quanser

MultiQ3 I/O board. The pin has an internal pull-up resister so that it has a logic TRUE state when disconnected and a logic FALSE state when grounded. When the bar is in contact with the bracket the logic state will be FALSE. When the block starts to move, contact will be lost, and the logic state will become TRUE. To detect the instant contact is lost the state of this pin is read with a sampling rate of 1000 Hz. Prior to each test the cylinder was de-pressurized. To initiate the movement, the air pressure in the cylinder was gradually increased by manually opening the pneumatic regulator. The force at the instant contact was lost (*i.e.* F_{sf}) was estimated by substituting the measured pressures into (4.1). Ten tests were performed with the contact bar bolted to the block as shown in Figure 4-3. The contact bar was repositioned, and a further ten tests were performed. The results are tabulated in Table 4-1. The mean of these values, 1.4 N, will be used as the static force estimate.

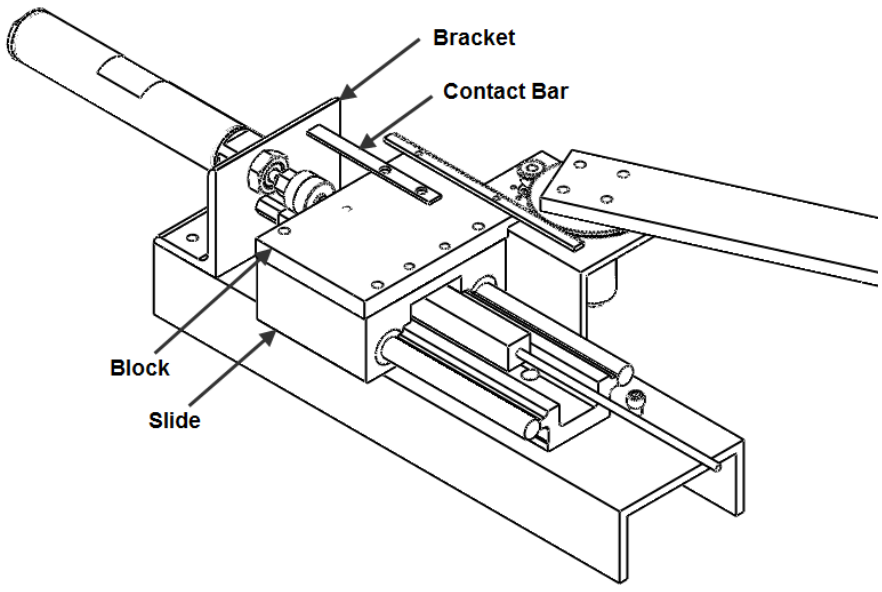

Figure 4-3 Static friction test setup

Table 4-1 Static friction test results.

Test No.	Position No.	Static Friction Force Estimate (N)
1	1	1.72
2	1	1.19
3	1	1.16
4	1	1.67
5	1	1.72
6	1	1.68
7	1	1.30
8	1	1.35
9	1	1.39
10	1	1.80
11	2	1.24
12	2	1.84
13	2	1.56
14	2	1.51
15	2	0.99
16	2	0.94
17	2	1.59
18	2	1.68
19	2	1.72
20	2	0.94

4.4.3 Coulomb and viscous friction

To find the Coulomb and viscous friction, a different test setup was used. If the prototype is oriented to move in the horizontal plane and the block of the linear slide is moving at a constant speed, the applied cylinder force should equal the Coulomb and viscous friction forces, *i.e.*

$$F_{cylinder} = F_{cf}\, sign(\dot{y}) + C_{vf}\, \dot{y} \tag{4.15}$$

If two tests are performed at different positive velocities, then (4.15) produces two equations which can be solved for F_{cf} and C_{vf} as follows:

$$C_{vf} = \frac{F_1 - F_2}{\dot{y}_1 - \dot{y}_2} \quad \text{when } \dot{y}_1 \neq \dot{y}_2 \text{ and} \tag{4.16}$$

$$F_{sf} = F_1 - C_{vf}\, \dot{y}_1 \tag{4.17}$$

where $\dot{y}_i$ is the velocity and F_i is the corresponding cylinder force estimated using the pressure measurements and(4.1). The pneumatic regulator was set to provide a small $F_{cylinder}$ value so that steady-state velocity would be reached quickly. Two pressure settings were used, and ten tests were run at each pressure setting. The results are listed in Table 4.2. The mean values from Table 4-2 are: $\dot{y}_1 = 0.263$ m/s, $\dot{y}_2 = 0.250$ m/s, F_1 = 2.16 N and F_2 = 2.10 N. Substituting these into (4.16) and (4.17) gives: F_{cf} = 0.97 N and C_{vf} = 4.5 N/m/s.

Table 4-2 Dynamic friction test results.

Test No.	Set No.	Velocity (m/s)	Cylinder Force (N)
1	1	2.59	1.51
2	1	2.60	1.51
3	1	2.62	1.49
4	1	2.64	1.51
5	1	2.83	1.54
6	1	2.67	1.57
7	1	2.56	1.55
8	1	2.61	1.58
9	1	2.58	1.67
10	1	2.60	1.66
11	2	2.55	2.12
12	2	2.60	2.14
13	2	2.46	2.04
14	2	2.46	2.12
15	2	2.61	2.06
16	2	2.45	2.08
17	2	2.46	2.12
18	2	2.45	2.04
19	2	2.62	2.16
20	2	2.69	2.19

4.5 Pneumatic Component Modeling

4.5.1 Chamber Pressure Dynamics

Applying the first law of thermodynamics and the ideal gas law to each of the cylinder chambers gives:

$$v\dot{P} + kP\dot{v} = kRT\dot{m} \tag{4.18}$$

where $\dot{m}$ is the mass flow rate into the chamber, v is the volume of the chamber, k is the ratio of specific heats of air, R is the universal gas constant, and T is the air temperature. Each chamber volume depends on its dimensions and the piston position as follows:

$$v_a = (y_{a0} + y)A_a \text{ and} \tag{4.19}$$

$$v_b = (y_{b0} - y)A_b \tag{4.20}$$

where y_{a0}=0.008 m and y_{b0}=0.122 m for the cylinders used in the prototype. Similarly the time derivative of the volumes are given by

$$\dot{v}_a = \dot{y}A_a \text{ and} \tag{4.21}$$

$$\dot{v}_b = \dot{y}A_b \tag{4.22}$$

4.5.2 Valve Filling and Discharging Modeling

Before deriving the mathematical model of the valve a simple test was performed to observe its dynamic characteristics. To maximize the chamber volume the cylinder position was fixed at the end of its stroke. The initial pressure inside the chamber was

atmospheric. The valve was opened to fill the chamber with air. When the chamber pressure reached the supply pressure, the valve was switched to exhaust the air. Figures 4-4 to 4-6 show the test data. The valve control signal is set to 'fill' at time 1 s and set to 'discharge' at time 9 s.

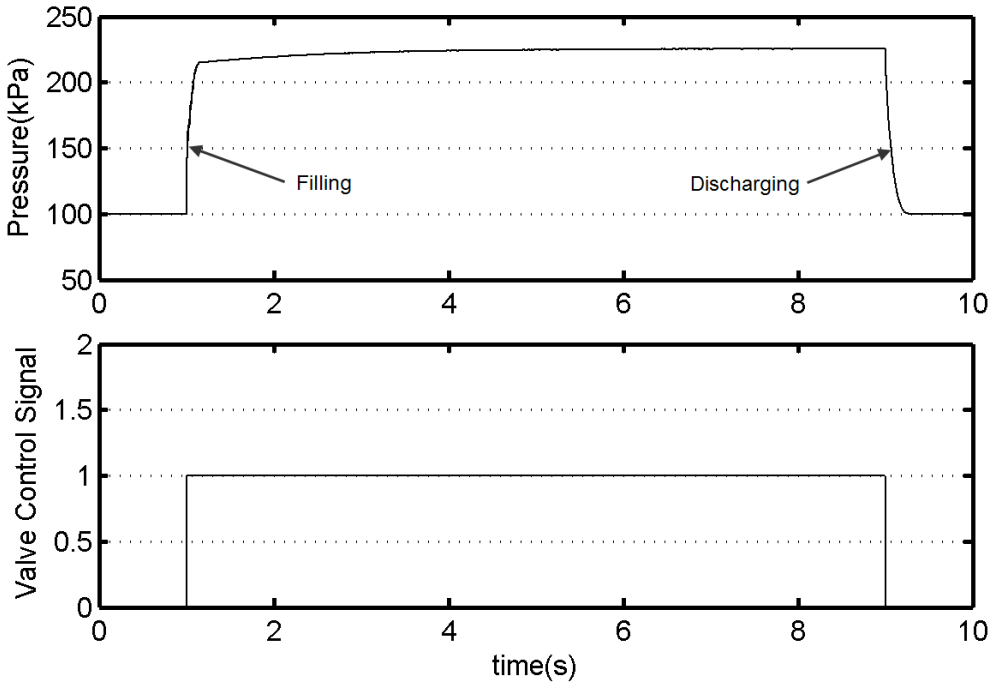

Figure 4-4 Valve filling discharging test.

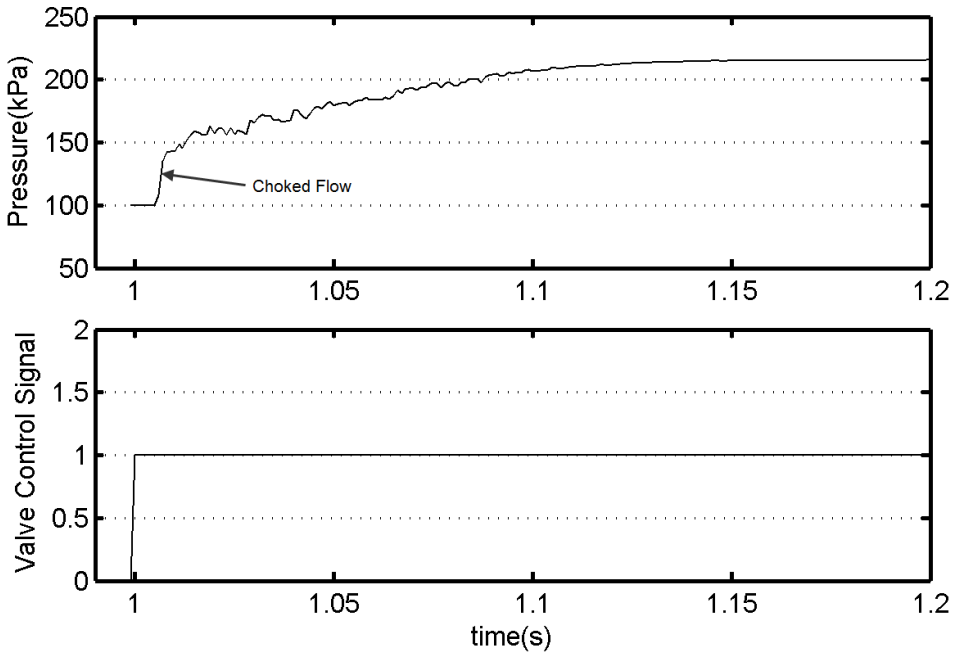

Figure 4-5 Close-up of the filling dynamics from the data shown in Figure 4-4.

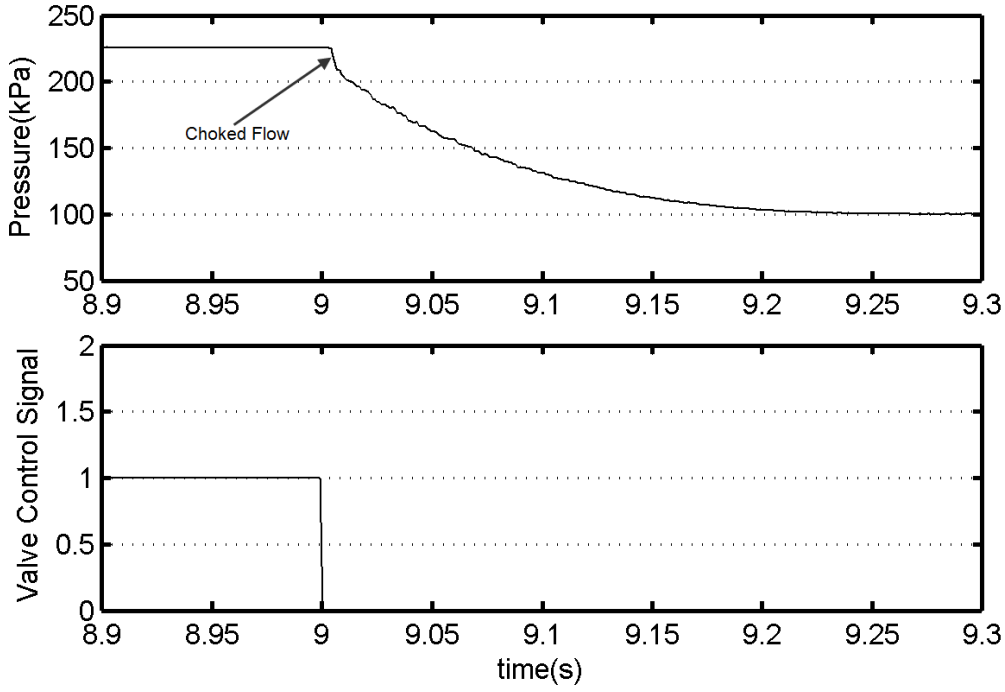

Figure 4-6 Close-up of discharging dynamics from the data shown in Figure 4-4.

Figure 4-4 shows the overall process of filling and discharging. Figure 4-5 is a close-up of the pressure change during filling. Figure 4-6 is a close-up of the pressure change during discharging.

It can be observed from Figure 4-5 and Figure 4-6 that a delay in the pressure exists indicating a delay between the solenoid receiving the control signal and the motion of the valve spool. This will be further discussed in the next section.

During the filling and discharge processes the flow can be characterized by two distinct dynamic behaviours: choked flow and unchoked flow. At the beginning of both charging and filling, there is an approximately linear segment with a steep slope indicating a rapid change in pressure. The flow during these segments is choked. According to Jones and Hawkins (1986), for an ideal gas, choked flow is determined by the ratio between upstream pressure, P_{up}, and downstream pressure, P_{down}. The condition (4.23) indicates when choked flow occurs with air. If the condition does not hold then the flow is unchoked.

$$\frac{P_{down}}{P_{up}} \leq 0.53 \tag{4.23}$$

With choked flow the mass flow rate $\dot{m}$ is constant. In the experimental setup, since the piston is fixed, $\dot{v} = 0$. Now (4.18) can be rewritten in the simplified form:

$$\dot{m} = \frac{v\dot{P}}{kRT} \tag{4.24}$$

where $\dot{m}$ is the mass flow rate into the chamber, v is the volume of the chamber (in the experimental setup $v = 5.03\times10^{-5}$ m^3), and $\dot{P}$ is the time derivative of the

pressure inside the chamber. The average slope of the choked segments in Figure 4-5 and 4-6 equals 13.5 MPa/s. Substituting the numerical values into (4.24) yields:

$$\begin{aligned}\dot{m} &= \frac{v\dot{P}}{kRT} \\ &= \frac{(5.03\times10^{-5}\,\mathrm{m}^3)(13.5\times10^{6}\,\mathrm{Pa/s})}{(1.4)(287\ \mathrm{Jkg/K})(293\mathrm{K})} \\ &= 0.0061\ \mathrm{kg/s}\end{aligned} \tag{4.25}$$

For unchoked flow, simplified versions of Shearer's equations (Shearer, 1956) will be used. For filling:

$$\dot{m} = c_{fill}\sqrt{P_s - P} \tag{4.26}$$

where c_{fill} is the filling coefficient. For discharging:

$$\dot{m} = c_{dis}(P_0 - P) \tag{4.27}$$

where c_{dis} is the discharging coefficient, and P_0 is the atmospheric pressure. Curve fitting (4.26) and (4.27) to the data shown in the figure produced the coefficients: $c_{fill} = 1.5 \times 10^{-6}$ kg/s/Pa and $c_{dis} = 6.3 \times 10^{-9}$ kg/s/Pa^{½}. Figure 4-7 compares simulation results with actual test data. The chamber pressure was simulated by numerically integrating $\dot{P}_a$ from (4.18) using Euler's method. The root mean square error was 2.42 kPa. This indicates that the c_{fill} and c_{dis} values are reasonably accurate.

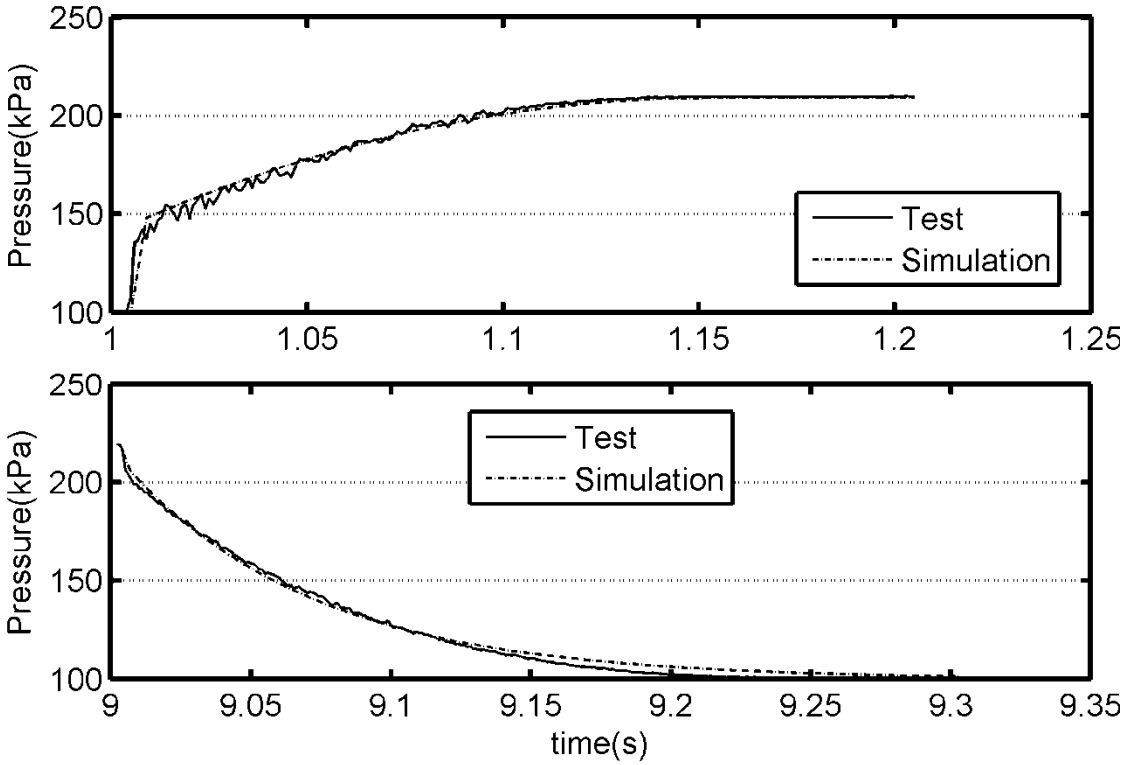

Figure 4-7 Comparison of simulated and measured charging (top) and discharging (bottom) pressure vs. time curves.

4.5.3 Valve Delay

According to the specification of the valves (MAC, 2009), there should be a delay of 3.5ms when the valve solenoid is energized and a 1.4ms delay when it is de-energized. Since the sampling rate is 1000 Hz, the data acquisition and control system cannot respond to changes that occur within a time interval smaller than 1 ms. So the expected energize/de-energize delays will be rounded to 1 ms and 4 ms, respectively. To verify the valve control delays, the piston of the cylinder was fixed to the middle of its stroke. A pseudo random binary signal (PRBS) was sent to valve *A* (see Figure 3-6) causing it to

open and close at pseudo random intervals. The pressure in chamber *A* was simultaneously sampled and saved. Figure 4-8 shows a portion of the test data.

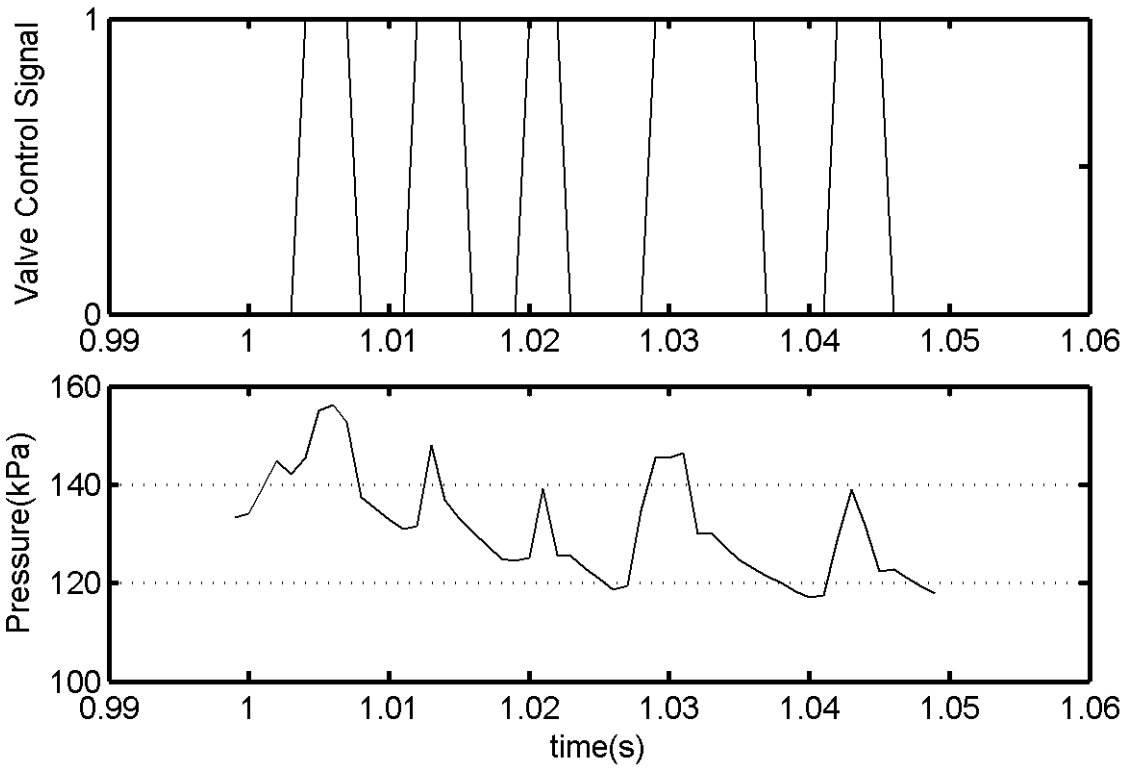

Figure 4-8 Valve delay test data

By inspecting the recorded data and comparing the times the control signal changed with the times the pressure started to increase, the energizing delay between the valve control signal and pressure change was estimated to be 4 ms, confirming the expected value. Employing the same method, the de-energizing delay was confirmed to be 1 ms.

4.6 Summary

In this chapter, a mathematical model was developed of the system dynamics, including the pneumatic cylinder, pneumatic valves, DC motor and mechanical elements. The structure of the equations was based on physical principals and then the parameters were either estimated from experimental data, or obtained from the manufacturer's specifications. The model forms a key part of the controller presented in the next chapter.

CHAPTER 5

CONTROL SYSTEM DEVELOPMENT

5.1 Introduction

In this chapter, the design of a position control algorithm for the hybrid actuator will be investigated. In the first section, a model-based controller is designed for the pneumatic cylinder. This is followed by preliminary testing and additions to the algorithm to improve its performance. Next, two control algorithms for the DC motor are presented. The chapter concludes with a summary.

5.2 Pneumatic Cylinder Control Algorithm

5.2.1 Selection of Control Algorithm

As discussed in Chapter 2, most of the pneumatic systems using solenoid valves used PWM to approximate the continuously adjustable behaviour of a servo valve. The disadvantage of this approach is that the sampling period of the controller must be several times longer than the switching time of the valve for the PWM to have adequate duty cycle resolution. With the hybrid actuator this could make the sampling period for the pneumatic cylinder more than 10 times longer than for the DC motor which is not desirable. To try to decrease the pneumatic control sampling period a different approach will be employed in this thesis. The valve switching will be based on a specialized form

of model predictive control (MPC). With MPC, the variable to be controlled (in this thesis the slide position, y) is predicted one or more sampling periods into the future. This time span is termed the prediction horizon. The control signal which minimizes a cost-function is then sent to the valves. The cost-function typically consists of a weighted average of the squared tracking error and squared control signal. MPC was previously applied to the control of a pneumatic cylinder by Wang *et al.* (2000 and 2006) and to a pneumatic muscle actuator by Schindele and Aschemann (2008). Servo valves and continuous-valued MPC algorithms were used in this prior research. No prior applications of MPC to pneumatic systems with solenoid valves were found in the literature.

5.2.2 Model Predictive Control Algorithm

The use of on/off solenoid valves is similar to the limiting case of constrained input known in the literature as "bang-bang" control. With bang-bang control, the control signal may have only two states, on and off. In 1988, Tsang and Clarke presented a version of MPC for the bang-bang control case. They used an exhaustive search to compute the control state that minimized the MPC cost-function over the prediction horizon. The algorithm in this thesis was inspired by their work.

The combination of the two on/off valves gives the control signal, u_p, four possible discrete states as listed in Table 5.1. Because it only involves discrete u_p states it will be termed the discrete-valued MPC (DMPC) algorithm. The system model

developed in Chapter 4 will be used to predict the future slide position for each of these four states. The cost-function to be minimized is defined as

$$\begin{aligned} J &= \sum_{j=1}^{N_p} \left(y_d(i+j) - \hat{y}(i+j) \right)^2 \\ &= \sum_{j=1}^{N_p} \hat{e}(i+j)^2 \end{aligned} \tag{5.1}$$

where $y_d(k)$ is the desired position for the k^{th} sampling instant, $\hat{y}(k)$ is the predicted position, $\hat{e}(k)$ is the predicted tracking error, and N_p is the prediction horizon. The control signal for the current sampling instant is given by

$$\begin{aligned} u_p(i) &= \arg\min J \\ &= \arg\min \sum_{j=1}^{N_p} \hat{e}(i+j)^2 \\ &\text{subject to:} \\ \hat{y}(i+j) &= f\left(y(i), P_a(i), P_b(i), u_p(i) \right) \quad \text{for } j = \{1, 2, \ldots, N_p\} \\ u_p(i) &\in \{0, 1, 2, 3\} \end{aligned} \tag{5.2}$$

Because there are only four possible solutions, and the calculation of $\hat{y}(k)$ can be done rapidly, the optimization problem (5.2) is solved in real-time by exhaustive search. The closed-loop performance may be tuned by adjusting the prediction horizon, N_p. Note that the calculation of $\hat{y}(k)$ assumes that u_p remains constant over the prediction horizon.

Table 5-1 Definition of control signal discrete states.

Valve A state	Valve B state	Control signal discrete state, u_p
0	0	0
1	0	1
0	1	2
1	1	3

The algorithm used to compute $\hat{y}(i+j)$ in (5.2) is as follows:

5. Set j=1.
6. If j=1 then use:

$$\begin{aligned}\hat{P}_a(i+j-1) &= P_a(i)\\ \hat{P}_b(i+j-1) &= P_b(i)\\ \hat{y}(i+j-1) &= y_f(i)\\ \hat{\dot{y}}(i+j-1) &= \frac{y_f(i)-y_f(i-1)}{T_s}\end{aligned} \tag{5.3}$$

where $\hat{P}_a$ and $\hat{P}_b$ are the predicted pressures for chambers A and B, respectively; P_a and P_b are the measured pressures for chambers A and B, respectively; $\hat{y}$ is the predicted position, $\hat{\dot{y}}$ is the predicted velocity; y_f is the Butterworth low-pass filtered measured position (see section 3.5 for details); and Ts is the sampling period. Note that $T_s = 0.001\,\text{s}$ is used in this thesis.

7. If j>1 then use:

$$\begin{aligned}
\hat{P}_a(i+j-1) &= \hat{P}_a(i+j-2) + T_s\hat{\dot{P}}_a(i+j-2) \\
\hat{P}_b(i+j-1) &= \hat{P}_b(i+j-2) + T_s\hat{\dot{P}}_b(i+j-2) \\
\hat{y}(i+j-1) &= \hat{y}(i+j-2) + T_s\hat{\dot{y}}(i+j-2) \\
\hat{\dot{y}}(i+j-1) &= \hat{\dot{y}}(i+j-2) + T_s\hat{\ddot{y}}(i+j-2)
\end{aligned} \tag{5.4}$$

8. If $j = N_P + 1$ then go to step 14.

9. Compute the predicted mass flow rates using:

$$\hat{\dot{m}}_a(i+j-1) = \begin{cases} \lambda_{dis}\left(\hat{P}_a(i+j-1)\right) & \text{if } u_p(i+j-1-n_{d,dis}) \in \{0,2\} \\ \lambda_{fill}\left(\hat{P}_a(i+j-1)\right) & \text{if } u_p(i+j-1-n_{d,fill}) \in \{1,3\} \end{cases} \tag{5.5}$$

$$\hat{\dot{m}}_b(i+j-1) = \begin{cases} \lambda_{dis}\left(\hat{P}_b(i+j-1)\right) & \text{if } u_p(i+j-1-n_{d,dis}) \in \{0,1\} \\ \lambda_{fill}\left(\hat{P}_b(i+j-1)\right) & \text{if } u_p(i+j-1-n_{d,fill}) \in \{2,3\} \end{cases} \tag{5.6}$$

$$\lambda_{dis}(P) = \begin{cases} -\dot{m}_{choked} & \text{if } P > \dfrac{P_0}{0.53} \\ c_{dis}\left(P_0 - P\right) & \text{otherwise} \end{cases} \quad \text{and} \tag{5.7}$$

$$\lambda_{fill}(P) = \begin{cases} \dot{m}_{choked} & \text{if } P_s > \dfrac{P}{0.53} \\ c_{fill}\sqrt{P_s - P} & \text{otherwise} \end{cases} \tag{5.8}$$

where $\dot{m}_{choked}$ is the choked mass flow rate; $n_{d,fill}$ is the valve energizing delay in sampling periods; and $n_{d,dis}$ is the valve de-energizing delay in sampling periods. For the valves used in this thesis: $\dot{m}_{choked}$ =0.0061 kg/s, $n_{d,fill}$ = 4 and $n_{d,dis}$ = 1 (as was discussed in section 4.5).

10. Substitute $\hat{\dot{m}}_a(i+j-1)$ and $\hat{P}_a(i+j-1)$ into (4.18) to obtain $\hat{\dot{P}}_a(i+j-1)$.

11. Substitute $\hat{\dot{m}}_b(i+j-1)$ and $\hat{P}_b(i+j-1)$ into (4.18) to obtain $\hat{\dot{P}}_b(i+j-1)$.

12. Substitute $\hat{P}_a(i+j-1)$ and $\hat{P}_b(i+j-1)$ into (4.3) to obtain the predicted cylinder force, $\hat{F}_{cylinder}(i+j-1)$.

13. Compute the predicted gravity force, $\hat{F}_{gravity}(i+j-1)$, using (4.1) and $\hat{y}(i+j-1)$.

14. Compute the predicted friction force, $\hat{F}_{friction}(i+j-1)$, using (4.14), $\hat{y}(i+j-1)$, and $\hat{\dot{y}}(i+j-1)$.

15. Compute the predicted total force, $\hat{F}_{total}(i+j-1)$, using (4.1), $\hat{F}_{cylinder}(i+j-1)$, $\hat{F}_{gravity}(i+j-1)$ and $\hat{F}_{friction}(i+j-1)$.

16. Compute the predicted acceleration, $\hat{\ddot{y}}(i+j-1)$, using (4.2) and $\hat{F}_{total}(i+j-1)$.

17. Set j=j+1 and return to step 3.

18. Stop.

It is also very important to note that using a pneumatic control sampling period of 1ms is impractical since the delays of solenoid valves would prevent the commanded valve states from actually occurring. The minimum period must be greater than the maximum valve delay of 4ms. Therefore the pneumatic control sampling period was

selected to be T_{sp}=5ms. Since T_s=1ms, this was implemented in the control software by applying a $5T_s$ long zero-order hold to u_p.

5.2.3 Choice of the Prediction Horizon

The value of N_p was tuned based on the results obtained from a series of step input experiments. The motion was in the vertical plane with $m_{payload}$=0. In these experiments a 60 mm step input was used for y_d, starting from the static equilibrium position of y in the vertical plane. If necessary, this position may be found by setting equation (4.8) equal to zero and solving for y. The results are shown for N_p values ranging from 40 to 220 in Figure 5-1 and Figure 5-2. Note that values outside of this range produced inferior results. The maximum overshoot and maximum absolute steady-state errors from these plots are listed in Table 5-2. The rise times are not listed since they did not vary significantly. Overshoot is an indicator of the relative stability, and of the tracking errors that will occur with rapidly changing y_d trajectories. Steady-state error is an indicator of the errors that will occur with constant or slowly varying y_d trajectories. It is desirable for a closed-loop system to have a small overshoot and a small steady-state error. From Figure 5-1and Figure 5-2 and Table 5-2, it is apparent that the overshoot tends to decrease as N_p increases, and the steady-state error improves initially, but then worsens as N_p increases. Since it provided the best combination of small overshoot with small steady-state error, N_p=100 was selected, and will be used for the remainder of the thesis.

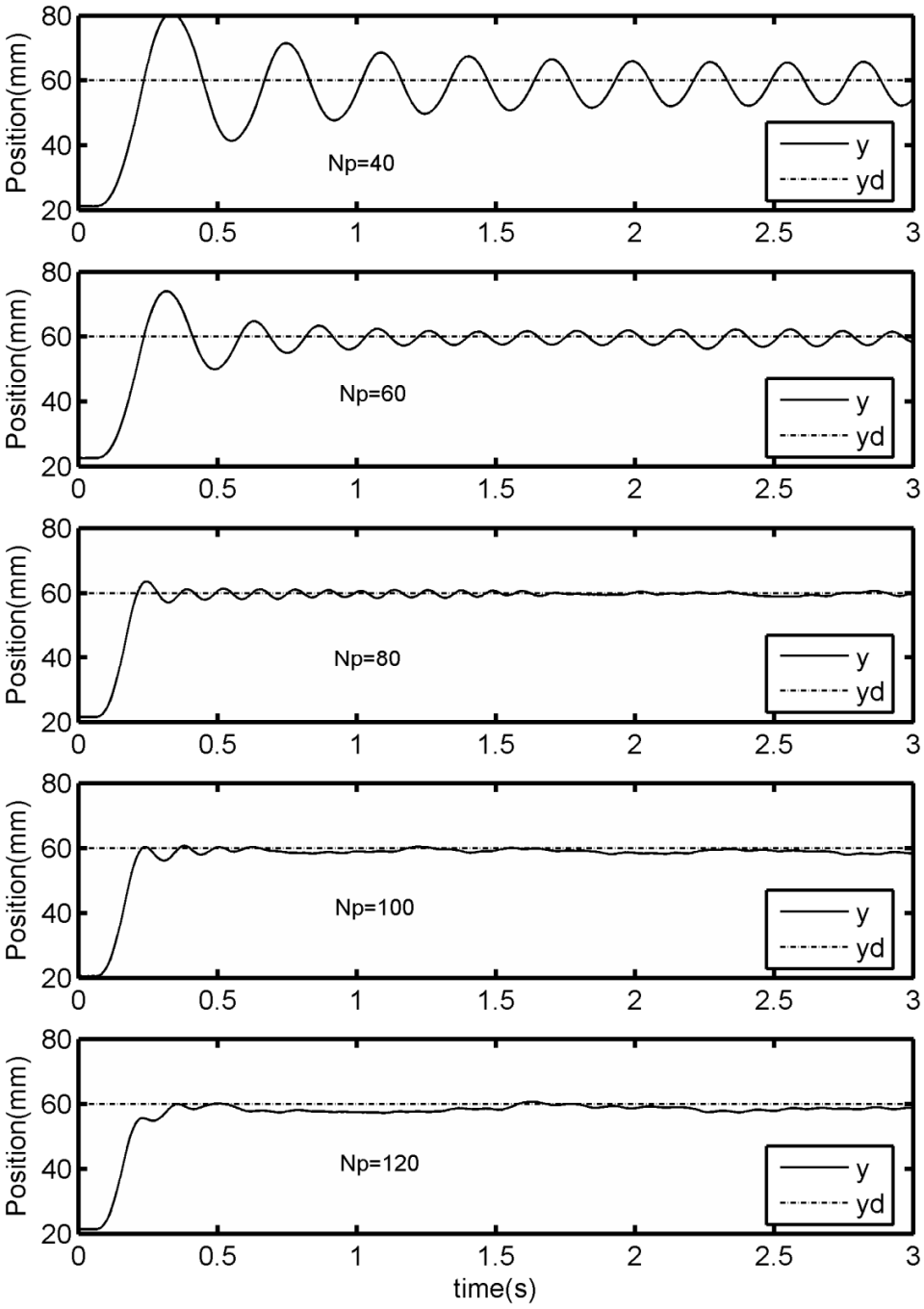

Figure 5-1 Experimental DMPC step-input results for N_p values from 40 to 120.

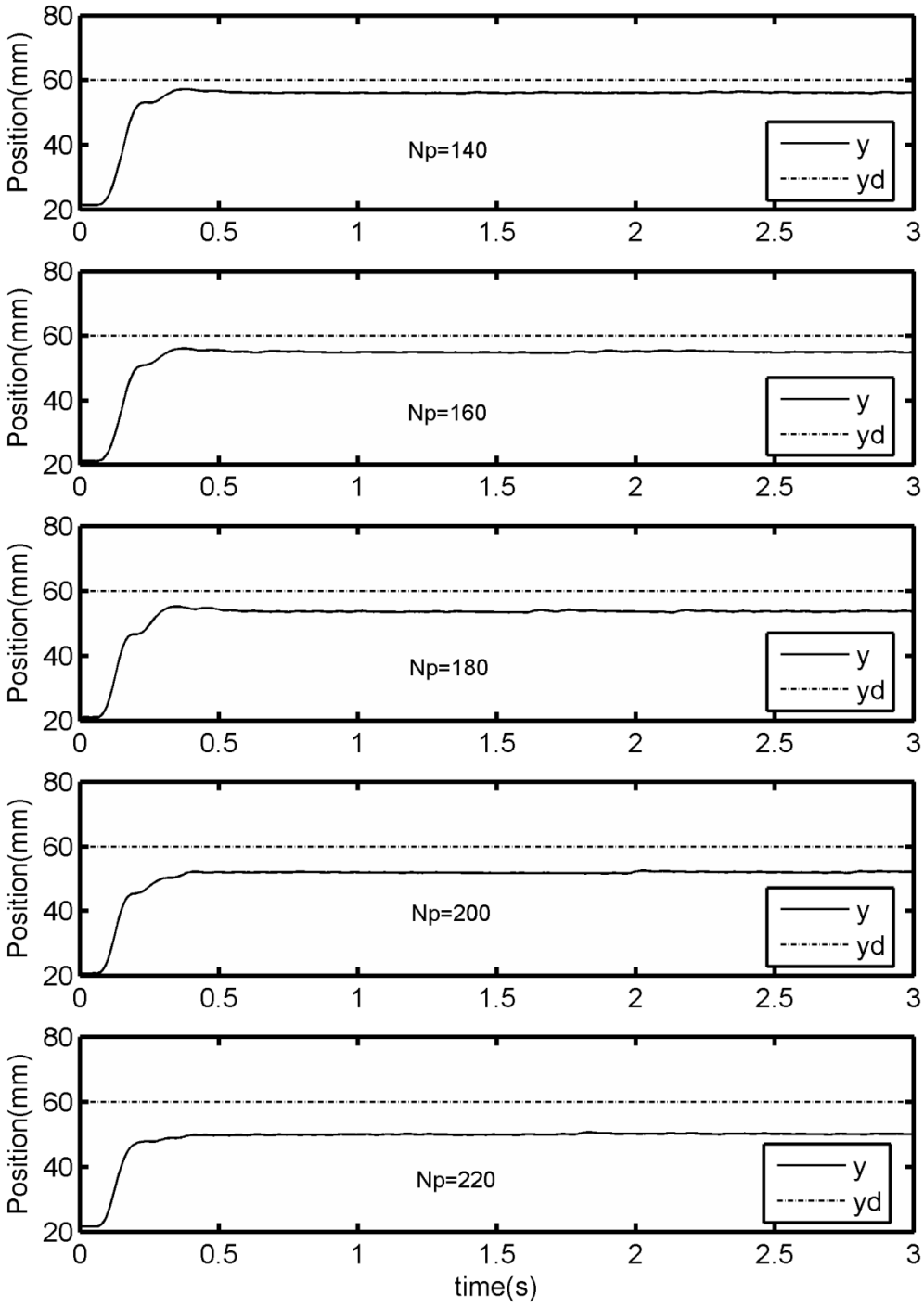

Figure 5-2 Experimental DMPC step-input results for N_p values from 140 to 220.

Table 5-2 Experimental DMPC step-input results for N_p values from 40 to 220.

N_p	40	60	80	100	120	140	160	180	200	220
Max. overshoot relative to steady-state (%)	35.05	23.53	5.92	1.15	1.14	0	0	0	0	0
Max. absolute steady-state error (mm)	1.19	0.46	0.43	0.89	2.06	3.78	5.05	6.33	8.17	9.95

5.3 Preliminary Experiments using DMPC with the Pneumatic Cylinder and a Payload Mass

Further experiments were performed with the same step input and equipment as the previous section. To test the robustness to a change in the payload mass, tests were done with $m_{payload}$ values of 0, 0.15 kg and 0.46 kg. Each test was repeated five times and the steady-state error results are listed in Table 5-3. Sample results are plotted in Figure 5-3 to 5-5. In these figures, $F_{model}=F_{gravity}$ with $y=y_d$ is plotted to show the force required to balance gravity.

Table 5-3 Steady-state error from step-input tests of the pneumatic cylinder with DMPC and various payloads.

	Max. absolute steady-state error (mm)				
	Test 1	**Test 2**	**Test 3**	**Test 4**	**Test 5**
$\mathbf{m_{payload} = 0.0\ kg}$	1.3	1.2	1.3	1.5	1.1
$\boldsymbol{m_{payload} = 0.15\ kg}$	3.4	3.2	3.6	3.4	2.7
$\boldsymbol{m_{payload} = 0.46\ kg}$	4.3	4.2	4.2	4.4	4.3

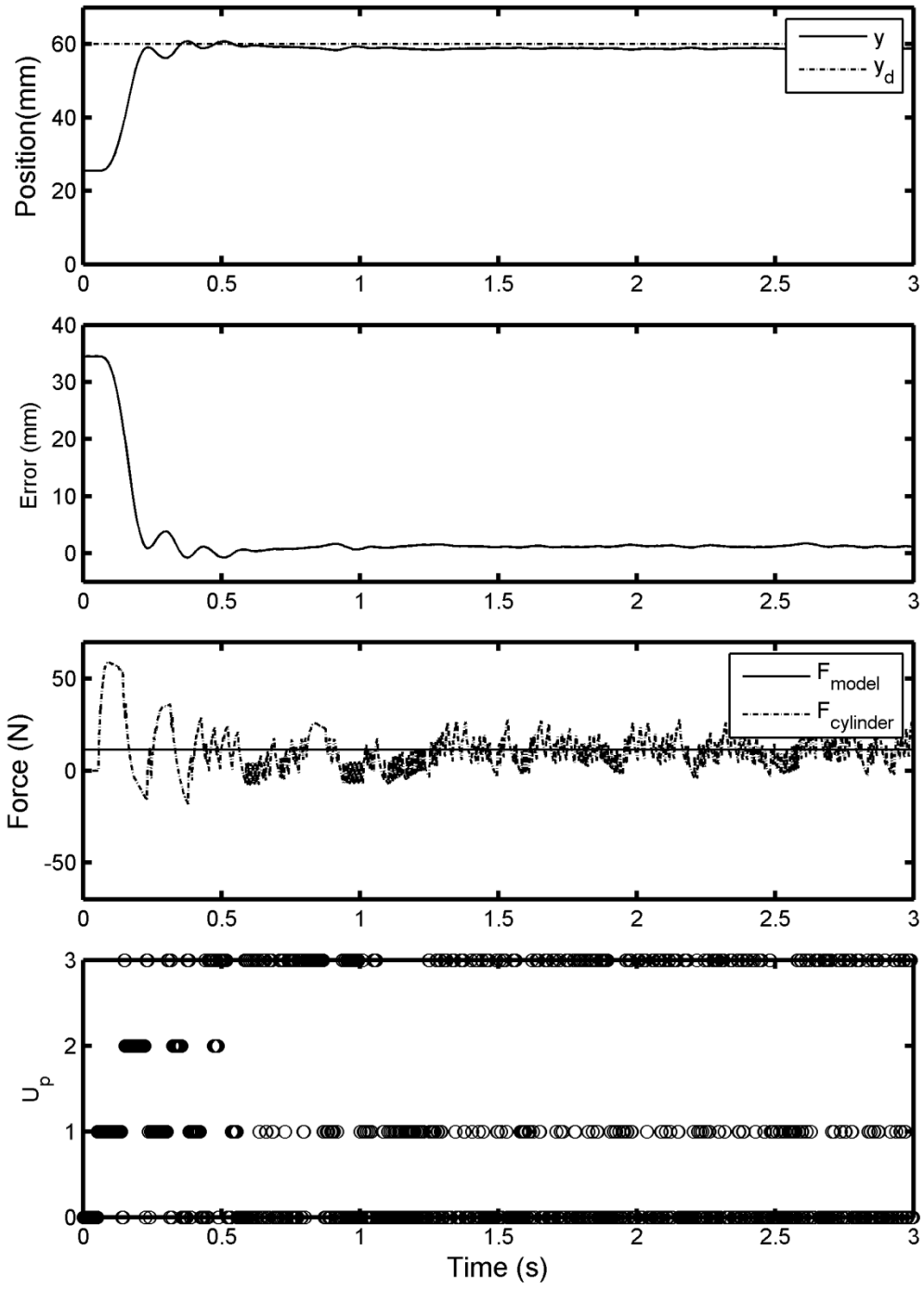

Figure 5-3 Step-input response of pneumatic cylinder with DMPC and $m_{payload}$=0.

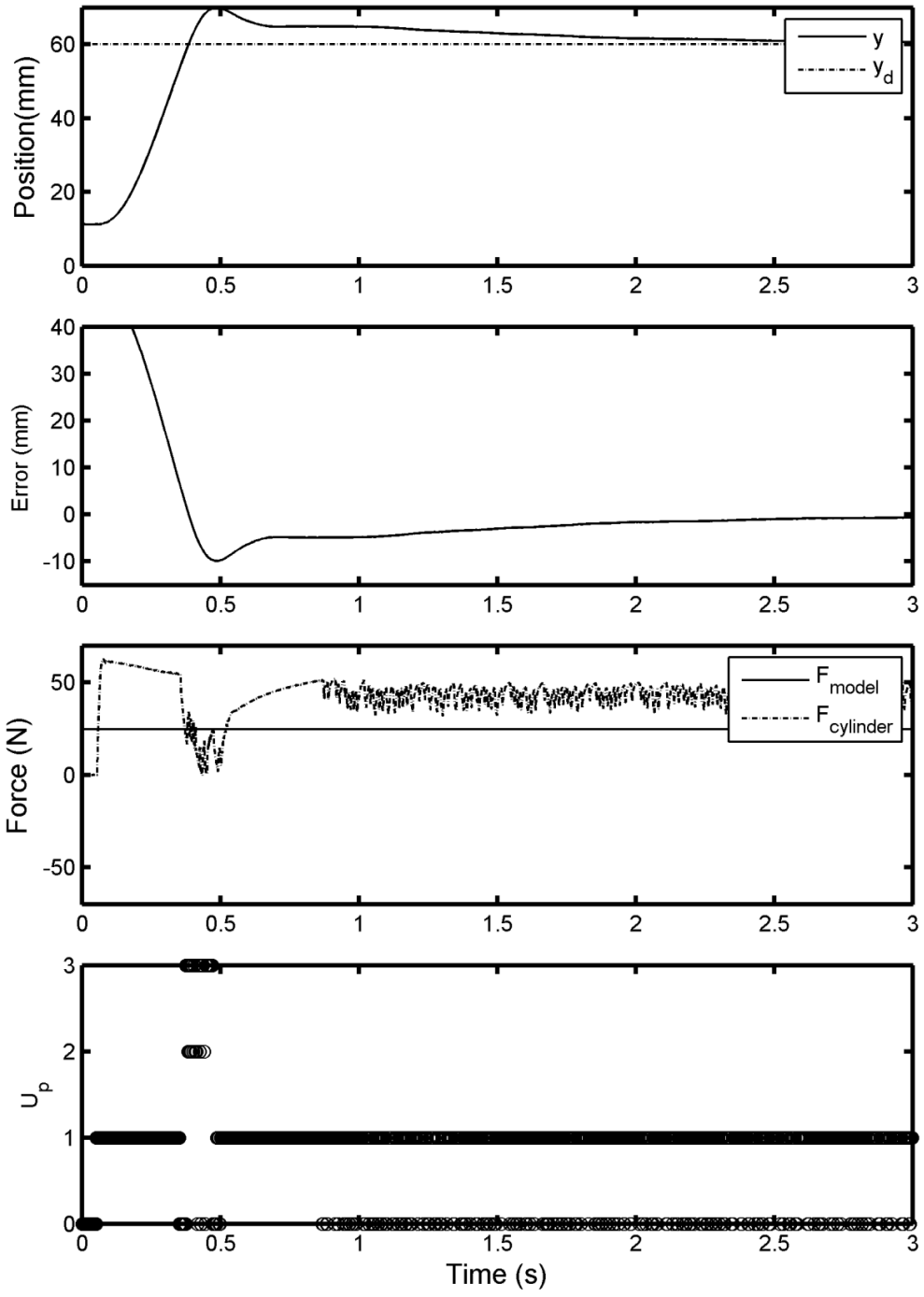

Figure 5-4 Step-input response of pneumatic cylinder with DMPC and $m_{payload} = 0.15$ kg.

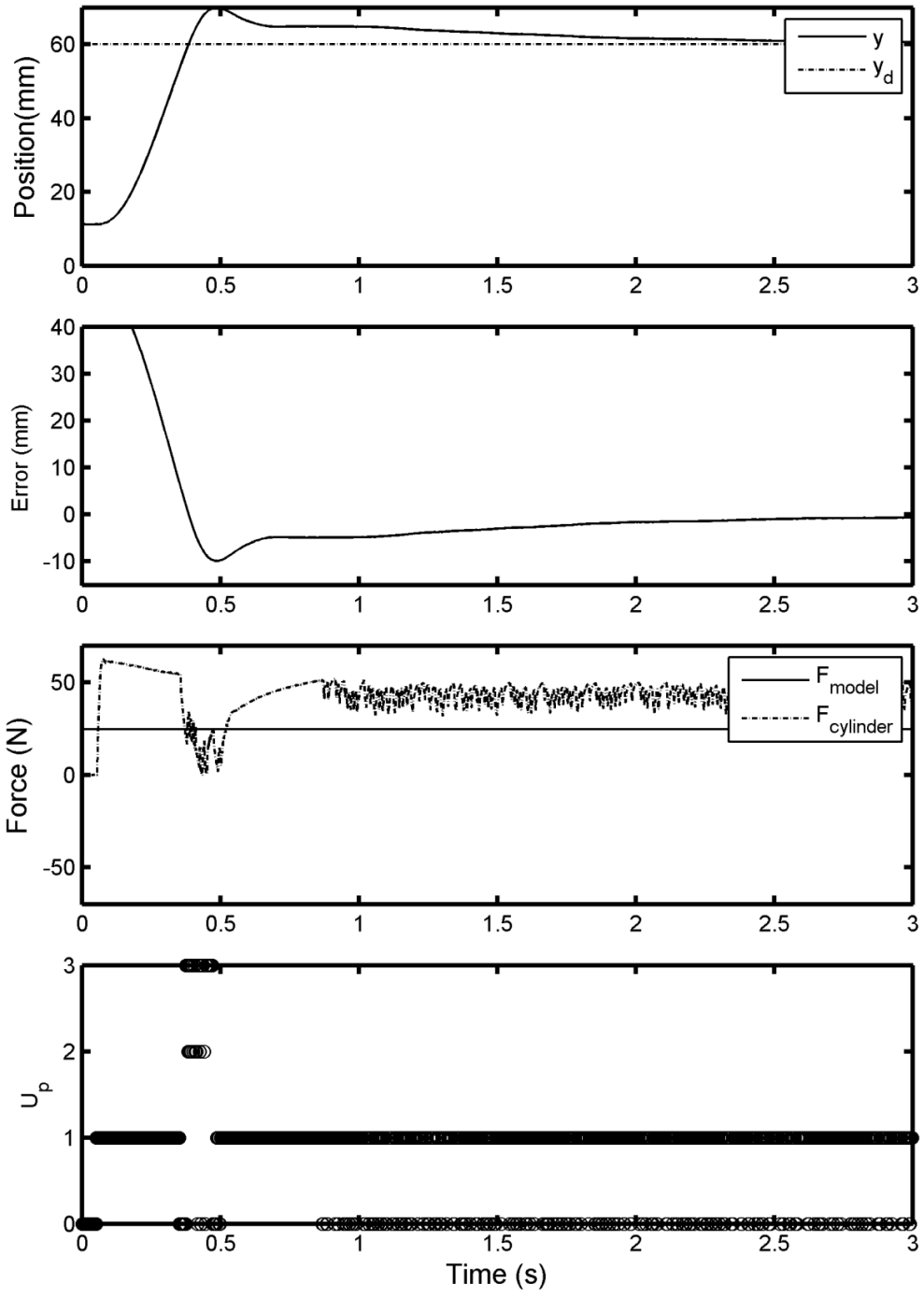

Figure 5-5 Step-input response of pneumatic cylinder with DMPC and $m_{payload} = 0.46$ kg.

From Table 5-3 and Figure 5-3 to 5-5, it can be observed that increasing the payload mass decreases the amplitude of oscillations after the initial transient which is desirable. However, it also greatly increases the steady-state error.

5.4 Compensation of the Steady-State Error

As shown in the previous section, the steady-state error of the pneumatic cylinder controlled using DMPC is sensitive to the payload mass. A standard method to reduce steady-state error is to introduce some form of integral action into the controller. With DMPC the most straightforward way to do this is to add an offset to y_d, as follows:

$$y_{offset}(i) = K_{ip} \sum_{n=0}^{i} \left(y_d(n) - y(n) \right) \tag{5.9}$$

$$y_{dp}(i) = y_d(i) + y_{offset}(i) \tag{5.10}$$

where i is the current sample number, y_{offset} is the offset used to compensate y_d, K_{ip} is the integral gain, and y_{dp} is desired position for the pneumatic DMPC controller. When y_{dp} is used in place of y_d the DMPC algorithm includes integral action and will be referred to as DMPC+I. A large value of K_{ip} will eliminate the steady-state error relatively quickly but will also tend to produce oscillations, possibly leading to instability. A small value of K_{ip} will not greatly affect relative stability, but will take longer to reduce the steady-state error. K_{ip} = 0.005 was found by manual tuning based on experimental step-input responses. To test the robustness of DMPC+I to a change in the payload mass, tests were done with $m_{payload}$ values of 0, 0.15 kg and 0.46 kg. Each test

was repeated five times and the steady-state error results are listed in Table 5-4. Sample results are plotted in Figures 5-6 to 5-8.

Table 5-4 Steady-state error from step-input tests of the pneumatic cylinder with DMPC+I and various payloads.

	Max. absolute steady-state error (mm)				
	Test 1	**Test 2**	**Test 3**	**Test 4**	**Test 5**
$\mathbf{m_{payload} = 0.0\ kg}$	0.2	0.2	0.2	0.2	0.2
$\boldsymbol{m_{payload} = 0.15\ kg}$	0.3	0.4	0.4	0.6	0.3
$\boldsymbol{m_{payload} = 0.46\ kg}$	0.5	0.7	0.6	0.6	0.7

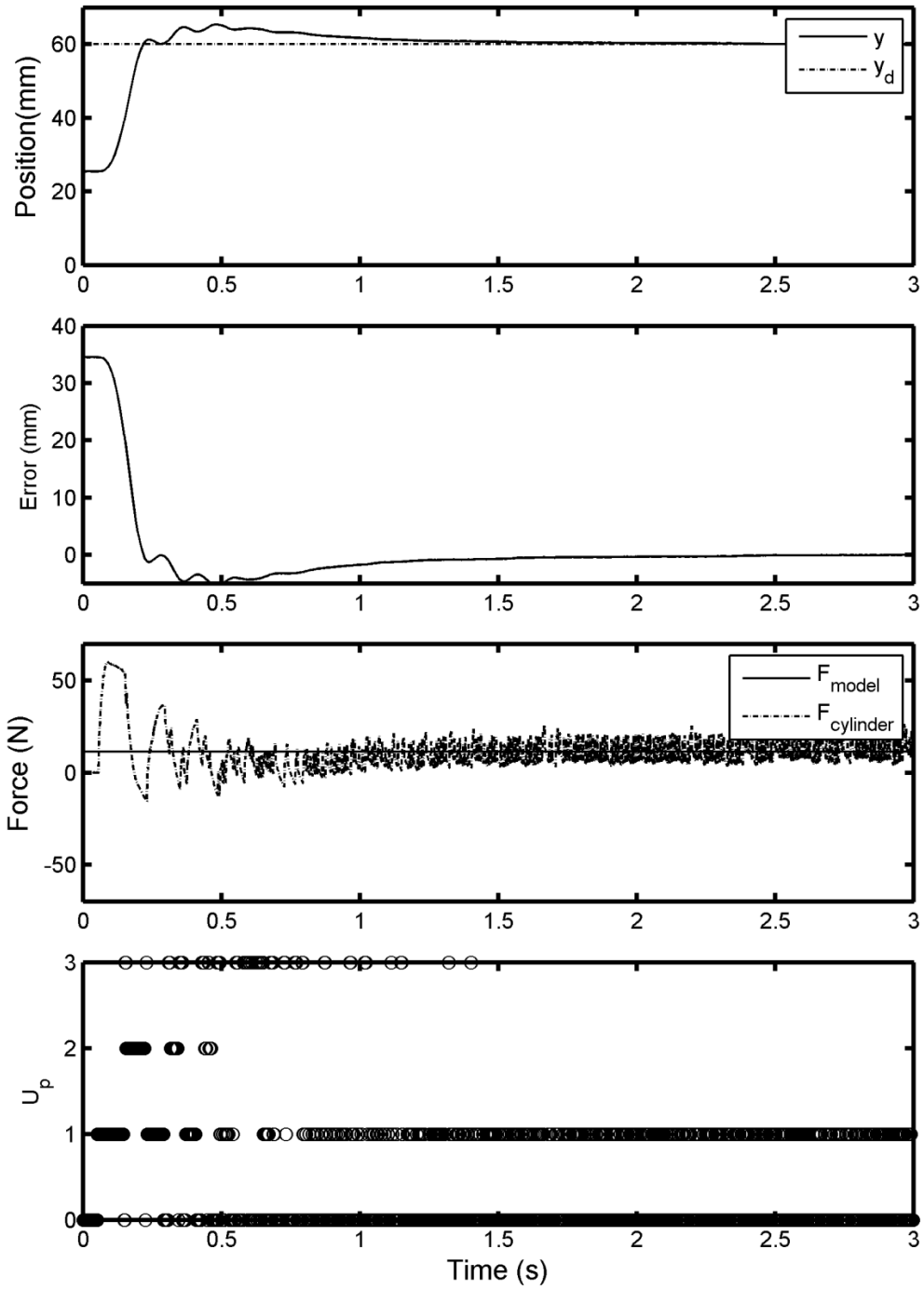

Figure 5-6 Step-input response of pneumatic cylinder with DMPC+I and $m_{payload} = 0.0$ kg.

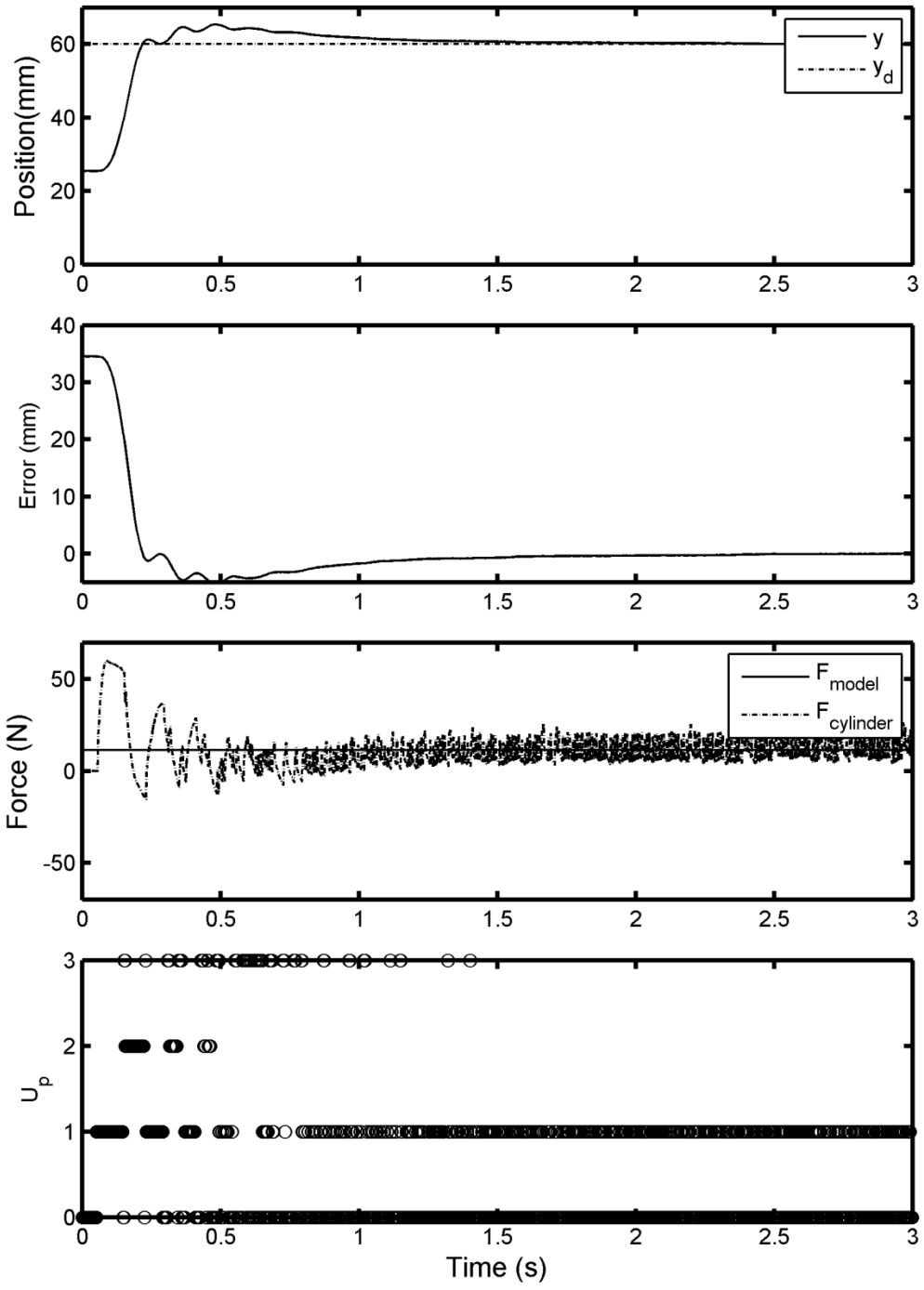

Figure 5-7 Step-input response of pneumatic cylinder with DMPC+I and $m_{payload} = 0.15$ kg.

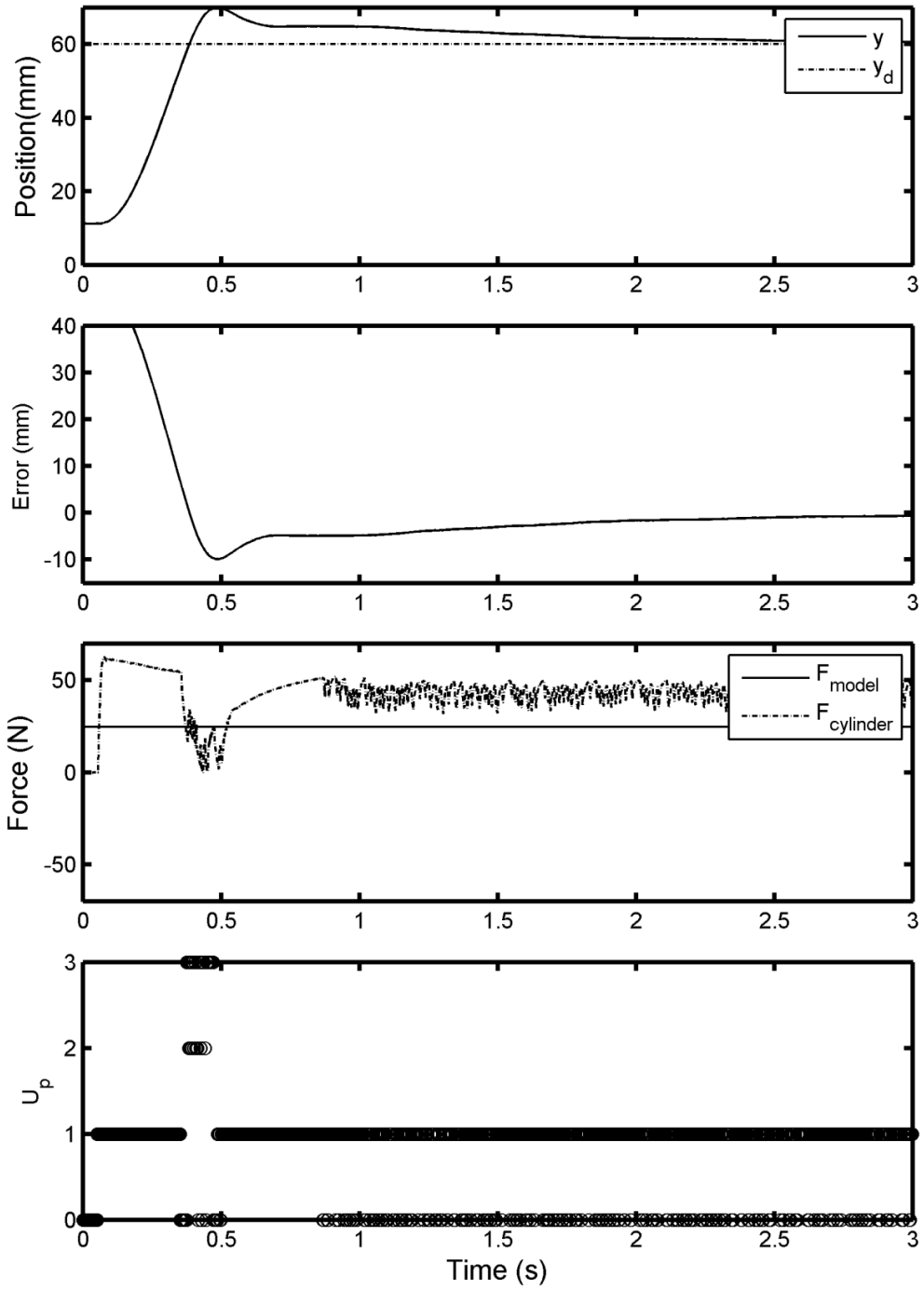

Figure 5-8 Step-input response of pneumatic cylinder with DMPC+I and $m_{payload} = 0.46$ kg.

From Table 5-4 and Figure 5-6 Step-input response of pneumatic cylinder with DMPC+I and $m_{payload} = 0.0$ kg. to 5-8, it can be observed that DMPC+I has greatly reduced the steady-state error, at the cost of increasing the overshoot and initial oscillations. It should be noted here that the pneumatic cylinder controlled by either DMPC or DMPC+I constitutes a switched nonlinear system. While methods for analyzing the stability of switched linear systems are available (Liberzon, 2003), the stability analysis of general switched nonlinear systems remains unsolved, and is beyond the scope of this thesis.

5.5 DC Motor Control

Two control algorithms will be investigated for controlling the DC motor. The first is inspired by the "inverse dynamics" control technique that has been successfully used with high performance robot arms (Spong and Vidyasagar (1989)). To apply the design method presented in section 8.3 of Spong and Vidyasagar (1989), it is first necessary to write the system dynamics from (4.1) and (4.2) in the form:

$$\ddot{y} = \frac{F_{motor} + F_{cylinder} + F_{gravity} - F_{friction}}{m_{eq}} \tag{5.11}$$

Then the method results in the inverse dynamics (ID) control law:

$$F_{motor}(i) = \hat{m}_{eq}\ddot{y}_d(i) + K_{pe}\left(y_d(i) - y_f(i)\right) + K_{de}\left(\dot{y}_d(i) - \hat{\dot{y}}(i)\right) - \hat{F}_{cylinder} - \hat{F}_{gravity} + \hat{F}_{friction} \tag{5.12}$$

where i is the sample number, the ^ symbol indicates the value estimated using the model parameters and the measured variables, K_{pe} is the proportional gain for the

motor (K_{pe}>0), K_{de} is the derivative gain for the motor (K_{de}>0), $\hat{\dot{y}}$ is the estimated velocity (computed using (5.3)), and y_f is the Butterworth low-pass filtered measured position (see section 3.5 for details). The control sampling period equals T_s. If the parameters and sensed values are perfect, and F_{motor} is unconstrained, then applying (5.12) to the system (5.11) will result in the closed-loop error dynamics:

$$\ddot{e} + \frac{K_{de}}{m_{eq}}\dot{e} + \frac{K_{pe}}{m_{eq}}e = 0 \qquad \textbf{(5.13)}$$

where $e = y_d - y$ is the error. Eq. 5.15 implies that the closed-loop will be stable with zero steady-state error. Of course, the assumptions of a perfect model, perfect sensors and unconstrained F_{motor} are unrealistic so the real performance may be considerably different than that predicted by (5.13). This issue will be further explored in the next chapter.

The second control algorithm is the standard proportional plus derivative (PD) controller given by:

$$F_{motor}(i) = K_{pe}\left(y_d(i) - y_f(i)\right) + K_{de}\left(\dot{y}_d - \hat{\dot{y}}\right) \qquad \textbf{(5.14)}$$

This algorithm was selected for two reasons. First it keeps the feedback elements of (5.14) but does not require a system model. Second, it is similar to algorithm used by Takemura *et al.* (2000) with their hybrid actuator. For both (5.13) and (5.14), a control sampling period of T_s=0.001 s will be used.

5.6 Summary

The design of a position control algorithm for the hybrid actuator was investigated. Using the model developed in Chapter 4, a model predictive control algorithm was designed for switching the solenoid valves to control the position of the pneumatic cylinder. Integral action was then added to improve the steady-state performance. Next, two control algorithms were proposed for the DC motor. The first is a model-based controller designed using the inverse dynamics method. The second is standard PD controller. The control algorithms will be evaluated using computer simulations in the next chapter.

CHAPTER 6

SIMULATIONS

6.1 Introduction

In this chapter, computer simulations will be used to evaluate the performance of the control algorithms proposed in the previous chapter. Simulations provide useful information without risking the hardware damage that can result from preliminary experiments. The simulations will be performed for two different vertical motion trajectories and three different payloads. With a real robot, the payload is not usually known in advance, or measured online. To be cautious, a payload of zero is assumed by the controller in all of the simulations. The simulations with non-zero payloads will test the robustness of each controller. Simulations will be presented and discussed for the pneumatic cylinder acting alone, and for the hybrid actuator.

6.2 Trajectory Selection

The actuator should perform well under both dynamic and steady-state conditions. A cycloidal y_d trajectory will be used to test the dynamic and steady-state performance. Its position, velocity and acceleration are calculated using (3.1)-(3.3), respectively. Note that since the position sensor only measures the linear position y, the desired trajectory was converted from radians to mm using (4.4). The trajectory begins at the static

equilibrium position of y in the vertical plane and ends at 100 mm. The position y=100 mm is close to the maximum stroke of the cylinder and corresponds to the angle $\theta = 2.67$ radians (see Figure 4-1 for an illustration of y and θ). The movement time is: T_e=4 s. The trajectory is preceded and followed by dwell periods of 2 s. The position, velocity and acceleration curves for this trajectory are shown in Figure 6-1.

A y_d trajectory similar to a sine wave will be used to test the performance under more dynamic conditions. The total duration is 8 s. A cycloidal curve is used in the first and last second to make the position and velocity curves continuous. The portion from 1 s to 7 s is a 1 Hz sine wave with an amplitude chosen such that max(y_d)=100 mm. The position, velocity and acceleration curves for this trajectory are shown in Figure 6-2.

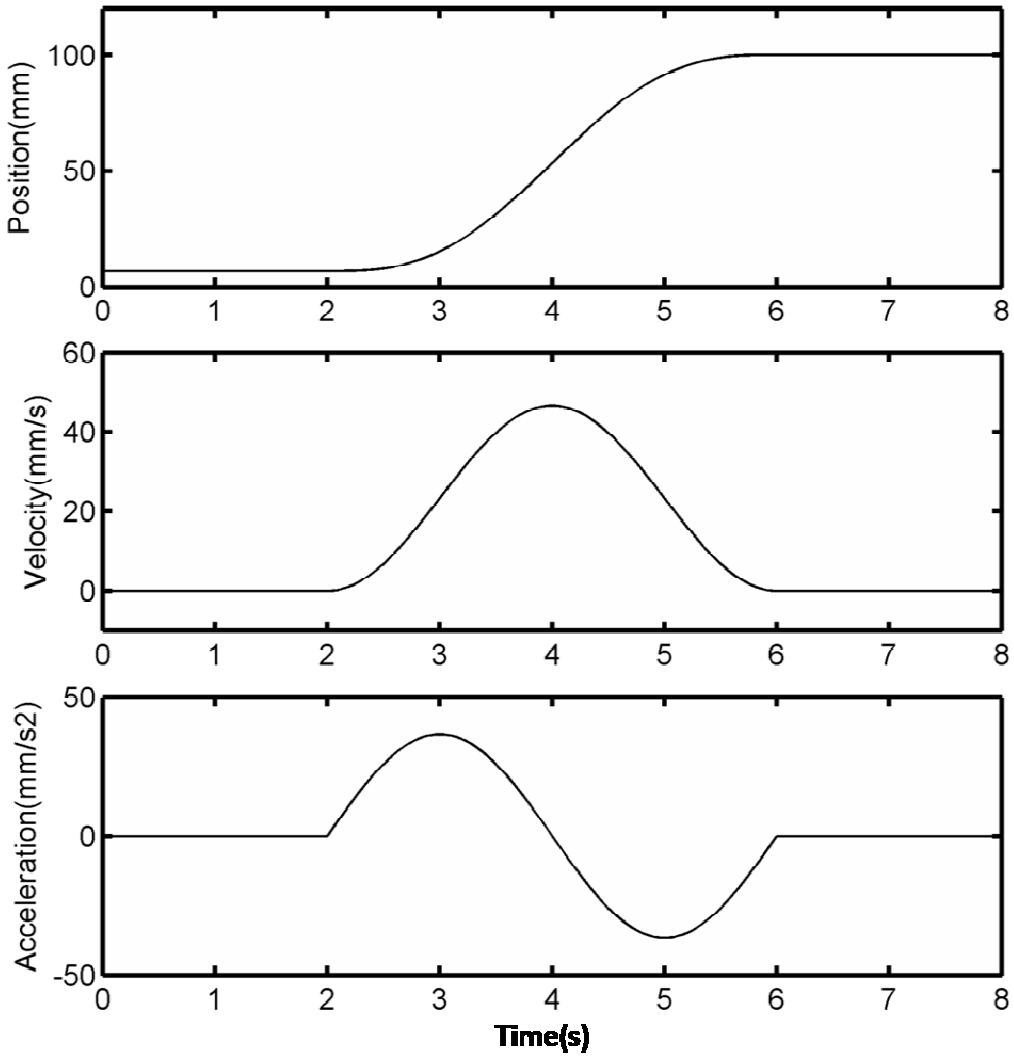

Figure 6-1 Cycloidal trajectory

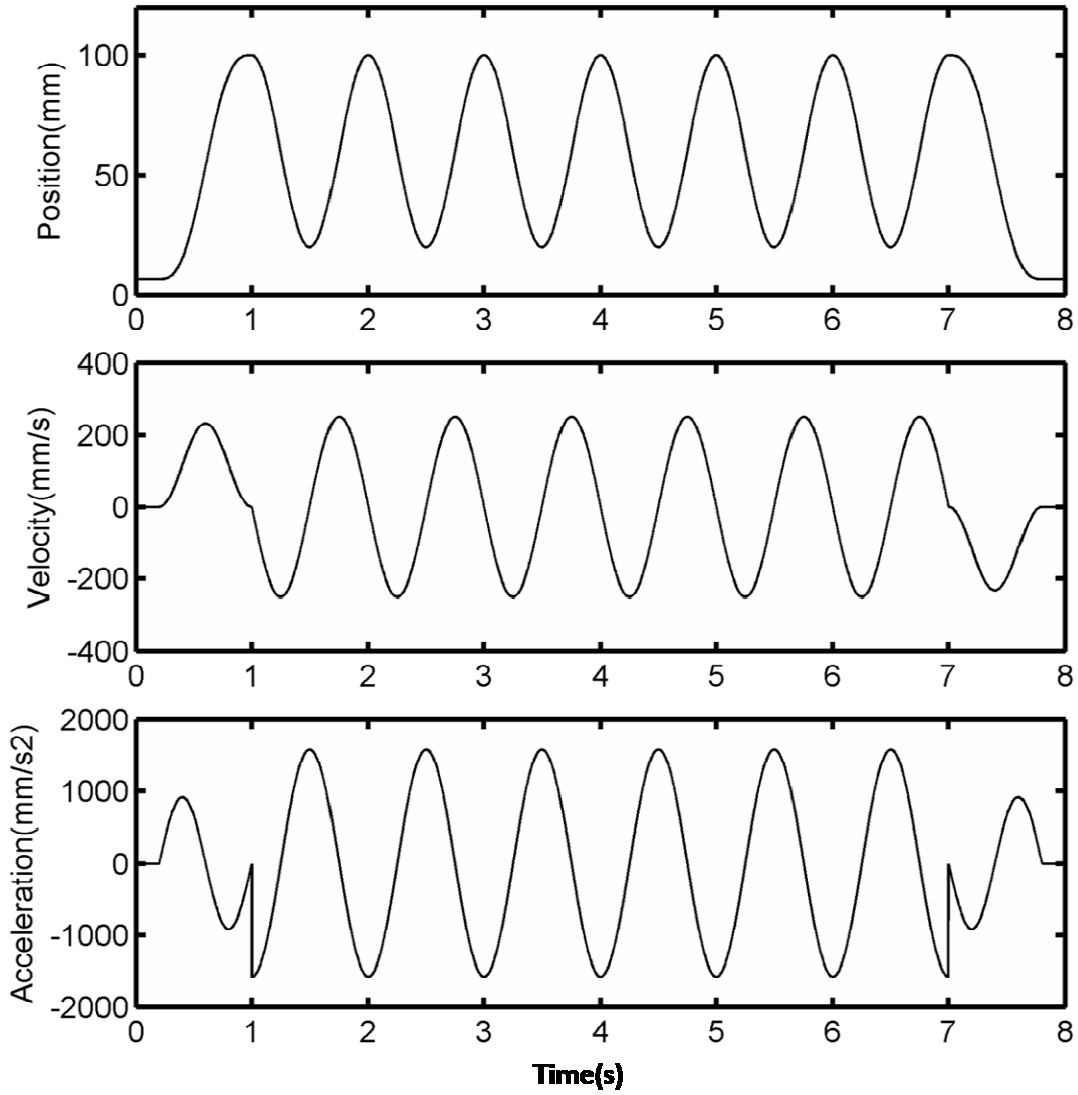

Figure 6-2 Sine wave trajectory

6.3 Performance Metrics

Performance metrics will be used to provide data for quantitative comparisons of the simulation results in this chapter and of the experimental results in Chapter 7. The root-mean-square error (RMSE) will provide a measure of the average tracking error over

both the entire motion trajectory. The maximum absolute error (MAE) provides a worst-case performance metric. For the cycloidal trajectory, the steady-state performance will be quantified using the steady-state error (SSE) and steady-state amplitude (SSA). The SSE equals the mean absolute value of the error when the response is at steady-state. Most control systems never stay at a perfectly constant position when y_d is constant. The SSA quantifies the level of steady-state vibration, and equals the difference between the maximum and minimum values of y in this region.

6.4 Simulation Settings

To allow comparisons between simulations and experiments to be presented in Chapter 7, the PD gains from section 7.2 will also be used in this chapter. Two non-zero payloads will be used to study the controller robustness, specifically: $m_{payload}$ = 0.15 kg and $m_{payload}$ = 0.46 kg. Because the payload is located at the end of the arm these values will substantially increase the equivalent mass and gravity force. Specifically, increasing $m_{payload}$ from 0 kg to 0.15 kg increases m_{eq} by 70% and $\max(|F_{gravity}|)$ by 150%. Increasing it from 0 kg to 0.46 kg increases m_{eq} by 230% and $\max(|F_{gravity}|)$ by 460%. All of the simulations were programmed in Matlab.

6.5 Simulation Results and Discussion

Figure 6-3 to 6-7 show the simulation results for the pneumatic cylinder acting alone. Figure 6-8 to 6-17 show the simulation results for the hybrid actuator and two

control algorithms described in chapter 5. Note that results for the sine wave trajectory and $m_{payload}$ = 0.46 kg are not presented since the position control failed due to the force saturation of both the DC motor and pneumatic cylinder.

Each figure includes five plots. These plots show the planned trajectory, y_d, and actual trajectory, y, the position error, the pneumatic valve command, u_p, (as defined in Table 5-1), the force from the pneumatic cylinder and the force from the electrical motor. In the simulations where the system was only driven by the cylinder, the electrical motor force always equalled zero.

Table 6-1 and 6-2 summarize the performance metrics of both trajectories.

6.5.1 Pneumatic Cylinder Alone

Figure 6-3 to 6-5 present the results for the cycloidal trajectory with different payloads. Figure 6-6 and 6-7 are the results for the sine wave trajectory with different payloads. These will be discussed separately below.

6.5.2 Cycloidal Trajectory

As discussed in section 6.2, the cycloidal trajectory can be separated into three parts. It starts to move at t=2 s. It reaches the target position = 100 mm at t = 6 s and follows this with a 2 s dwell period.

The first and second plot of each figure shows the trajectory following performance. At first glance, it looks like as the payload increased, the system performance worsened in terms of trajectory following. However, examining the results given in Table 6-1 provides greater detail. When payload was 0.15 kg, the system has the smallest SSE. When the payload was 0.46 kg, the system has the smallest SSA. Finally, when there was no payload, the system has the smallest MAE. So not all performance metrics worsened as the payload increased.

Returning to the plots, during the transient period, the amplitude of the error near the beginning (from t = 2 s to 4 s) got larger as the payload increased. The result with no payload shows a maximum error of about 1.2 mm, with a payload of 0.15 kg this increased to 2.5 mm, and it increased again to 3 mm with the 0.46 kg payload. Conversely, as the payload increased, the amplitude of error decreased during the steady state part of the trajectory. This is obvious from the plots during t= 6 s to 8 s, and from the SSA values given in Table 6-1. The error responses also followed a certain pattern, especially in Figure 6-4. This is an example of a limit cycle where the position and velocity do not decay to zero, but also does not exceed a certain bounded region of the state space. It is thought that the coarse quantization of the pneumatic system is the main cause of this phenomenon. When the arm moves in the vertical plane, the gravity force is always present. The pneumatic valve command, up, has only four states. It is hard for the system to find a single optimized valve state to generate just the right amount of force to overcome the gravity, so it must switch between several good, but not optimal, choices.

Also, when payload is smaller, changes on the pressure of each chamber will cause a larger position change than with the larger payload.

6.5.2.1 Sine wave trajectory

Figure 6-6 and 6-7 are the simulation results for the sine wave trajectory and payloads of 0 kg and 0.15 kg. The sine wave trajectory is a better test of the dynamic response than the cycloidal trajectory. The acceleration and velocity are larger (recall Figures 6-1 and 6-2), and the gravity force also changes more rapidly. As expected, a more accurate system model provides a better result. Recall that the controller assumes the payload is zero. The result with zero payload has much smaller values of MAE and RMSE, as listed in Table 6-2. This clear distinction did not happen with the cycloidal trajectory, meaning that an accurate system model is more important in this more dynamic situation. Looking further into the error plot, it may be noticed that frequency of the error oscillations is lower at the higher payload. This shows the same pattern as the cycloidal trajectory tests.

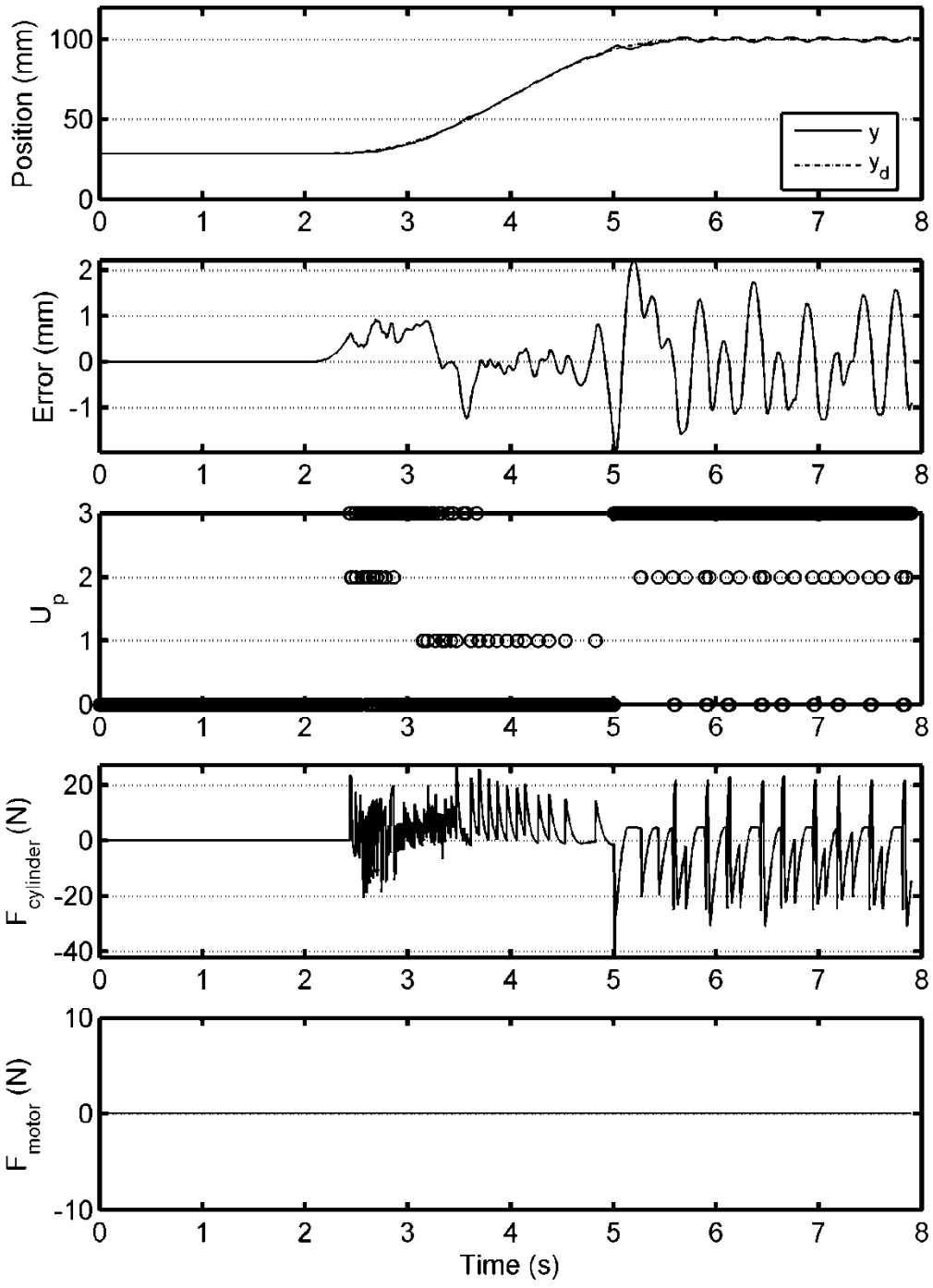

Figure 6-3 Vertical cycloidal trajectory simulation with the pneumatic cylinder, DMPC+I controller, and mpayload = 0 kg.

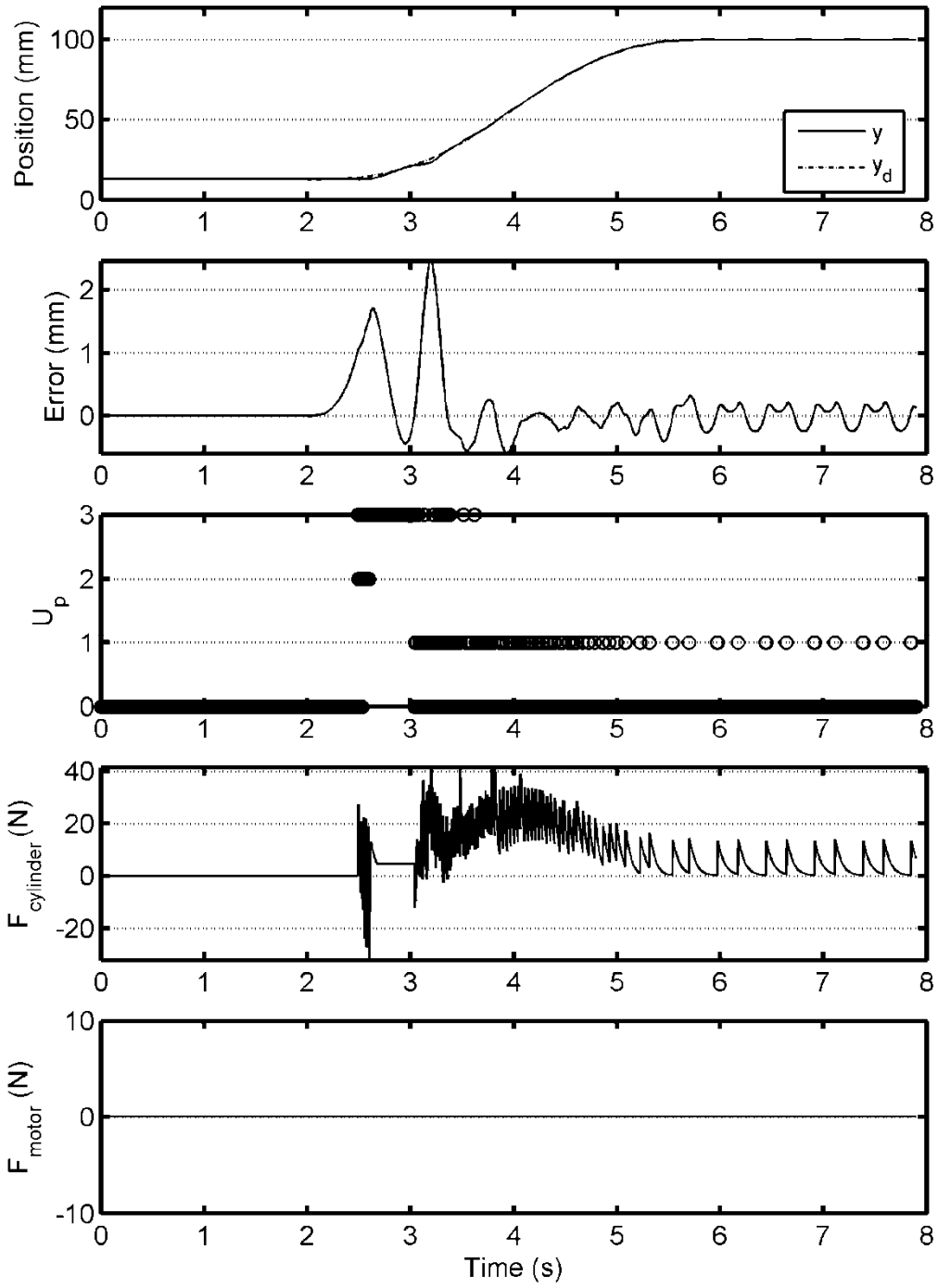

Figure 6-4 Vertical cycloidal trajectory simulation with the pneumatic cylinder, DMPC+I controller, and $m_{payload}$ = 0.15 kg.

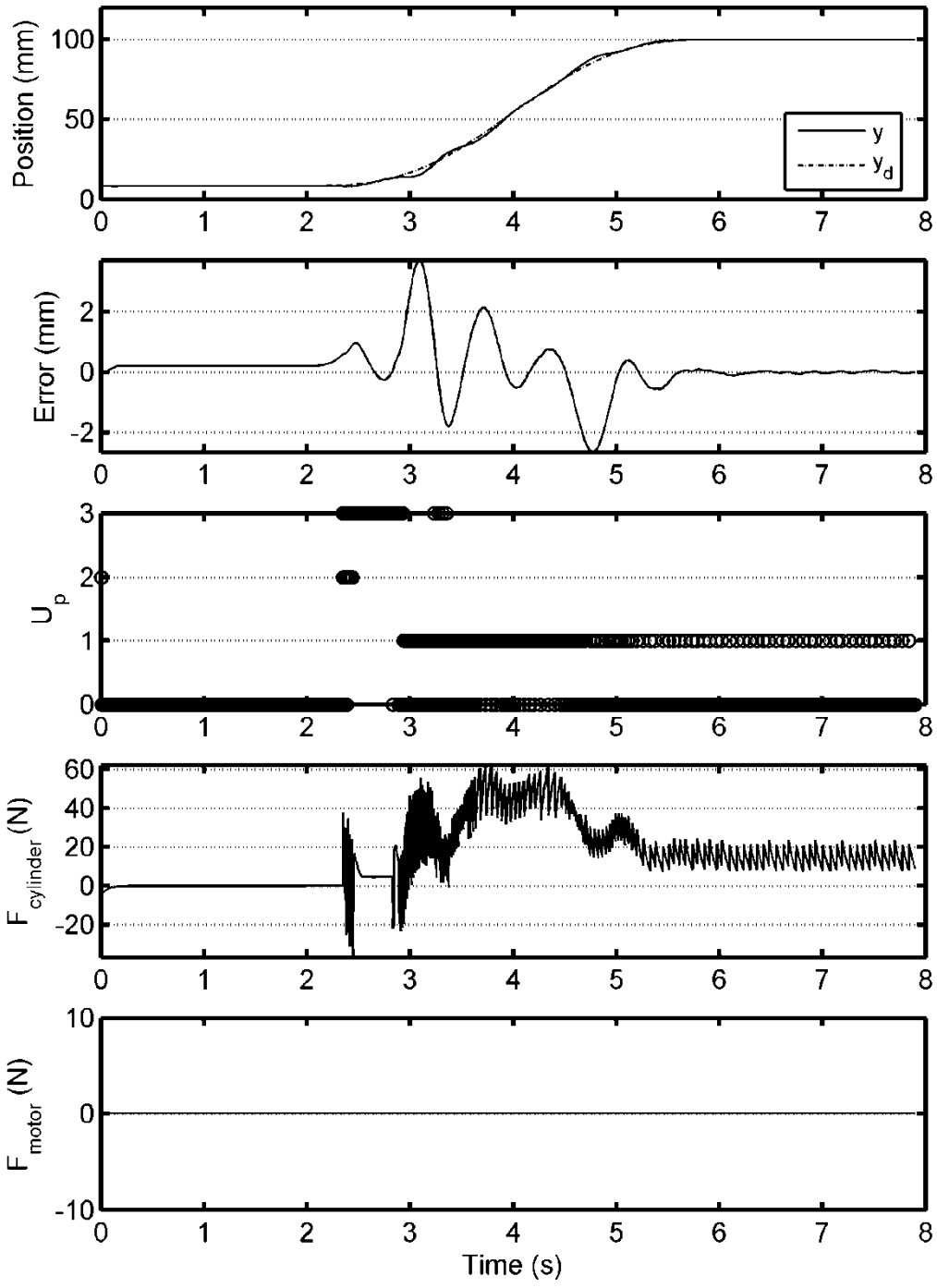

Figure 6-5 Vertical cycloidal trajectory simulation with the pneumatic cylinder, DMPC+I controller, and $m_{payload}$ = 0.46 kg.

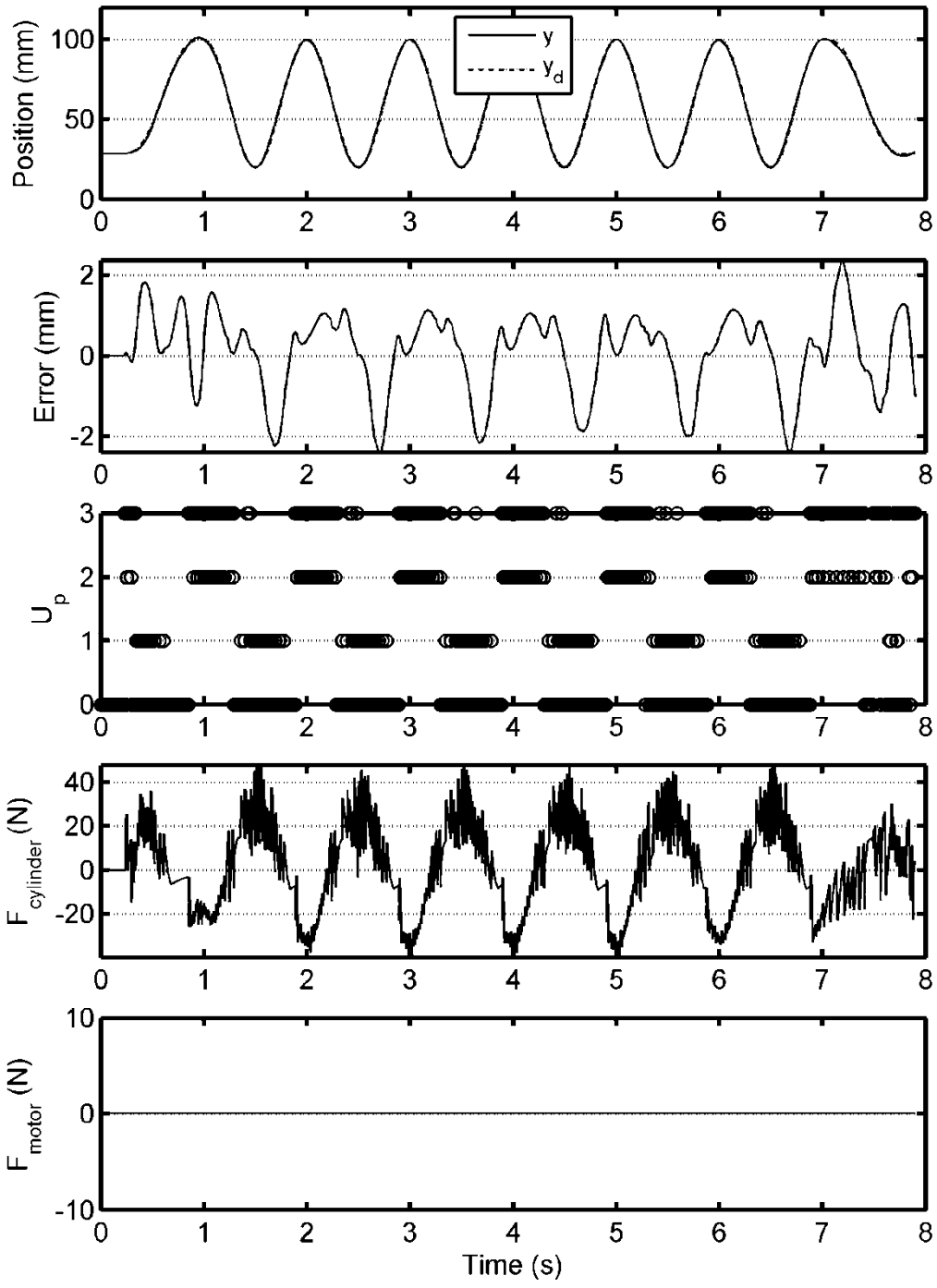

Figure 6-6 Vertical sine wave trajectory simulation with the pneumatic cylinder, DMPC+I controller, and $m_{payload}$ = 0 kg.

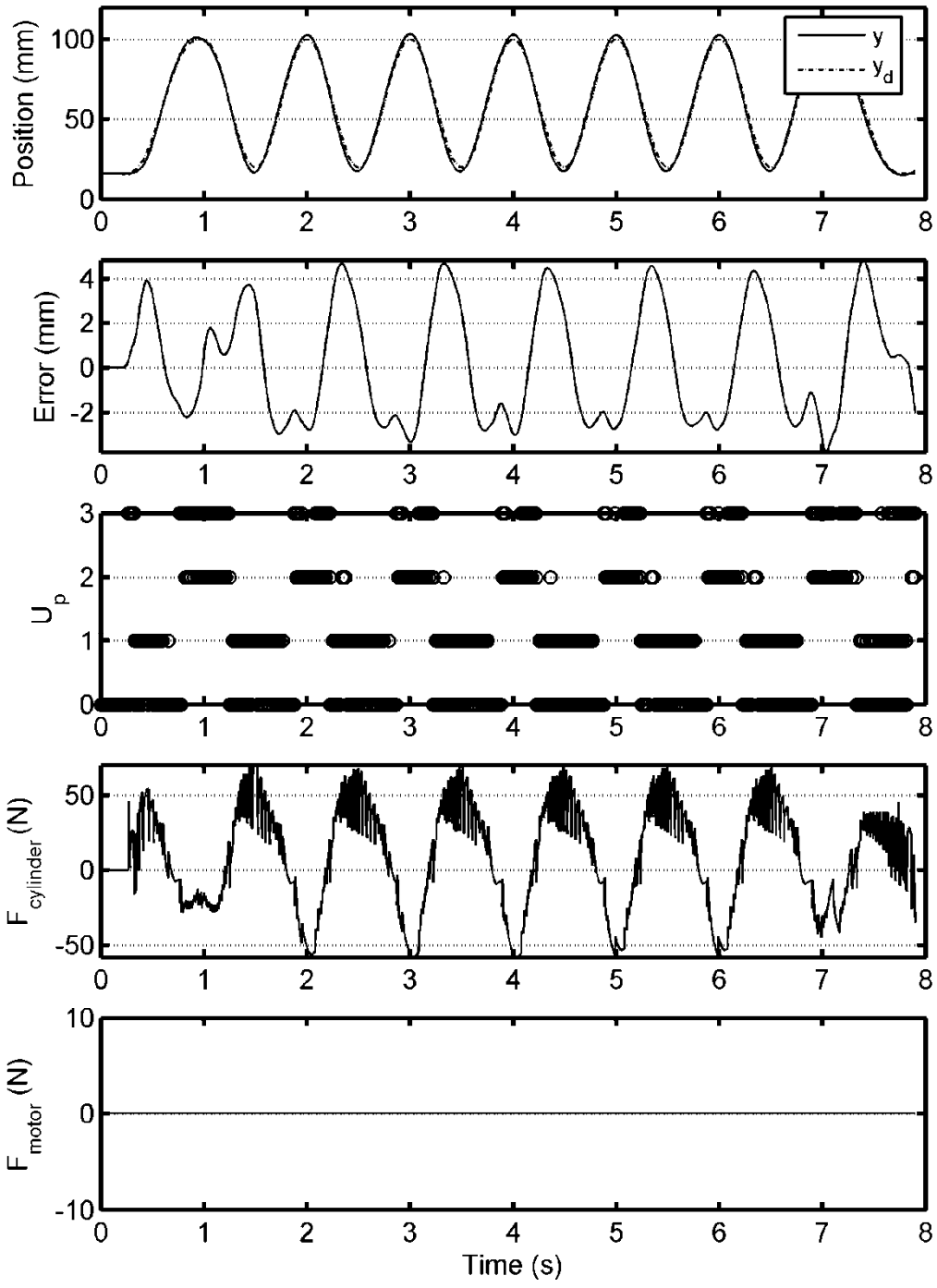

Figure 6-7 Vertical sine wave trajectory simulation with the pneumatic cylinder, DMPC+I controller, and $m_{payload}$ = 0.15 kg.

6.5.3 Hybrid Actuator

Figure 6-8 to 6-17 show the simulation results for the hybrid actuator and both cycloidal and sine wave trajectories. The DMPC+I controller is used to control the pneumatic cylinder. For the DC motor, both the ID and PD motor control algorithms from section 5.5 are simulated.

From these simulation results, the hybrid actuator has a much better overall performance than the pneumatic cylinder. The ID motor controller worked better than the PD controller in the cycloidal trajectory tests, while the PD controller performed better than ID controller with the sine wave trajectory. The results will be discussed in further detail below.

6.5.3.1 Cycloidal Trajectory

Figure 6-8, 6-10 and 6-12 show the simulation results for the cycloidal trajectory and the ID motor controller. As shown by (5.11), the ID controller uses the information from the measured pneumatic pressures to calculate the required electrical motor force. In theory, this would produce very small tracking errors. However, in reality the motor has a torque limit that limits its force output. If the force required from the motor is more than it can generate, the motor cannot compensate for the error. In Figure 6-8, the maximum error occurred at around $t \approx 3$ s. This corresponds to the time when the maximum positive acceleration was required (see Figure 6-1). Although the pneumatic cylinder is capable of providing the necessary force, the prediction algorithm chose the valve state which

minimized the predicted error, but also happened to produce a smaller force than the ideal. Even with additional force generated by the electrical motor, the hybrid actuator still did not produce enough force to closely follow the trajectory. The same situation happened at $t \approx 5$ s in Figures 6-10 and 6-12, where the maximum negative force was required. This undershoot is smaller than the overshoot at $t \approx 5$ s since the gravity force helps to stop the arm when it is moving upwards. The undershoot is less obvious in Figure 6-8 because the quantized valve state happened to produce a pneumatic force closer to the ideal.

Figure 6-9, 6-11 and 6-13 show the results for the cycloidal trajectory and the PD motor controller. As shown by (5.14), the PD controller does not take cylinder force into consideration. It considers only the error and rate of change of the error and adjusts the DC motor output accordingly. This simpler approach produced slightly different results compared with the ID controller. In all of the cycloidal trajectory simulations, the performance of the PD controller was not as good as the ID controller. Since the PD controller did not take the pneumatic force into account, it tended to be more aggressive since it was trying to correct the error by itself. This caused larger position oscillations. This can be observed from position and error plots. Also the motor force plot indicates it reached the saturation situation more frequently than with ID controller. However, as the payload increased the performance differences between the ID and PD motor controllers decreased, as seen from the plots and the metrics in Table 6-1. There are two reasons for this. First, the larger payload requires larger force from the actuator so

saturation occurs more often and makes the performances more similar. Second, since the controller assumes the payload is zero, when the payload increases the model inaccuracy increases and this worsens the performance of the ID controller.

With all of these results the finer quantization and faster speed of response of the DC motor compared to the pneumatic cylinder is very apparent. For example, in Figure 6-8, the desired position starts changing at t = 2 s, but due to its coarse quantization u_p does not change until $t \approx 3$ s. Meanwhile, the motor force begins to smoothly change at t = 2 s. This earlier force increase started the motion of the system and prevented the error from accumulating. This ability to "fill in the gaps" of the pneumatic actuator led to the performance improvement shown by the hybrid actuator in this section, and elsewhere in the thesis.

6.5.3.2 Sine wave trajectory

Figure 6-14 and 6-16 are the results for sine wave trajectory with the hybrid actuator and ID motor controller. There is an obvious improvement compared with the results for the pneumatic cylinder shown in Figure 6-6 and 6-7. As with those results, the maximum overshoots and undershoots tended to occur close to the times where the desired acceleration was maximum (see Figure 6-2). These acceleration demands also caused the DC motor force to saturate which limited its ability to reduce the error.

From Figures 6-15 and 6-17, and Table 6-2, it can be observed that the PD motor controller produce smaller errors than the ID motor controller with this trajectory. This

was true even though the DC motor force saturated even more frequently than with the ID controller.

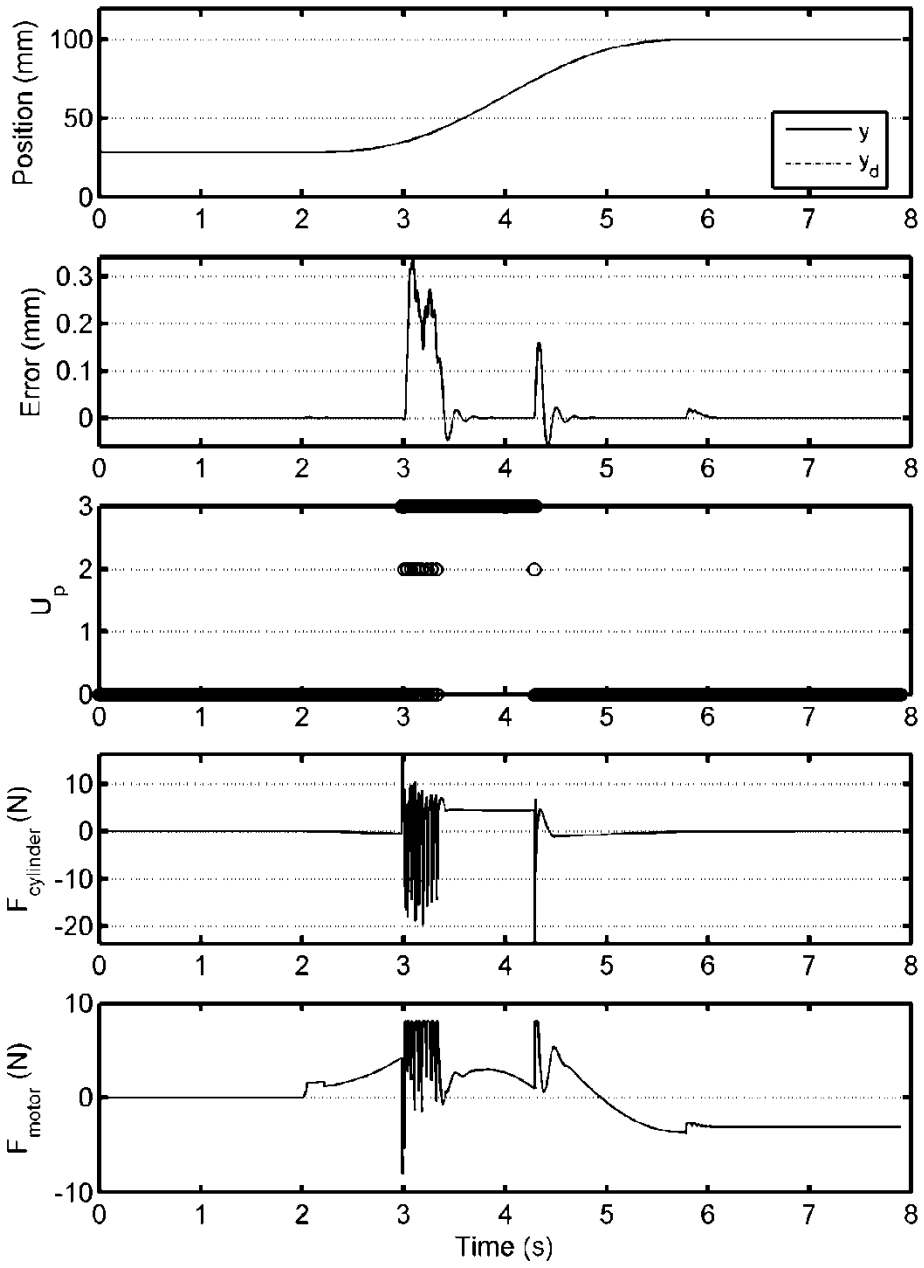

Figure 6-8 Vertical cycloidal trajectory simulation with the hybrid actuator, DMPC+I cylinder controller and ID motor controller, and $m_{payload}$ = 0 kg.

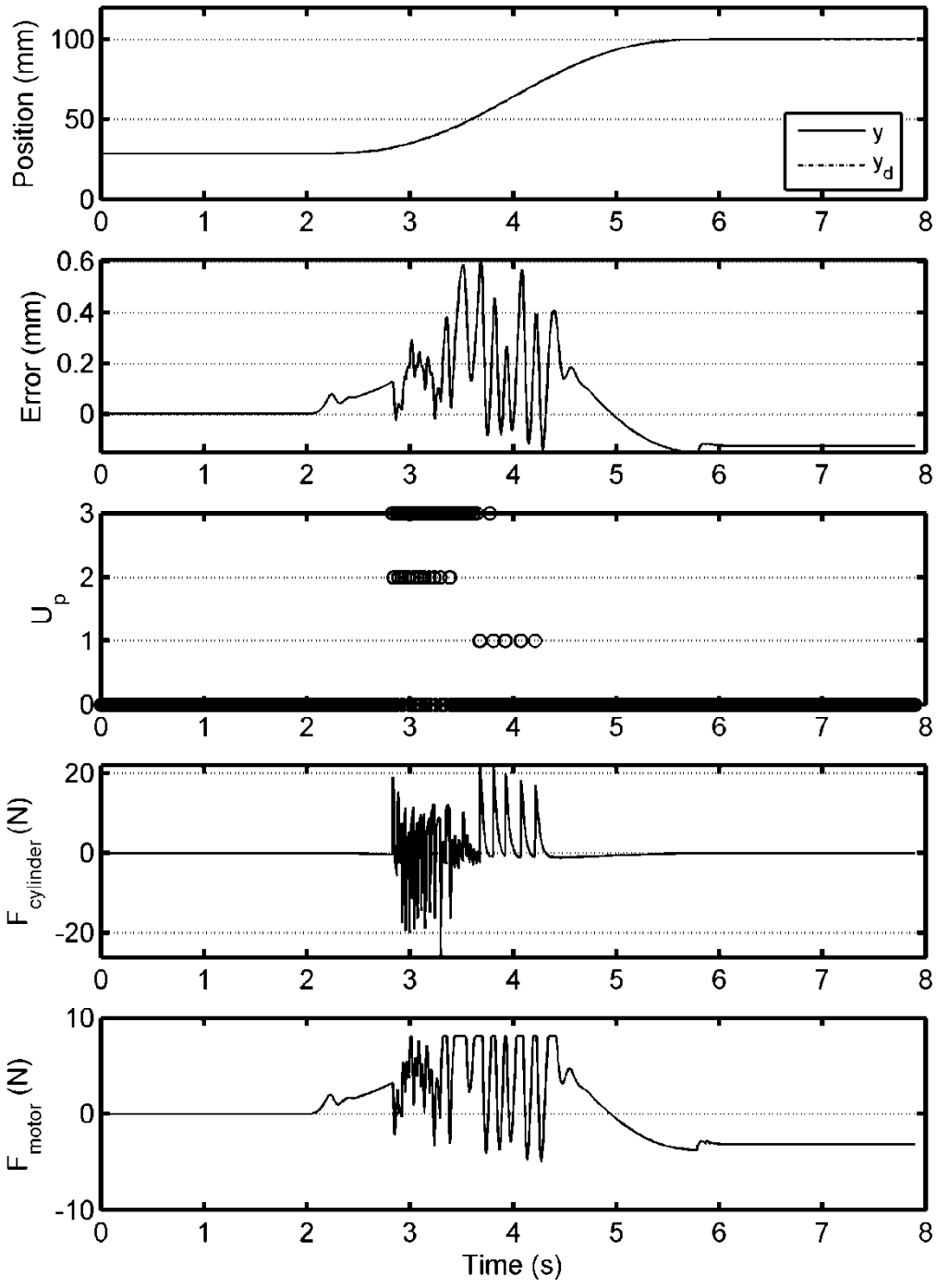

Figure 6-9 Vertical cycloidal trajectory simulation with the hybrid actuator, DMPC+I cylinder controller and PD motor controller, and $m_{payload}$ = 0 kg.

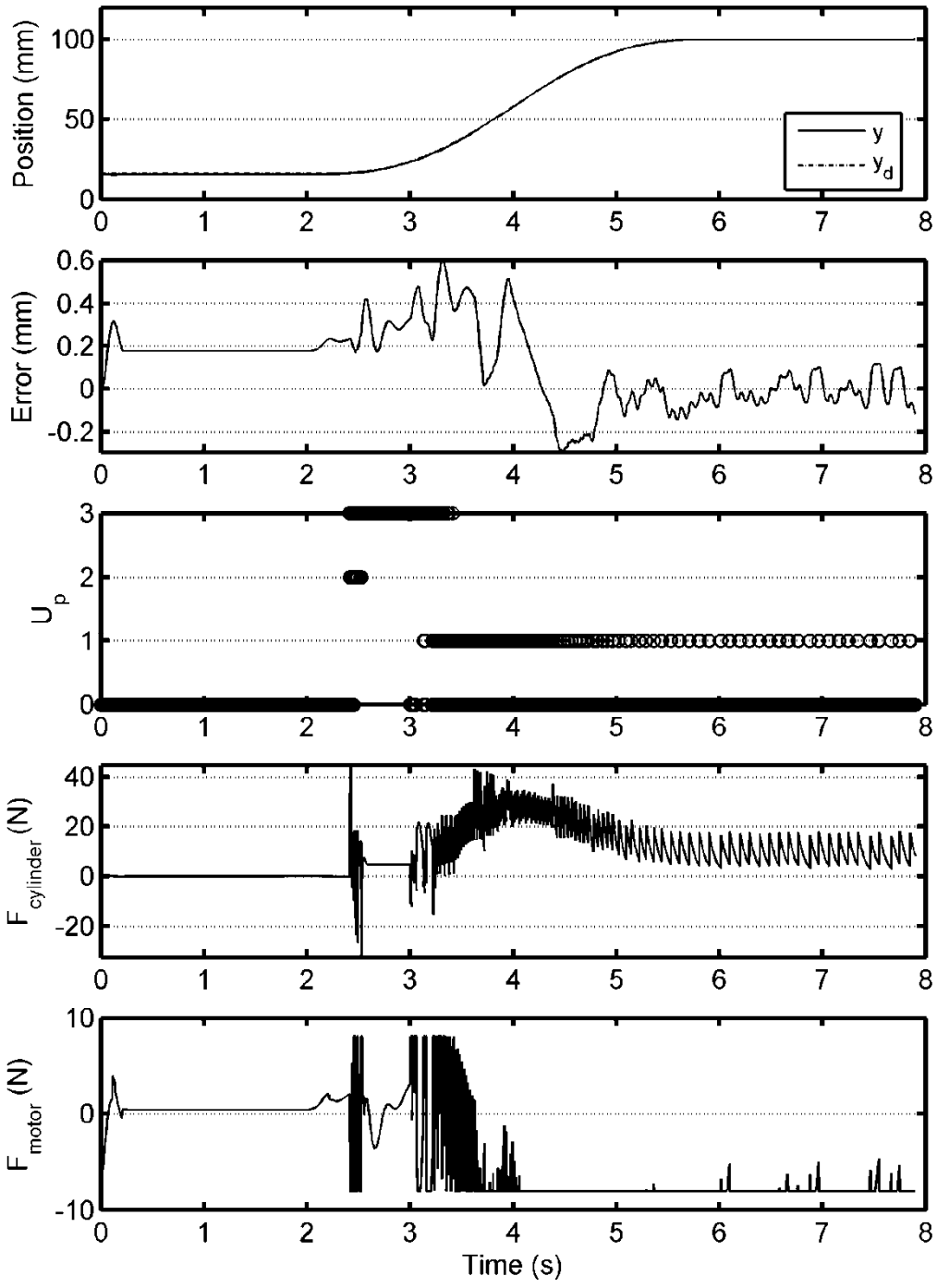

Figure 6-10 Vertical cycloidal trajectory simulation with the hybrid actuator, DMPC+I cylinder controller and ID motor controller, and $m_{payload}$ = 0.15 kg.

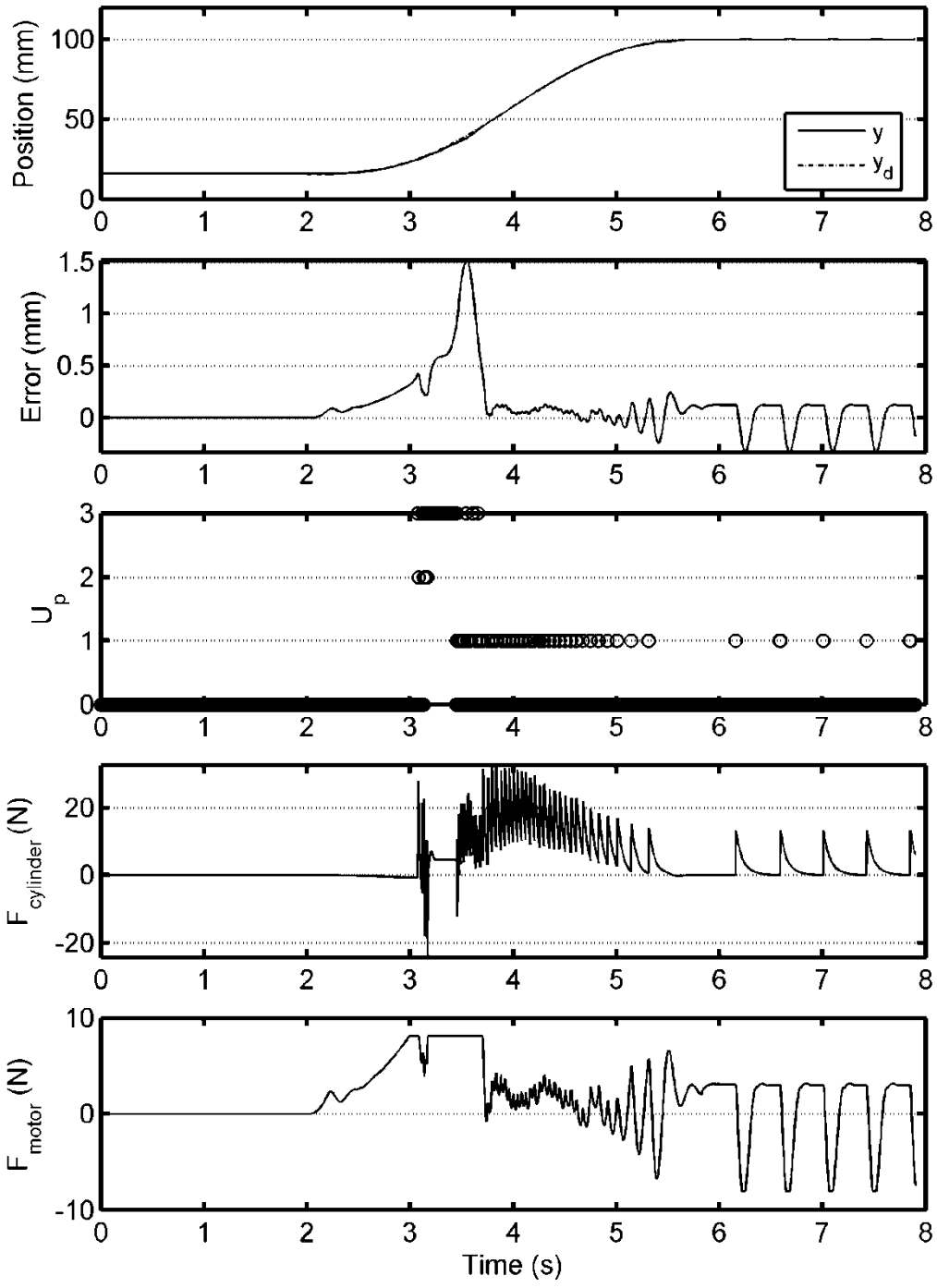

Figure 6-11 Vertical cycloidal trajectory simulation with the hybrid actuator, DMPC+I cylinder controller and PD motor controller, and $m_{payload}$ = 0.15 kg.

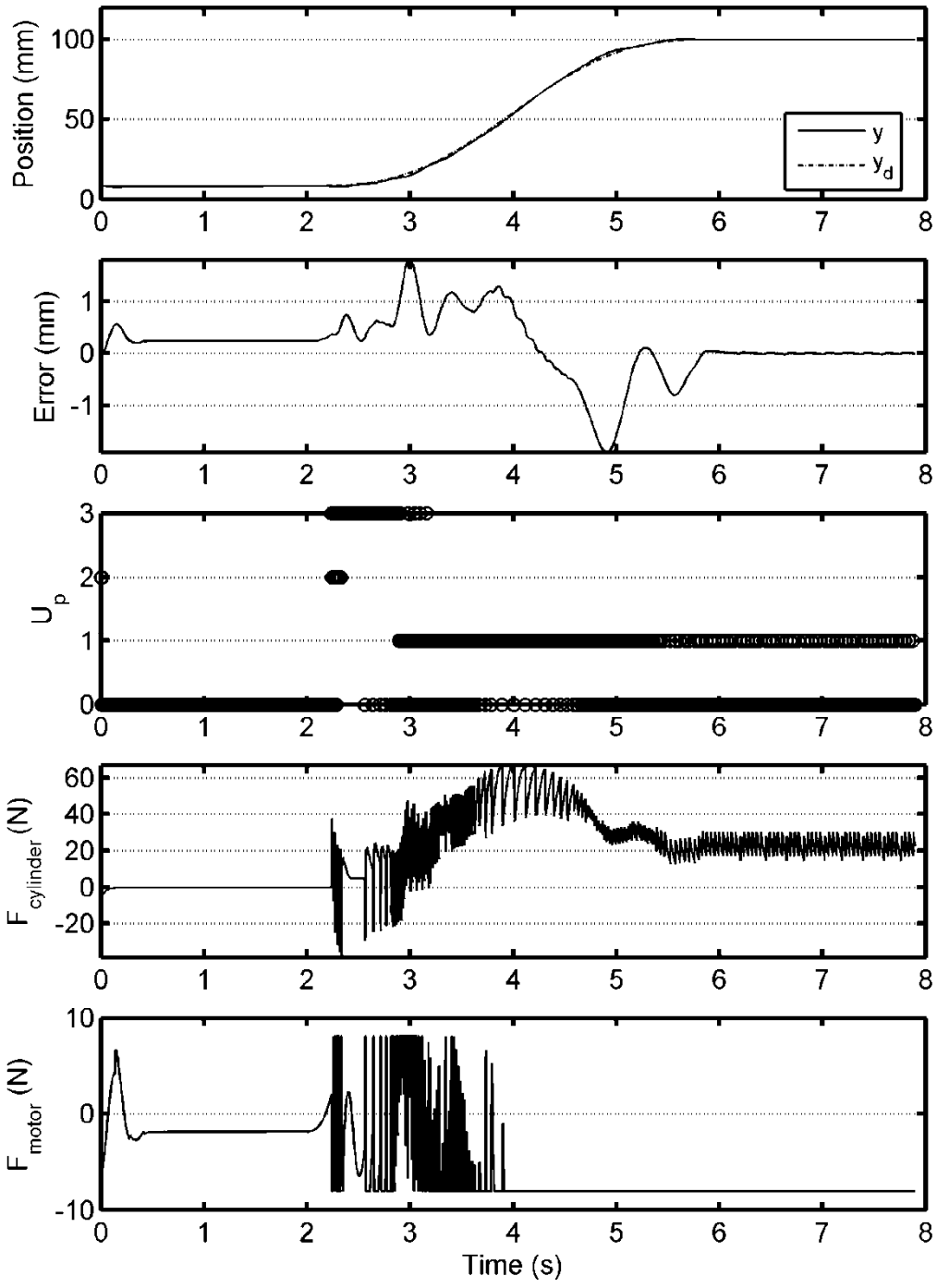

Figure 6-12 Vertical cycloidal trajectory simulation with the hybrid actuator, DMPC+I cylinder controller and ID motor controller, and $m_{payload}$ = 0.46 kg.

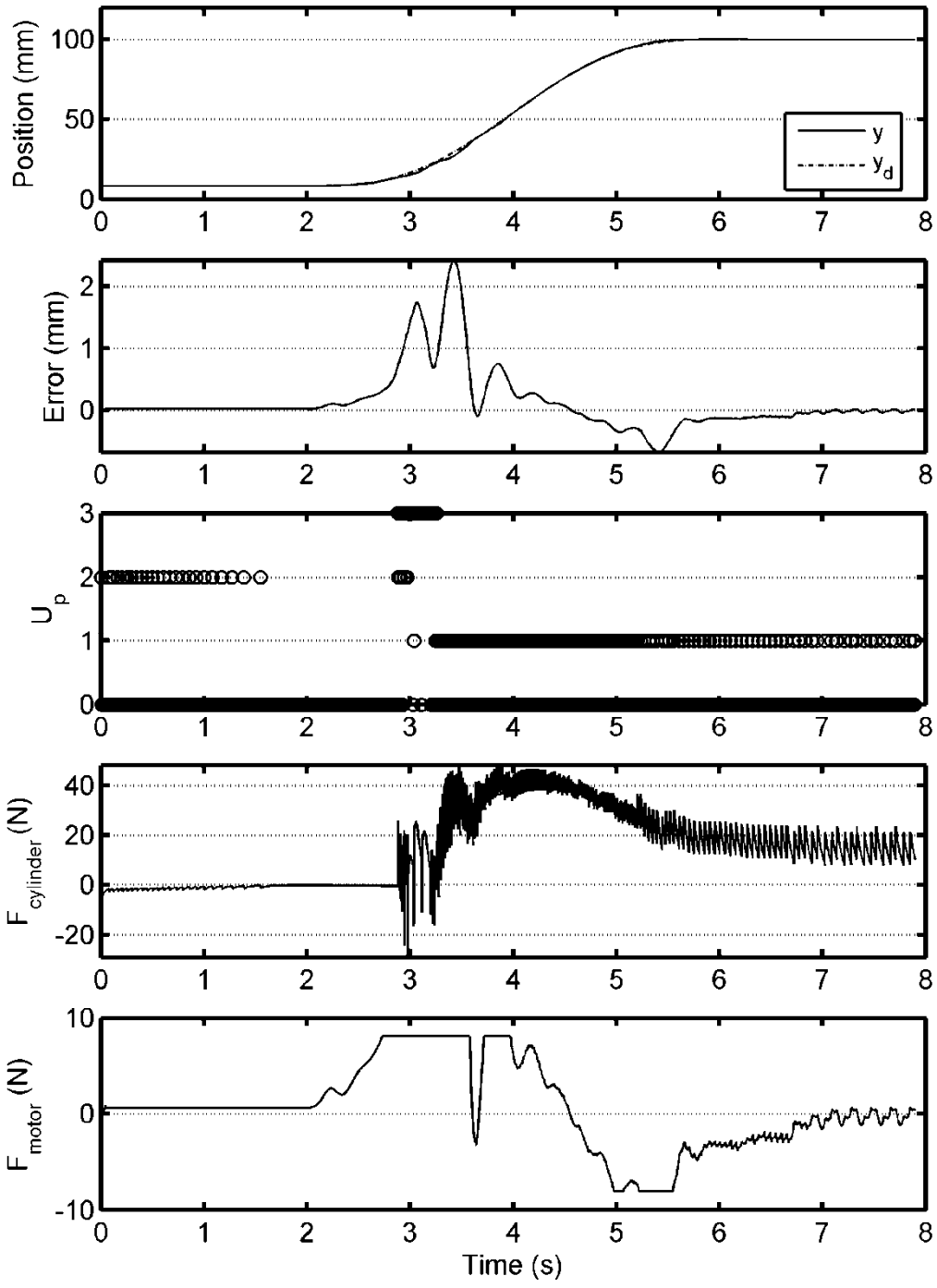

Figure 6-13 Vertical cycloidal trajectory simulation with the hybrid actuator, DMPC+I cylinder controller and PD motor controller, and $m_{payload}$ = 0.46 kg.

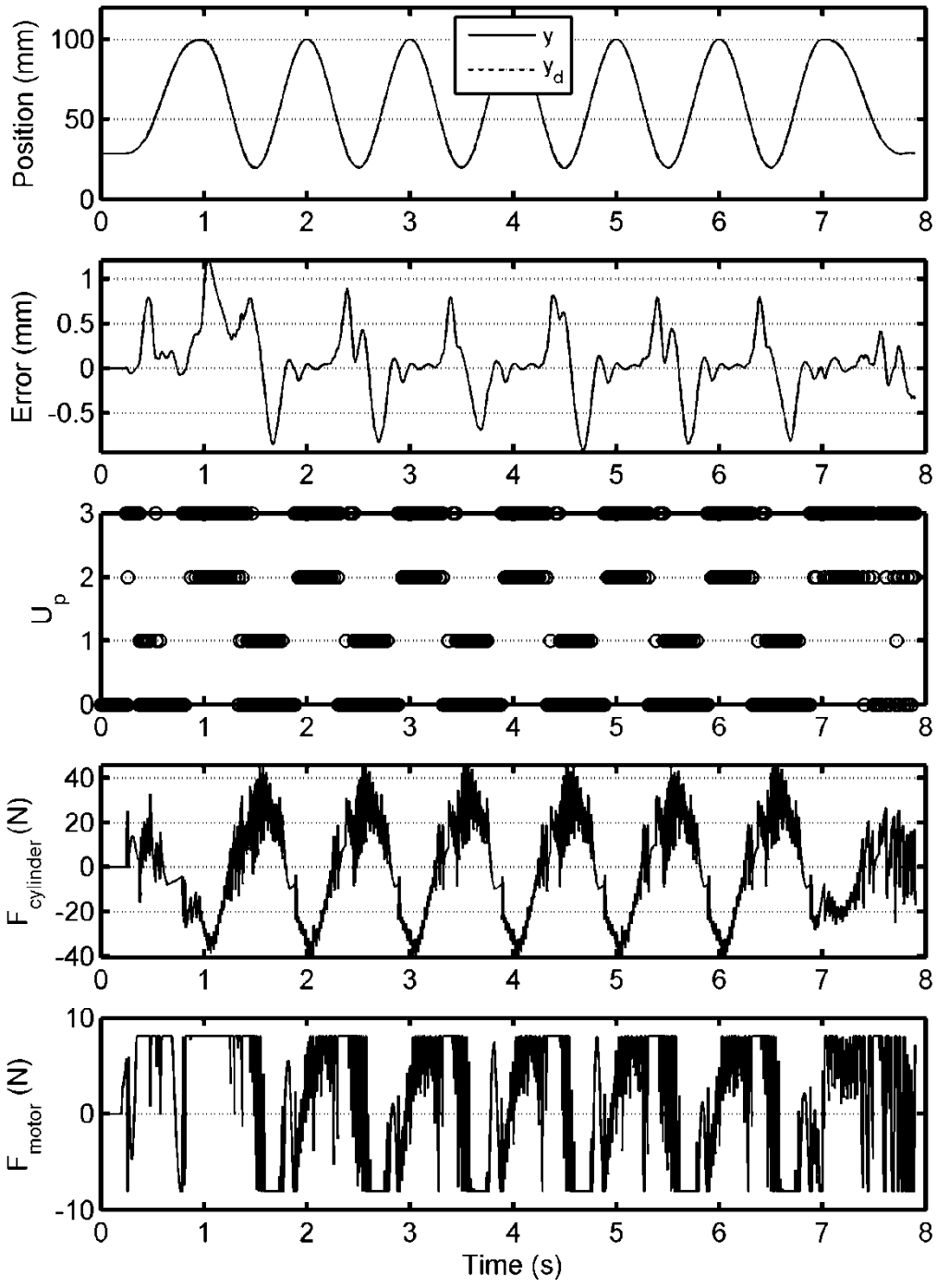

Figure 6-14 Vertical sine wave trajectory simulation with the hybrid actuator, DMPC+I cylinder controller and ID motor controller, and $m_{payload}$ = 0 kg.

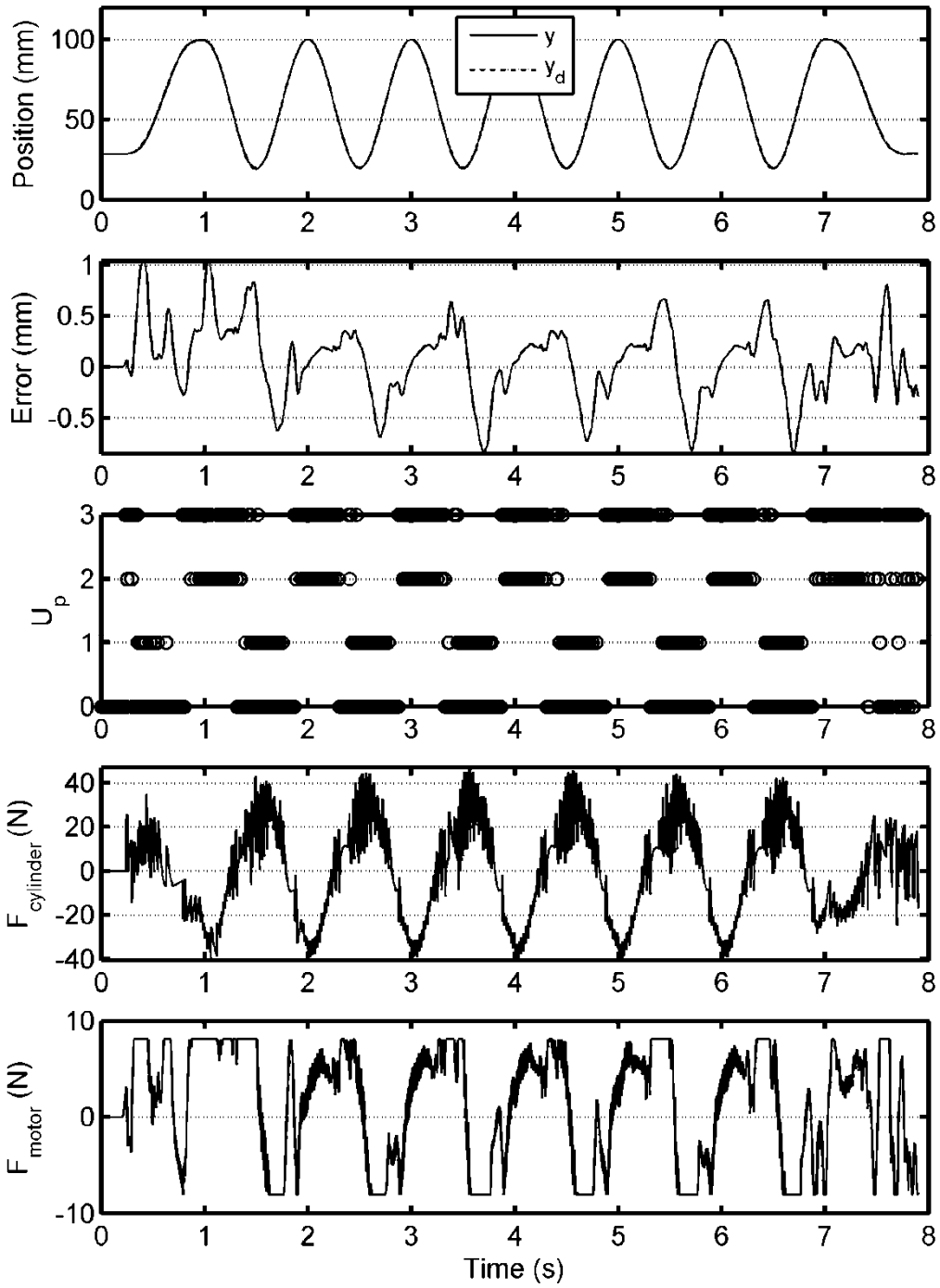

Figure 6-15 Vertical sine wave trajectory simulation with the hybrid actuator, DMPC+I cylinder controller and PD motor controller, and $m_{payload}$ = 0 kg.

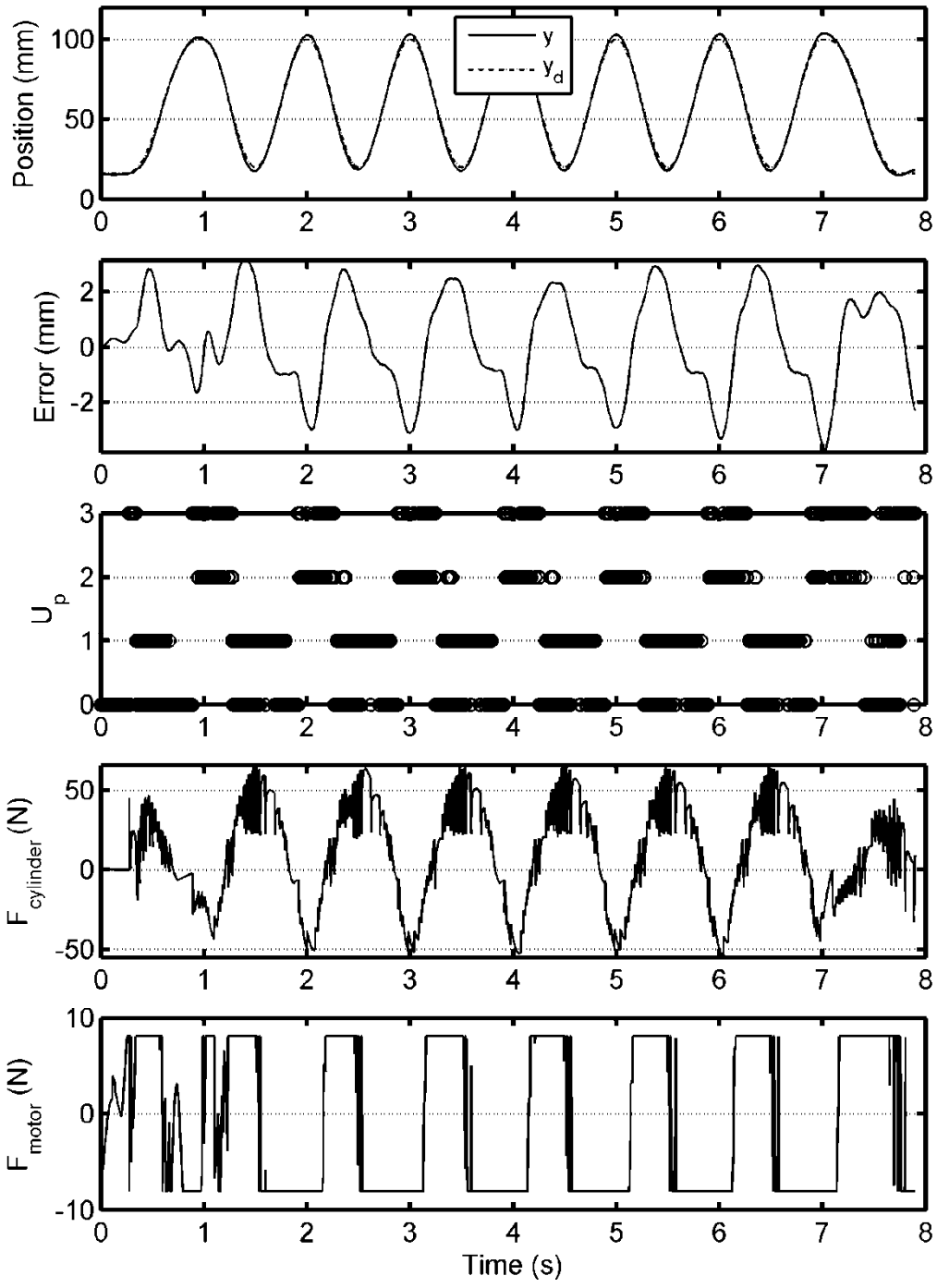

Figure 6-16 Vertical sine wave trajectory simulation with the hybrid actuator, DMPC+I cylinder controller and ID motor controller, and $m_{payload}$ = 0.15 kg.

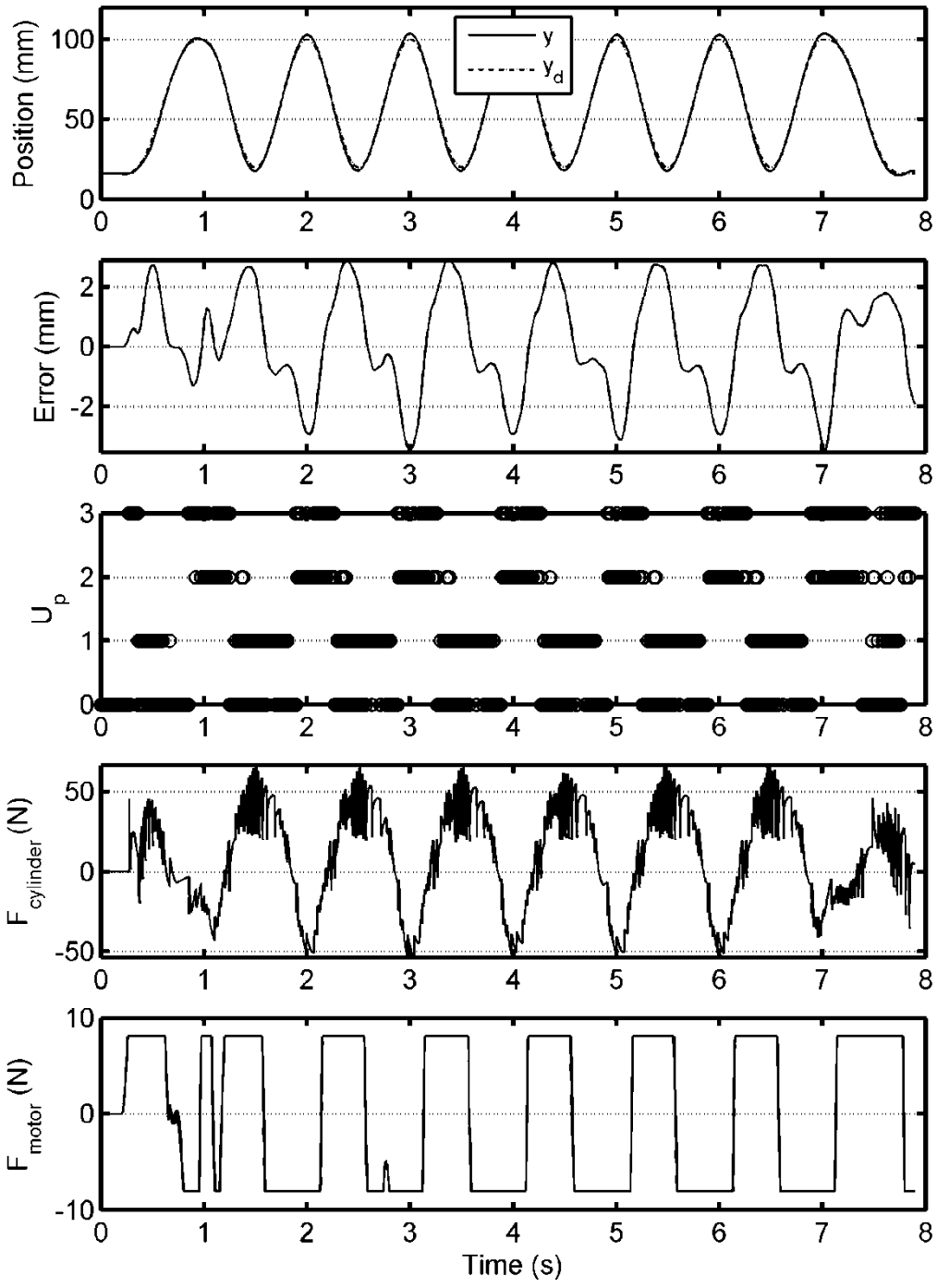

Figure 6-17 Vertical sine wave trajectory simulation with the hybrid actuator, DMPC+I cylinder controller and PD motor controller, and $m_{payload}$ = 0.15 kg.

Table 6-1 Simulation results for the vertical cycloidal trajectory.

Motor controller	$M_{payload}$ (kg)	RMSE (mm)	MAE (mm)	SSE (mm)	SSA (mm)
Inactive	0	0.68	2.22	0.03	2.85
ID	0	0.05	0.34	<0.01	<0.01
PD	0	0.15	0.61	0.13	<0.01
Inactive	0.15	0.45	2.46	<0.01	0.47
ID	0.15	0.21	0.60	<0.01	0.24
PD	0.15	0.27	1.52	<0.01	0.46
Inactive	0.46	0.86	3.71	0.03	0.06
ID	0.46	0.61	1.90	<0.01	0.03
PD	0.46	0.50	2.42	0.03	0.12

Table 6-2 Simulation results for vertical sine wave trajectory.

Motor controller	$M_{payload}$ (kg)	RMSE (mm)	MAE (mm)
Inactive	0	1.00	2.39
ID	0	0.37	1.21
PD	0	0.37	1.04
Inactive	0.15	2.52	4.82
ID	0.15	1.73	3.80
PD	0.15	1.68	3.52

6.6 Conclusions

This chapter presented simulation results for the following three systems with vertical motions and different payloads:

1. Pneumatic cylinder with DMPC+I controller.
2. Hybrid actuator with the pneumatic cylinder controlled by the DMPC+I controller and the DC Motor controlled by the ID controller.
3. Hybrid actuator with the pneumatic cylinder controlled by the DMPC+I controller and the DC Motor controlled by the PD controller.

Based on these results, the hybrid actuator produces a much better position control performance than the pneumatic cylinder acting alone. For the cycloidal trajectory, the average RMSE and MAE improved by 55% and 56%, respectively. For the sine wave trajectory, the average RMSE and MAE improved by 41% and 34%, respectively. The coarse quantization of u_p and the relatively slow speed of response of compressed air were the main causes of the lower performance of the cylinder plus DMPC+I controller. The improvement with the hybrid actuator was due to the DC motor adding a faster (or higher frequency) and finer quantized force to the force from the cylinder. This produced a combined force output that caused the actuator to track the desired position trajectory much more closely. It is also important to note that the steady state performance, in terms of SSE and SSA, did not improve significantly with the hybrid actuator, and was occasionally worse.

With the hybrid actuator, the ID motor controller worked better than the PD controller with the cycloidal trajectory, while the PD controller performed better than the ID controller with the sine wave trajectory. The ID controller is model-based and assumed the payload was zero (as did the DMPC-I controller). Of course this worked well when the actual payload was zero, but the performance worsened significantly as the payload was increased. The PD controller does not rely on a model. This of course made it more robust to payload changes. It also does not take the pneumatic force into account, so it tried to correct the error on its own and this tended to produce more aggressive control actions than the ID controller. This made the SSA larger with the PD controller and the cycloidal trajectory, but also helped it to outperform the ID when tracking the more dynamic sine wave trajectory. In these simulations the only source of uncertainty included was the mismatch between the assumed and actual payloads. With hardware experiments, additional uncertainties due to modeling error, and pressure sensor noise would further worsen the performance of the ID controller relative to the PD controller. For this reason, only the PD controller will be employed with the DC motor in the hardware experiments to be presented in the next chapter.

CHAPTER 7

EXPERIMENTS

7.1 Introduction

In this chapter, experiments will be performed to test the actual closed-loop performance of the hybrid actuator and the pneumatic cylinder acting alone. A proof-of-concept prototype was fabricated using the design presented in Chapter 3. With a real robot, the payload is not usually known in advance, or measured online. As in Chapter 6, to be conservative, a payload of zero is assumed by the controller in all of the experiments. The experiments with non-zero payloads will test the robustness of each controller. Experiment results will be presented and discussed for vertical cycloidal, vertical sine wave and horizontal sine wave trajectories. Note that most of the discussion presented in Chapter 6 also applies to the experiment results, and will not be repeated here for brevity.

7.2 Settings for the Experiments

As in Chapter 6, the pneumatic cylinder will be controlled using the DMPC+I algorithm. For the reasons presented in section 6.6, only the PD algorithm will be used to control the DC motor in this chapter. The manually tuned PD gain values were: K_{pe} = 23,000 N/m and K_{de} = 400 N/m/s. A payload of zero is assumed by the controller in all

of the experiments. Experiments with payloads of 0.15 kg and 0.46 kg are used to test the robustness of each controller. Recall that increasing $m_{payload}$ from 0 kg to 0.15 kg increases m_{eq} by 70% and $\max(|F_{gravity}|)$ by 150%. Increasing it from 0 kg to 0.46 kg increases m_{eq} by 230% and $\max(|F_{gravity}|)$ by 460%. The cycloidal and sine wave trajectories described in section 6.2 were employed as the desired trajectories to test the dynamic and steady-state performance. Each experiment was repeated five times. The majority of the experiments were performed with the arm moving upwards in the vertical plane since that form of movement requires the most actuator power. A few experiments were performed in the horizontal plane for the sine wave trajectory.

7.3 Experiment Results and Discussion

7.3.1 Pneumatic Cylinder Alone

7.3.1.1 Vertical Cycloidal trajectory

Figure 7-1 shows an experiment result with the DMPC+I controller and $m_{payload}$ = 0. As shown in Figure 6-1 shows, the transient part of the desired trajectory runs from t = 2 s to 6 s, and from t = 6 s to 8 s the trajectory is at steady state. Figure 6-1 also indicated that maximum acceleration requirements happen at t = 3 s and 5 s. At t = 4 s, the desired velocity reaches its maximum, and the desired acceleration changes sign. From the error plot in Figure 7-1, it can be observed that error shows some correspondence with these events. The error reached maximum positive values around t ≈ 3 s and 5 s and a maximum negative value around t ≈ 4 s. As the system reached steady state, the error

was larger than in the simulation (see Figure 6-3). At steady state, the position oscillated much less in the experiment. The limit cycle observed in the simulations did not occur. It may have been prevented by higher damping caused by increased friction when the experiments were performed compared to when the model was obtained.

7.3.1.2 Vertical sine wave trajectory

Figure 7-2 shows an experiment result for a vertical sine wave trajectory with the DMPC+I controller and zero payload. The corresponding simulation result was shown in Figure 6-6. The errors are larger than with the simulation, but otherwise follow a similar pattern. The maximum overshoots and undershoots occurred close to the times where the desired acceleration peaked (see Figure 6-2).

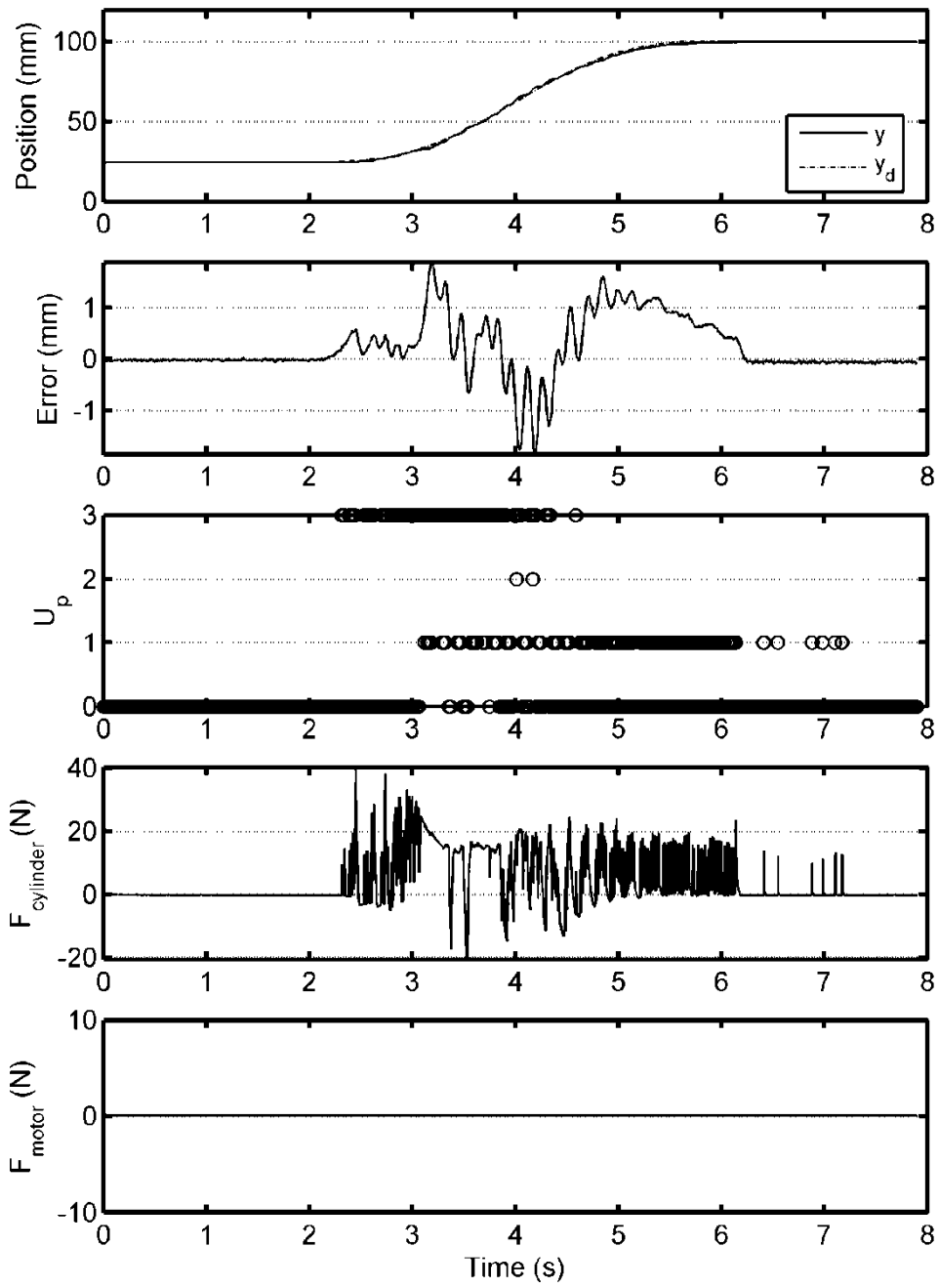

Figure 7-1 Vertical cycloidal trajectory experiment with the pneumatic cylinder, DMPC+I controller, and mpayload = 0 kg.

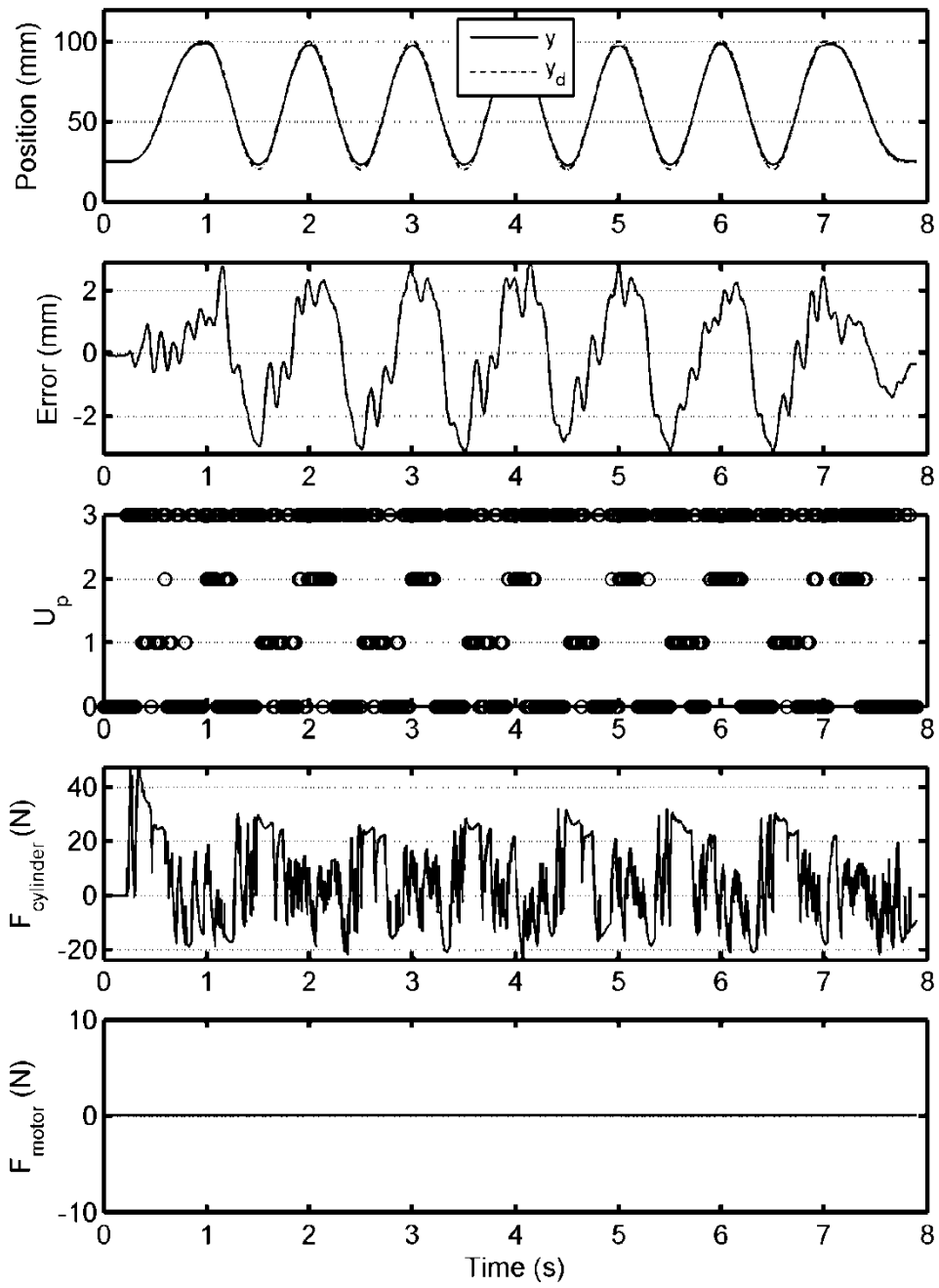

Figure 7-2 Vertical sine wave trajectory experiment with the pneumatic cylinder, DMPC+I controller, and $m_{payload}$ = 0 kg.

7.3.2 Hybrid Actuator

Figures 7-3 to 7-9 present example experiment results for the hybrid actuator. Results for repeated experiments are tabulated and discussed in section 7.3.3. The pneumatic cylinder is controlled by the DMPC+I algorithm and the DC motor is controlled by the PD algorithm. As in Chapter 6, the hybrid actuator clearly outperformed the pneumatic cylinder acting alone. The results will be discussed in further details below.

7.3.2.1 Vertical cycloidal trajectory

Figure 7-3 to 7-5 show results for the vertical cycloidal trajectory with payloads of 0, 15 kg and 0.46 kg, respectively. The transient performance degraded significantly as payload was increased. In particular, the MAE increased from 0.3 mm at $m_{payload}$ = 0 kg, to 1.6 mm at $m_{payload}$ = 0.15 kg, and to 3.3 mm at $m_{payload}$ = 0.46 kg. This was due in part to the mismatch between the assumed payload used by the DMPC+I algorithm and the actual payload that occurred when $m_{payload}$ = 0.15 kg and $m_{payload}$ = 0.46 kg. The assumed payload made the DMPC+I algorithm underpredict the required force, and then the DC motor tried to compensate for the insufficient pneumatic cylinder force. This added lag to the force response, and increased the duration of the motor force saturation periods, leading to worsened transient performance at those higher payloads. The same trends occurred with the simulation results (see Figure 6-9, 6-11 and 6-13). The steady state performance was relatively unaffected by the payload increase.

7.3.2.2 Vertical sine wave trajectory

Figures 7-6 and 7-7 show results for the vertical sine wave trajectory and payloads of 0 and 0.15 kg, respectively. Compared with the simulations (in Figures 6-15 and 6-17), the error patterns in these plots contain more random higher frequency oscillations. This is likely due to the effects of the position and pressure sensor noise. With a zero payload, the error magnitudes of the simulation and experiment are similar. Surprising, with the 0.15 kg payload the error magnitude with the experiment is roughly half the value found with the simulation. In the experiment, much less motor force saturation occurred (see the bottom plots in Figures 6-17 and 7-7), and this helped to keep the error relatively small.

7.3.2.3 Horizontal sine wave trajectory

Figures 7-8 and 7-9 show results for the horizontal sine wave trajectory and payloads of 0 and 0.46 kg, respectively. Note that the 0.46 kg payload was not used with the sine wave trajectory previously since the actuator cannot provide the force needed to follow this trajectory in the vertical plane. Even when gravity is removed, the large accelerations and large payload are difficult to handle, and the errors exceeded 5 mm as the plot in Figure 7-9 shows. With zero payload, the error magnitude is similar to the vertical case, and the maximum overshoots and undershoots once again tended to occur close to the times where the desired acceleration was maximum (see Figure 6-2).

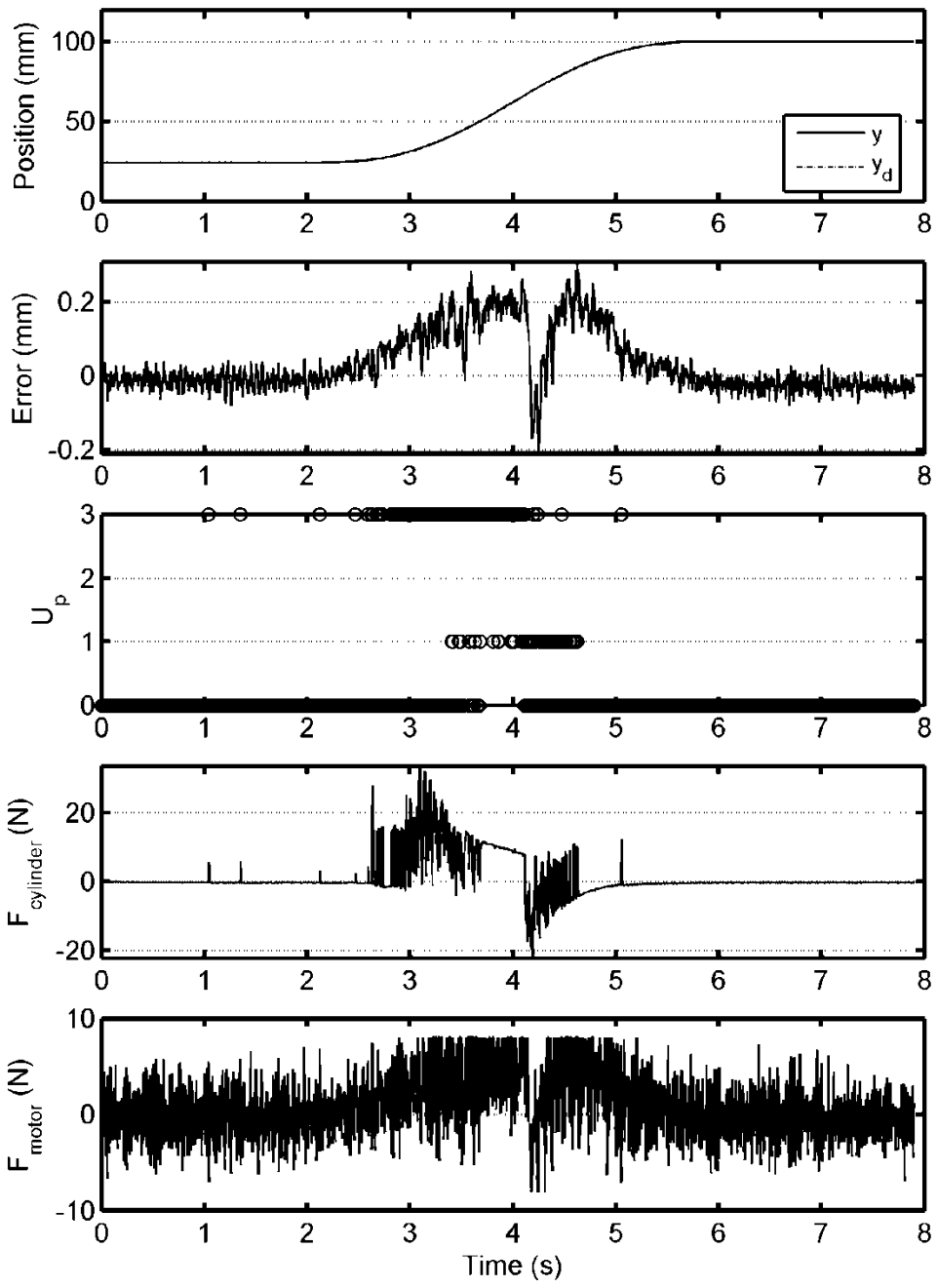

Figure 7-3 Vertical cycloidal trajectory experiment with the hybrid actuator, DMPC+I cylinder controller and PD motor controller, and mpayload = 0 kg

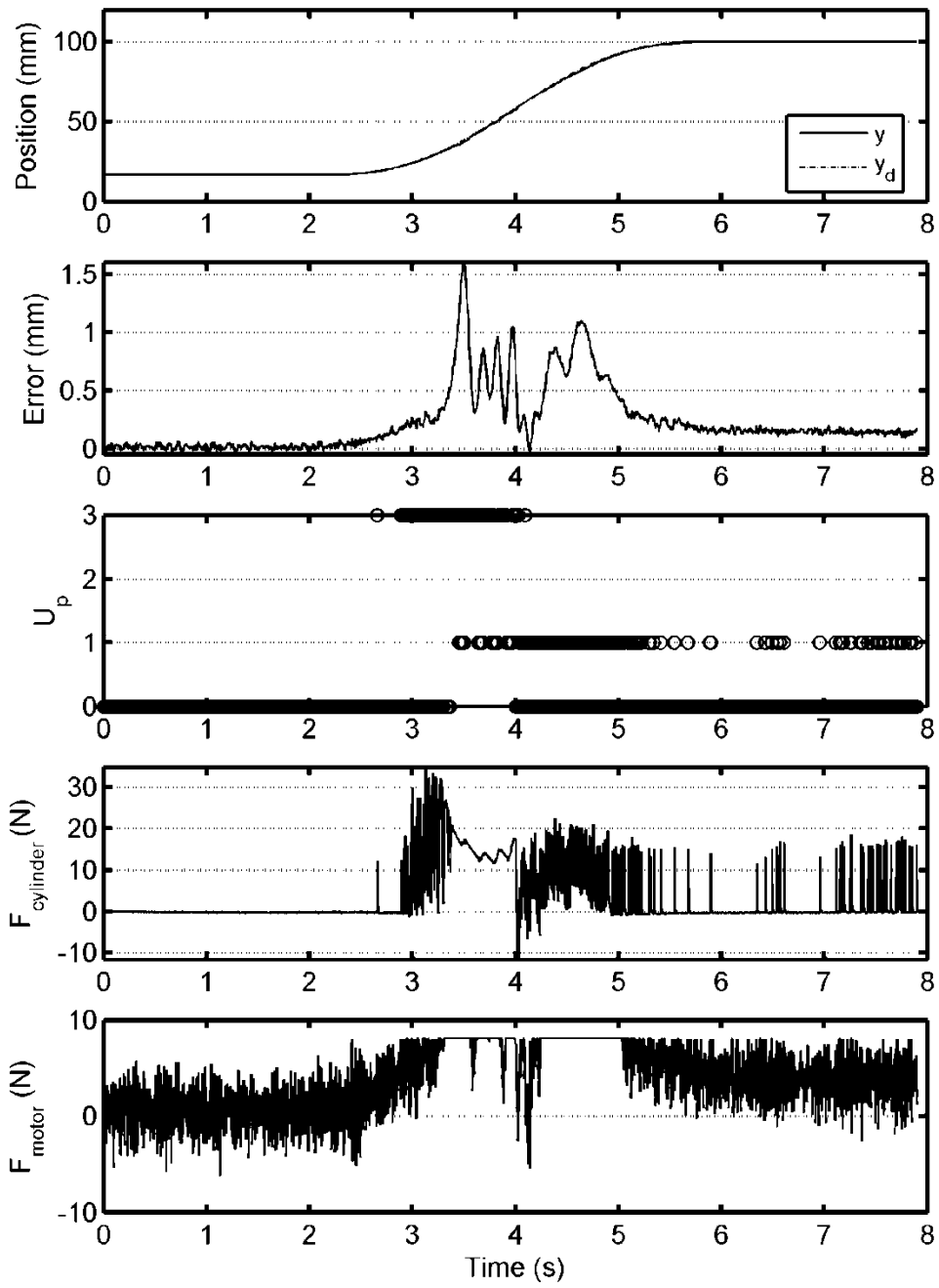

Figure 7-4 Vertical cycloidal trajectory experiment with the hybrid actuator, DMPC+I cylinder controller and PD motor controller, and $m_{payload}$ = 0.15 kg

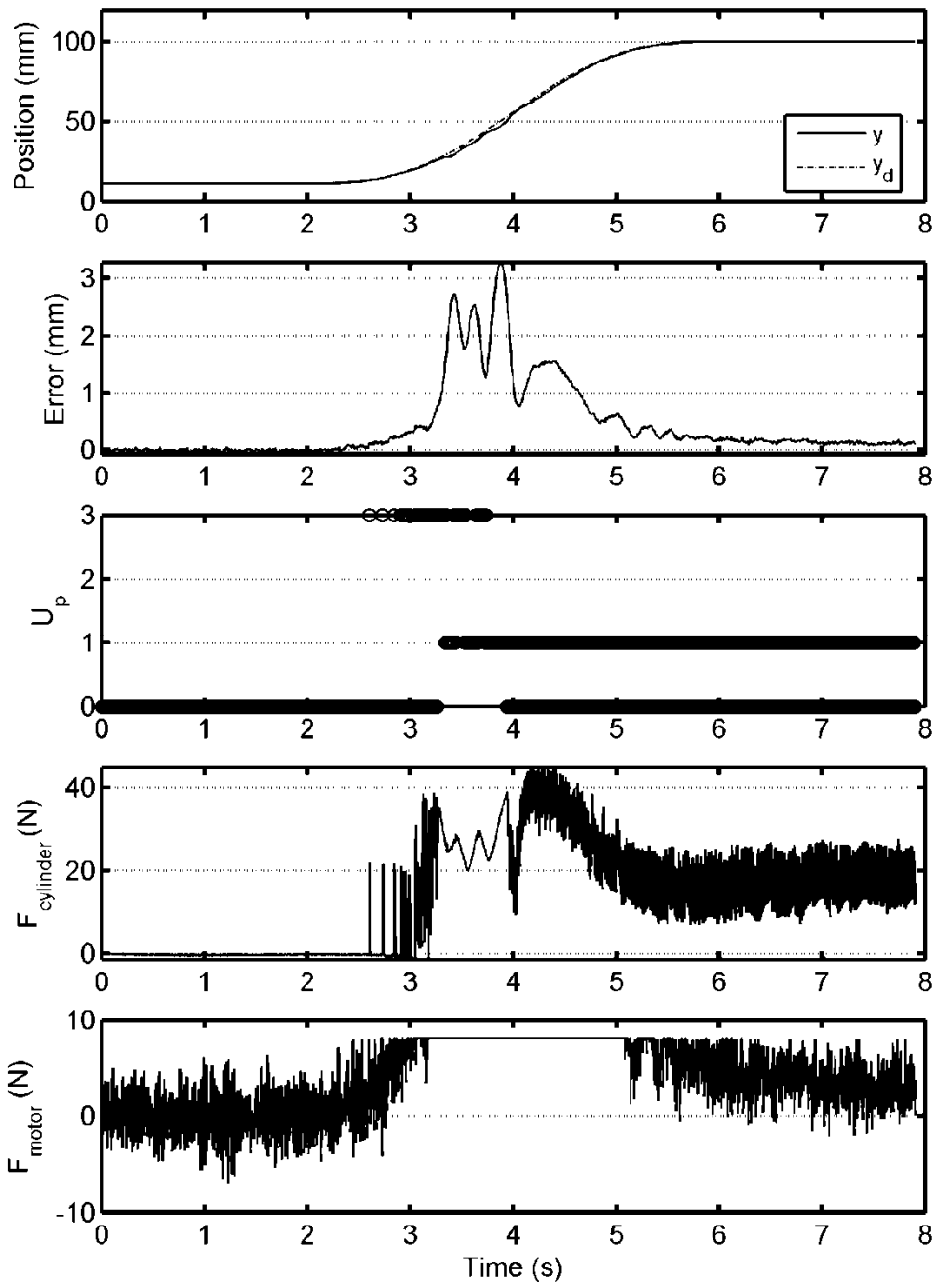

Figure 7-5 Vertical cycloidal trajectory experiment with the hybrid actuator, DMPC+I cylinder controller and PD motor controller, and $m_{payload}$ = 0.46 kg

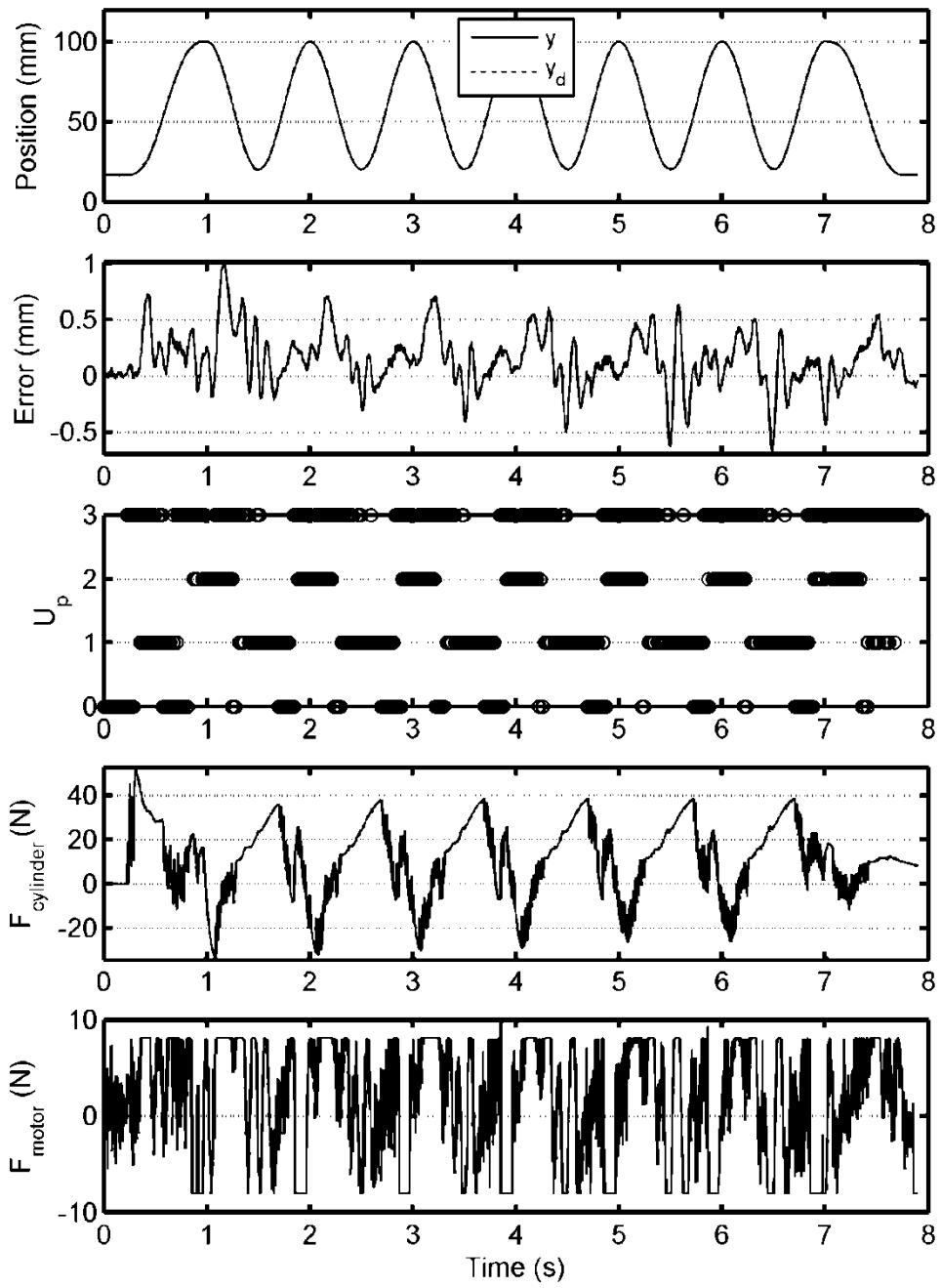

Figure 7-6 Vertical sine wave trajectory experiment with the hybrid actuator, DMPC+I cylinder controller and PD motor controller, and $m_{payload}$ = 0 kg

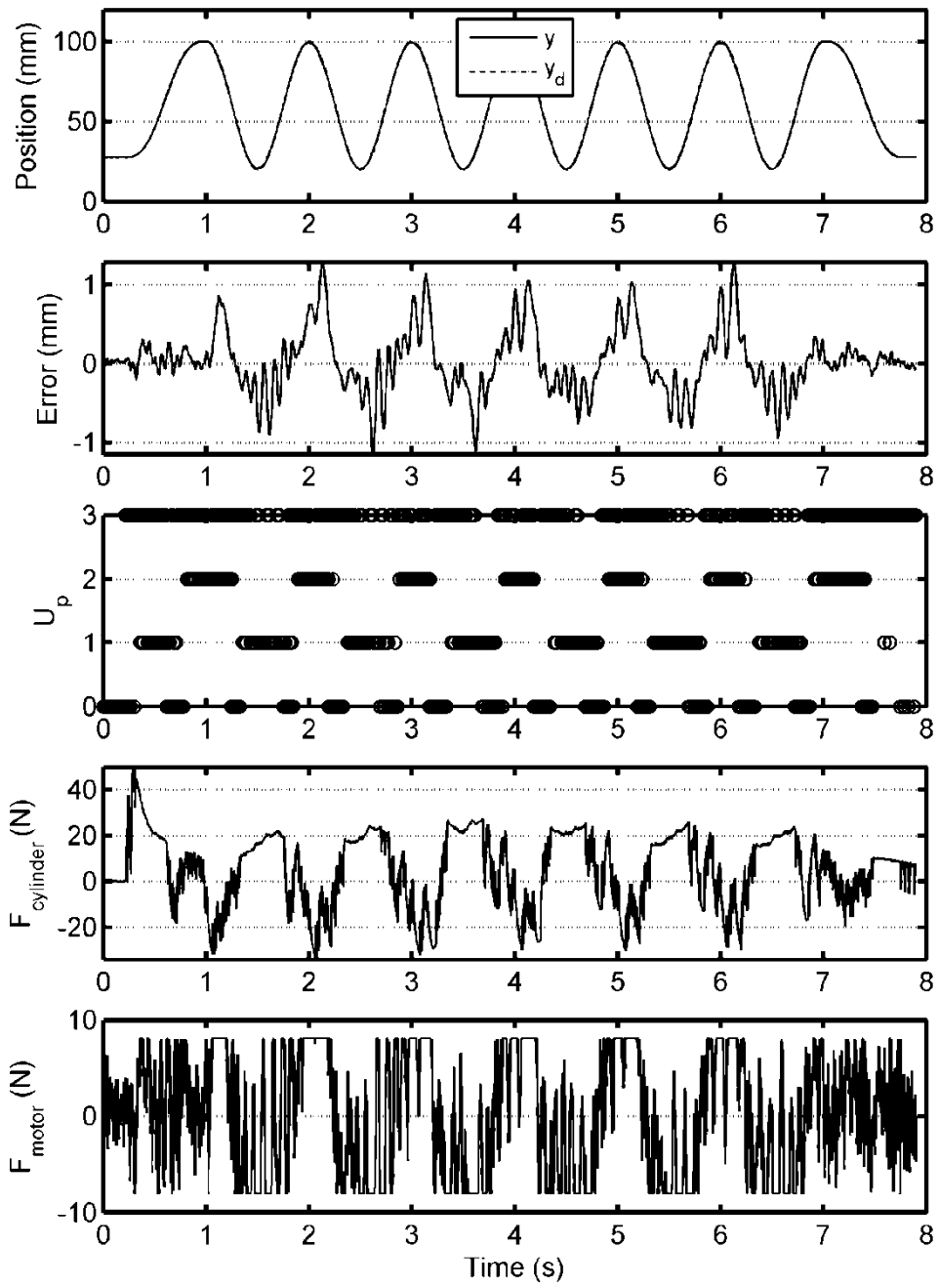

Figure 7-7 Vertical sine wave trajectory experiment with the hybrid actuator, DMPC+I cylinder controller and PD motor controller, and $m_{payload}$ = 0.15 kg

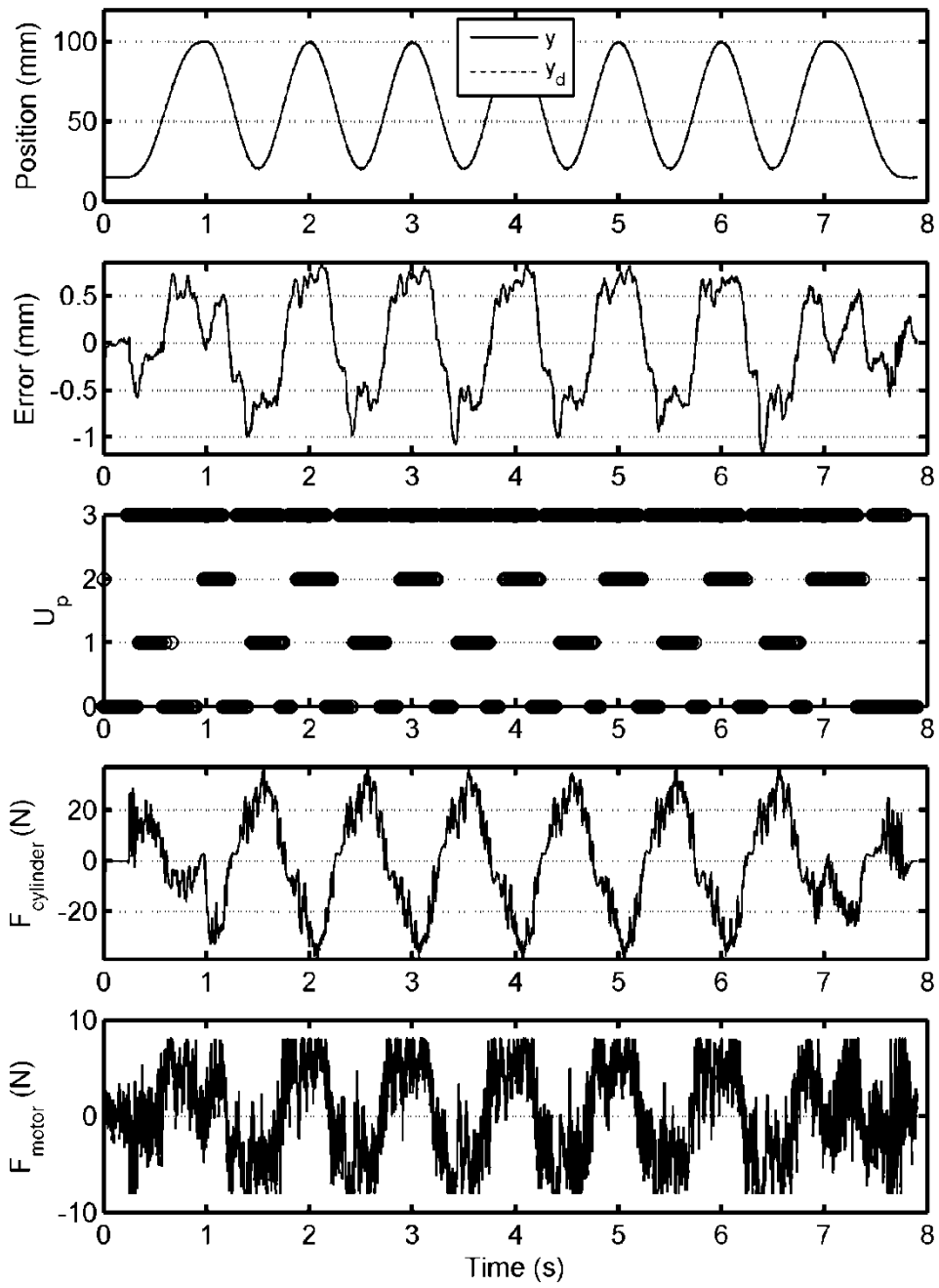

Figure 7-8 Horizontal sine wave trajectory experiment with the hybrid actuator, DMPC+I cylinder controller and PD motor controller, and $m_{payload}$ = 0.0 kg

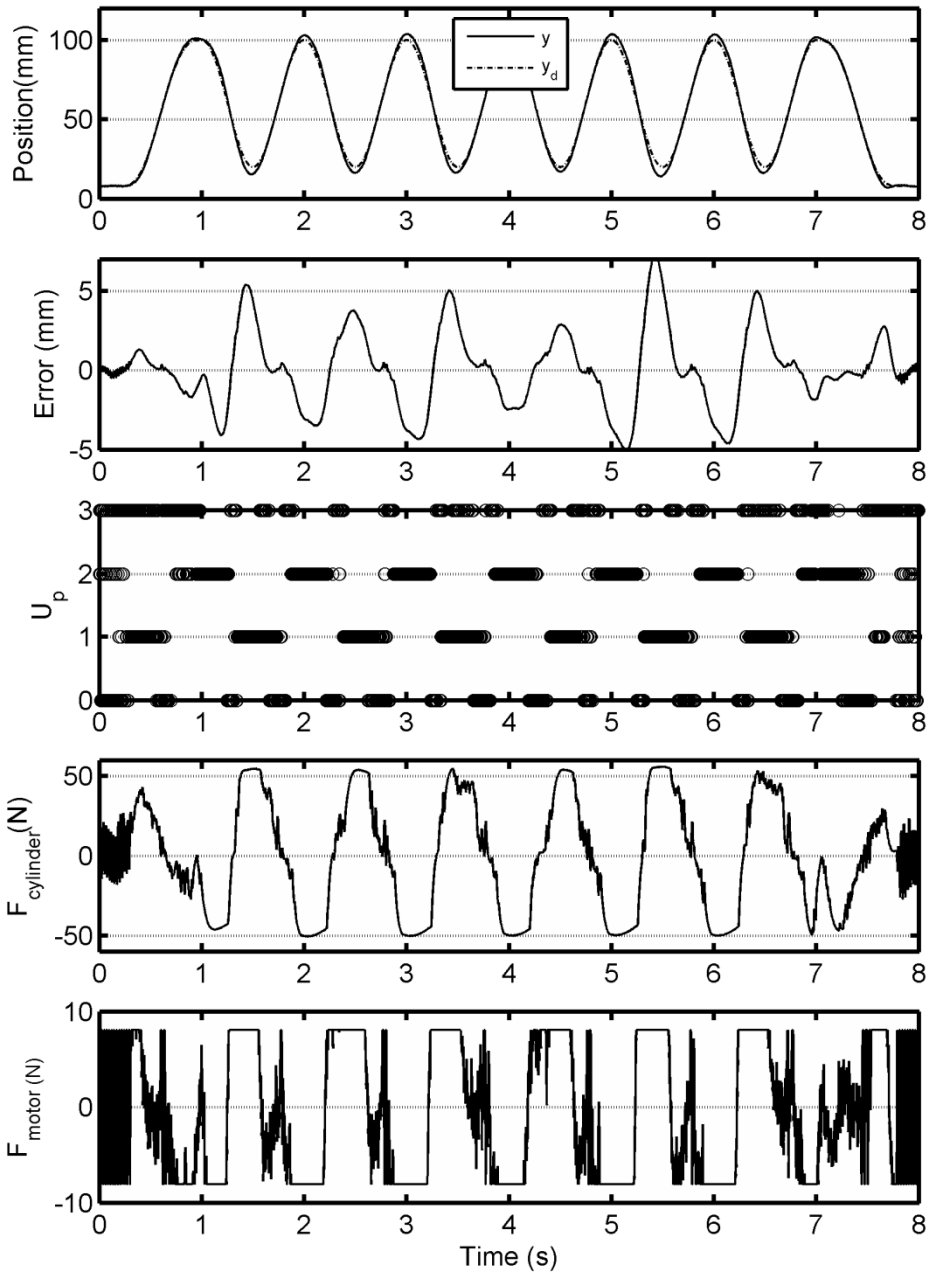

Figure 7-9 Horizontal sine wave trajectory experiment with the hybrid actuator, DMPC+I cylinder controller and PD motor controller, and $m_{payload}$ = 0.46 kg

7.3.3 Comparison based on the Performance Metrics

The performance metrics from the sets of five experiments are listed in Tables 7-1 to 7-9. This data shows that the deviations between the members of each set of experiments were small, so the performances of the pneumatic cylinder alone and the hybrid actuator were both quite repeatable. The mean values of these metrics are presented in Tables 7-10 to 7-12. As observed in Chapter 6, the transient performance of the hybrid actuator was clearly superior to the pneumatic cylinder alone. For the vertical cycloidal trajectory with zero payload, the mean RMSE and MAE improved by 86% and 85%, respectively. For the vertical sine wave trajectory with zero payload, the mean RMSE and MAE improved by 83% and 70%, respectively. The reasons for this performance improvement were previously discussed in section 6.6. As in the simulations, the mean SSE did not change significantly with the hybrid actuator.

For the hybrid actuator, for all three trajectories (*i.e.* vertical cycloidal, vertical sine wave, and horizontal sine wave), the experiment results followed the trend that as payload increased, the mean RMSE and mean MAE increased. This behavior was previously observed and discussed in sections 6.5.1.1, 6.5.1.2 and 7.3.2.1. Conversely, the steady state performance, as measured by the SSE and SSA metrics, did not change significantly when the payload was increased.

Table 7-1 Experiment results for vertical cycloidal trajectory with the pneumatic cylinder, DMPC+I controller, and mpayload = 0 kg

Performance Metric	Test 1	Test 2	Test 3	Test 4	Test 5	Mean
RMSE (mm)	0.52	0.61	0.58	0.61	0.58	0.58
MAE (mm)	1.92	2.03	1.88	2.03	1.93	1.96
SSE (mm)	0.05	0.06	0.06	0.04	0.02	0.04
SSA (mm)	0.18	0.15	0.08	0.31	0.37	0.22

Table 7-2 Experiment results for vertical cycloidal trajectory with the hybrid actuator, DMPC+I cylinder controller, PD motor controller, and mpayload = 0 kg.

Performance Metric	Test 1	Test 2	Test 3	Test 4	Test 5	Mean
RMSE (mm)	0.07	0.08	0.08	0.08	0.09	0.08
MAE (mm)	0.30	0.24	0.31	0.27	0.31	0.29
SSE (mm)	0.03	0.03	0.03	0.02	0.03	0.03
SSA (mm)	0.10	0.11	0.10	0.10	0.11	0.11

Table 7-3 Experiment results for vertical cycloidal trajectory with the hybrid actuator, DMPC+I cylinder controller, PD motor controller, and mpayload = 0.15 kg.

Performance Metric	Test 1	Test 2	Test 3	Test 4	Test 5	Mean
RMSE (mm)	0.35	0.34	0.33	0.36	0.36	0.35
MAE (mm)	1.78	1.59	1.50	1.57	1.60	1.61
SSE (mm)	0.15	0.15	0.15	0.15	0.15	0.15
SSA (mm)	0.10	0.09	0.09	0.10	0.11	0.10

Table 7-4 Experiment results for vertical cycloidal trajectory with the hybrid actuator, DMPC+I cylinder controller, PD motor controller,and mpayload = 0.46 kg.

Performance Metric	Test 1	Test 2	Test 3	Test 4	Test 5	Mean
RMSE (mm)	0.80	0.75	0.75	0.78	0.75	0.76
MAE (mm)	3.28	2.90	2.78	2.94	3.09	3.00
SSE (mm)	0.13	0.14	0.15	0.13	0.14	0.14
SSA (mm)	0.13	0.15	0.15	0.12	0.17	0.14

Table 7-5 Experiment results for vertical sine wave trajectory with the pneumatic cylinder, DMPC+I controller, and mpayload = 0 kg.

Performance Metric	Test 1	Test 2	Test 3	Test 4	Test 5	Mean
RMSE (mm)	1.59	1.61	1.62	1.62	1.67	1.62
MAE (mm)	3.22	3.40	3.24	3.24	3.19	3.26

Table 7-6 Experiment results for vertical sine wave trajectory with the hybrid actuator, DMPC+I cylinder controller, PD motor controller, and mpayload = 0 kg.

Performance Metric	Test 1	Test 2	Test 3	Test 4	Test 5	Mean
RMSE (mm)	0.28	0.28	0.25	0.30	0.26	0.28
MAE (mm)	0.88	1.01	0.96	1.01	1.01	0.97

Table 7-7 Experiment results for vertical sine wave trajectory with the hybrid actuator, DMPC+I cylinder controller, PD motor controller,and mpayload = 0.15 kg.

Performance Metric	Test 1	Test 2	Test 3	Test 4	Test 5	Mean
RMSE (mm)	0.39	0.42	0.41	0.41	0.42	0.41
MAE (mm)	1.14	1.43	1.28	1.22	1.31	1.28

Table 7-8 Experiment results for horizontal sine wave trajectory with the hybrid actuator, DMPC+I cylinder controller, PD motor controller, and mpayload = 0.0 kg.

Performance Metric	Test 1	Test 2	Test 3	Test 4	Test 5	Mean
RMSE (mm)	0.52	0.52	0.52	0.52	0.52	0.52
MAE (mm)	1.00	1.14	1.10	1.18	1.19	1.12

Table 7-9 Experiment results for horizontal sine wave trajectory with the hybrid actuator, DMPC+I cylinder controller, PD motor controller,and mpayload = 0.46 kg.

Performance Metric	Test 1	Test 2	Test 3	Test 4	Test 5	Mean
RMSE (mm)	2.30	2.60	2.46	2.12	1.92	2.28
MAE (mm)	5.25	8.29	7.34	5.65	4.73	6.25

Table 7-10 Mean values of experiment results for vertical cycloidal trajectory.

Motor controller	$m_{payload}$ (kg)	Mean RMSE (mm)	Mean MAE (mm)	Mean SSE (mm)	Mean SSA (mm)
Inactive	0	0.58	1.96	0.04	0.22
PD	0	0.08	0.29	0.03	0.11
PD	0.15	0.35	1.61	0.15	0.10
PD	0.46	0.76	3.00	0.14	0.14

Table 7-11 Mean values of experiment results for vertical sine wave trajectory.

Motor controller	$m_{payload}$ (kg)	Mean RMSE (mm)	Mean MAE (mm)
Inactive	0	1.62	3.26
PD	0	0.28	0.97
PD	0.15	0.41	1.28

Table 7-12 Mean values of experiment results for horizontal sine wave trajectory.

Motor controller	$m_{payload}$ (kg)	Mean RMSE (mm)	Mean MAE (mm)
PD	0	0.52	1.12
PD	0.46	2.28	6.25

7.4 Conclusions

In this chapter, experiments were performed with the hybrid actuator and with the pneumatic cylinder acting alone. Tests were done for vertical cycloidal, vertical sine wave and horizontal sine wave trajectories and different payloads. It was found that the pneumatic cylinder and hybrid actuator produce similar steady state performances. However, the transient (or dynamic) performance of the hybrid actuator was clearly superior. Based on the tests performed with zero payload, the mean RMSE and MAE improved by 84% and 77%, respectively. Regarding robustness, the steady state performance of the hybrid actuator was insensitive to changing the payload from zero to 0.46 kg. Recall that this payload change increases m_{eq} by 230% and $\max(|F_{gravity}|)$ by 460%. This increase did significantly enlarge the errors observed during the transient portions of the trajectories, but the stability of the responses was not obviously affected (*i.e.* the amplitudes of the oscillations decayed quickly to reach steady state).

Unfortunately, the proof-of-concept prototype has since suffered mechanical and electrical failures. As a result, further experiments cannot be performed with it. The design and construction of a more reliable prototype should be the subject of future work.

CHAPTER 8

CONCLUSIONS

8.1 Summary

In this thesis, a novel hybrid pneumatic-electric actuator was developed. A proof-of-concept prototype was designed and built. A mathematical model of the actuator dynamics was derived using a combination of physical laws and empirical curve fitting. A novel model-based position control algorithm was created for the pneumatic actuator. A conventional PD controller was used with the electric motor. The performance was investigated using computer simulations and hardware experiments. The position control precision of the hybrid actuator was far superior to the performance of the pneumatic actuator working alone.

8.2 Achievements

The main achievements of this thesis are as follows:

1. A proof-of-concept hybrid actuator prototype was designed and built. This prototype consisted of a pneumatic cylinder and a DC motor connected in parallel using gears; and was used to drive a single-link robot arm. Compared to the design of Takemura et al. (2000), the proposed design uses a low friction cylinder rather than a high friction air motor, and uses solenoid valves rather expensive servo valves.

2. A detailed nonlinear model of the actuator dynamics was developed. The dynamics of the mechanical, electrical and pneumatic elements were included.
3. Based on the system model, a novel discrete-valued model-predictive control plus integral compensator algorithm was created for controlling the position of a pneumatic actuator using on/off valves.
4. The control algorithm for the hybrid actuator was completed by using a conventional PD algorithm to control the electric motor. This combination performed well under both dynamic and steady state conditions, and was fairly robust to changes in the payload mass.
5. Experiments were performed with the hybrid actuator and with the pneumatic cylinder acting alone. Multiple tests were done for vertical cycloidal, vertical sine wave and horizontal sine wave trajectories, and different payloads.
6. It was found that the pneumatic cylinder and hybrid actuator produce similar steady state performances. However, the transient (or dynamic) performance of the hybrid actuator was clearly superior. The details were presented in Chapter 7.

8.3 Recommendations for Future Work

1. The major limiter of the pneumatic system performance is the coarse quantization of its valves. The system used a 3-way valve to control the charging and discharging of each chamber. Each valve can be either open to the atmosphere or open to the air supply. This gives the control signal a total

of four states as listed in Table 5-1. The DMPC+I algorithm should chose the best valve state for the system, but this valve state may still cause a large error. Also, when the arm is moving in the vertical plane, there is no valve state that can maintain an equilibrium state between pneumatic force and gravity force. The possible solutions include using several more valves with pulse-code modulation, or using servo valves would add significantly to the hardware cost. For future research work, it is recommended that four 2-way valves are used to replace the two existing 3-way valves. With two 2-way valves per chamber, each chamber can have three states: charging, discharging, and blocked (i.e. when both valves are off). This will increase the number of the control signal states from four to nine. In particular it would be possible to trap the air inside the chambers so the system could maintain an equilibrium position against gravity without consuming energy. Since 2-way solenoid valves are inexpensive the additional hardware cost would be low.

2. The DMPC+I control algorithm incorporated an integral component to compensate for the SSE caused by system uncertainties. This integral component operated over the full duration of each experiment. It effectively reduced the SSE, but also caused the oscillation in the position response. It may not be necessary to incorporate the errors from the full duration. A forgetting factor can be introduced into this compensator so that it only integrates the recent errors. Also, the integral gain was

manually tuned in this thesis. A more sophisticated tuning method should be developed.

3. The hybrid actuator developed in this thesis combines pneumatic and electric power. The ratio between maximum pneumatic cylinder force and maximum electric motor force is about 10:1. This ratio may not be the best choice, and it is not obvious how a better ratio should be determined. From this thesis research, it can be seen that a larger electric force would benefit the position control performance, but it would also significantly increase the system cost and system weight. A method for more optimally choosing the force ratio should be investigated.
4. A more mechanically robust prototype should be built for future work.

References

Airpot Corporation (2009), "Airpel performance specifications", April 2009, http://airpot.com/html/airpels.html.

Barth, E.., Zhang, J., and Goldfarb, M. (2003), "Control design for relative stability in a PWM-controlled pneumatic system", *Journal of Dynamic Systems, Measurement, and Control*, vol. 125, p. 504, 2003.

Chiang, M., Chen, C., and Tsou, T. (2005), "Large stroke and high precision pneumatic -piezoelectric hybrid positioning control using adaptive discrete variable structure control", *Mechatronics*, vol. 15, pp. 523-545, 2005.

Clarke, D. (1988), "Application of generalized predictive control to industrial processes", *IEEE Control Systems Magazine*, vol. 8, pp. 49-55, 1988.

Corteville, B., Van Brussel, H., Al-Bender, F., and Nuttin, M. (2005), "The development of a frictionless pneumatic actuator: A mechatronic step towards safe human robot interaction", in *2005 IEEE International Conference on Mechatronics*, Taipei, Taiwan, pp. 179-184, 2005.

Jones, J., and Hawkins, G. (1986), *Engineering Thermodynamics: an Introductory Textbook*, 2nd ed., John Wiley & Sons, New York, 1986.

Lai, J., Menq, C., and Singh, R. (1990), "Accurate position control of a pneumatic actuator", *ASME Journal of Dynamic Systems, Measurement, and Control*, vol. 112, pp. 734-739, 1990.

Liberzon, D. (2003), *Switching in systems and control*, Birkhauser, Boston, 2003.

Liu, S., and Bobrow, J. E. (1988), "An analysis of a pneumatic servo system and its application to a computer-controlled robot", *ASME Journal of Dynamic Systems, Measurement, and Control*, vol. 110, p. 228, 1988.

MAC (2009), "Direct solenoid and solenoid pilot operated valves", April 2009, http://www.macvalves.com/products/Three_Way/Small/34/34.pdf.

Maxon Motor (2009), "Maxon RE40 148877 specification", April 2009, http://shop.maxonmotor.com/ishop/article/article/148877.xml.

McDonell, B. W., and Bobrow, J. E. (1993), "Adaptive tracking control of an air powered robot actuator", *Journal of Dynamic Systems, Measurement, and Control*, vol. 115, p. 427, 1993.

Mills, J. K. (1990), "Hybrid actuator for robot manipulators: design, control and performance", in *Proceedings of the 1990 IEEE International Conference on Robotics and Automation*, pp. 1872 – 1878, 1990.

Moore, P., Weston, R., and Thatcher, T. (1985), "Compensation in pneumatically actuated servomechanisms", *Transactions of the Institute of Measurement and Control*, vol. 7, pp. 238-244, 1985.

Nguyen, T., Leavitt, J., Jabbari, F., and Bobrow, J. (2007), "Accurate sliding-mode control of pneumatic systems using low-cost solenoid valves", *IEEE/ASME Transactions on Mechatronics*, vol. 12, pp. 216-218, 2007.

Ning, S., and Bone, G. M. (2002), "High steady-state accuracy pneumatic servo positioning system with PVA/ PV control and friction compensation", in *Proceedings of the 2002 IEEE International Conference on Robotics and Automation*, Washington, DC, pp. 2824-2829, 2002.

Ning, S., and Bone, G. M. (2005), "Development of a nonlinear dynamic model for a servo pneumatic positioning system", in *Proceedings of the IEEE International Conference on Mechatronics and Automation (ICMA 2005),* Niagara Falls, Canada, pp.43-48, 2005.

Petrosky, L. J. (1987), "Hybrid electro-pneumatic robot joint actuator", U.S. Patent 478225828, October 1987.

Rao, Z., and Bone, G. M. (2008), "Nonlinear modeling and control of servo pneumatic actuators", *IEEE Transactions on Control Systems Technology*, vol. 16, pp. 562-569, 2008.

Rooks, B. (2006). "The harmonious robot", *Industrial Robot*, vol. 33, pp. 125-130, 2006.

Schindele, D., and Aschemann, H. (2008), "Nonlinear model predictive control of a high-speed linear axis driven by pneumatic muscles", *in 2008 American Control Conference (ACC '08)*, Seattle, WA, pp. 3017-3022, 2008.

Schindele, D., and Aschemann, H. (2009), "Adaptive friction compensation based on the LuGre model for a pneumatic rodless cylinder", in *Proceedings of 35th Annual Conference of IEEE Industrial Electronics*, pp. 1432 – 1437, 2009.

Shearer, J. (1956), "Study of pneumatic processes in the continuous control of motion with compressed air – I", *Transactions of the ASME*, vol. 78, pp. 233-242, 1956.

Shen, X., Zhang, J., Barth, E., and Goldfarb, M. (2006), "Nonlinear model-based control of pulse width modulated pneumatic servo systems", *ASME Journal of Dynamic Systems, Measurement, and Control*, vol. 128, p. 663, 2006.

Shigley, J. Mischke, C and Budynas, R. (2001), *Mechanical Engineering Design*, 6th ed. McGraw-Hill, New York, 2001.

Sindrey, R., and Bone, G. M. (2009), "Position tracking control of a miniature water hydraulic rotary actuator", *ASME Journal of Dynamic Systems, Measurement and Control*, Vol. 131, 2009.

Spong, M. W, and Vidyasagar, M. (1989), *Robot Dynamics and Control*, John Wiley & Sons, New York, 1989.

Stock Drive Products/Sterling Instrument (2009), "E Product Manager", April 2009, https://sdp-si.com/eStore/.

Takemura, F., Pandian, S., Nagase, Y., Mizutani, H., Hayakawa, Y., and Kawamura, S. (2000), "Control of a hybrid pneumatic/electric motor", in *Proceedings 2000 IEEE/RSJ International Conference on Intelligent Robots and Systems*, pp. 209-214, 2000.

Tsang, T., and Clarke, D.W. (1988), "Generalised predictive control with input constraints", *IEE Proceedings, Part D*, vol. 135, pp. 451-460, 1988.

Van Varseveld, R., and Bone, G. M. (1997), "Accurate position control of a pneumatic actuator using on/off solenoid valves", *IEEE/ASME Transactions on Mechatronics*, Vol.2, pp.195-204, 1997.

Wang, H. (1998), "On the estimation of on-off valve parameters for control of programmable pneumatic actuators", *Transactions of the Institute of Measurement and Control*, vol. 20, p. 211, 1998.

Wang, X., and Kim, C. (2000), "Self-tuning predictive control with forecasting factor for control of pneumatic lumber handling systems", *International journal of adaptive control and signal processing*, vol. 14, pp. 533-558, 2000.

Wang, X., Cheng, Y.-H. and Sun W. (2006), "Multi-step predictive control with TDBP method for pneumatic position servo system", *Transactions of the Institute of Measurement and Control*, vol. 28, pp. 53-68, Jan. 2006.

Ye, N., Scavarda, S., Betemps, M., and Jutard, A. (1992), "Models of a Pneumatic PWM Soleniod Valve for Engineering Applications", ASME Journal of Dynamic Systems, Measurement, and Control, vol. 114, pp. 680-688, 1992.

Appendix A GEAR SAFETY FACTOR CALCULATION

A.1 Introduction

Brass gear and rack are used in the experiment. To ensure the safety of experiment, gear strength needs to be calculated and safety factor must be determined before test can be processed.

A.2 System Parameters

Table A-1 Gear and Arm Parameters

Number of teeth:	$N_g = 100$
Module:	$M = 0.75mm$
Pitch Diameter	$D_p = N_g M = 0.075m$
Gear Face Width:	$w_{face} = 3mm$
All rotating part mass	$m_{arm} = 1.27kg$
Distance from COG to rotation center	$d_{arm} = 0.26m$

A.3 Motion Trajectory

By using Cycloidal trajectory, one cycle is from 0 to 180 degree then 180 to 0 degree

Total time to finish a cycle

$$T_{cycle} = 4s \quad \textbf{(A.1)}$$

Use Matlab code to find:

Max angular velocity

$$\omega_{\max} = 2.75 rad/s \quad \textbf{(A.2)}$$

Max linear velocity

$$v_{\max} = \omega_{\max} \times \frac{D_p}{2} = 0.103 m/s \quad \textbf{(A.3)}$$

Max angular acceleration

$$a_{\omega \max} = 1.23 rad/s^2 \quad \textbf{(A.4)}$$

A.4 Gear Teeth Stress Calculation

From equation (3.10), maximum Force required

$$F_{\max} = 72.80N \quad \textbf{(A.5)}$$

Gear Stress Calculation (Shigley et al., 2001)

Gear Load Factor:

$$K_v = \frac{6.1 + \frac{\omega_{\max}}{UnitOf(\omega_{\max})}}{6.1} = \frac{6.1 + 4.1430}{6.1} = 1.679 \quad \textbf{(A.6)}$$

Gear teeth stress:

$$\sigma = K_v \times \frac{F_{\max}}{w_{face} \times M \times 0.447} = 1.679 \times \frac{72.80}{3 \times 10^{-3} \times 0.75 \times 10^{-3} \times 0.447} = 121.53 MPa \quad \textbf{(A.7)}$$

Material Strength of Brass:

$$\sigma_{brass} = 239 MPa \quad \textbf{(A.8)}$$

Safety factor:

$$f = \frac{\sigma_{brass}}{\sigma} = \frac{239}{121.53} = 1.97 \quad \textbf{(A.9)}$$

A.5 Conclusion

Based on the safety factor calculated in equation (A.9), the gear strength meet the requirement of design specification.